

**Radiation Response and Optical Characterization of Carbon Based Thin-
films Prepared by Saddle Field Plasma Enhanced Chemical Vapor
Deposition**

by

Sameh Hegazy

A thesis submitted to the
School of Graduate and Postdoctoral Studies in partial
fulfillment of the requirements for the degree of

Master of Science in Material Science

Faculty of Science

University of Ontario Institute of Technology (Ontario Tech University)

Oshawa, Ontario, Canada

September 2020

© Sameh Hegazy, 2020

THESIS EXAMINATION INFORMATION

Submitted by: **Sameh Hegazy**

Master of Science in Material Science

Thesis title: Radiation Response and Optical Characterization of Carbon Based Thin-films Prepared by Saddle Field Plasma Enhanced Chemical Vapor Deposition
--

An oral defense of this thesis took place on August 27, 2020 in front of the following examining committee:

Examining Committee:

Chair of Examining Committee	Brad Easton
Research Supervisor	Franco Gaspari
Research Co-supervisor	Antony Waker
Examining Committee Member	Rayf Shiell
Thesis Examiner	Markus Piro

The above committee determined that the thesis is acceptable in form and content and that a satisfactory knowledge of the field covered by the thesis was demonstrated by the candidate during an oral examination. A signed copy of the Certificate of Approval is available from the School of Graduate and Postdoctoral Studies.

ABSTRACT

Carbon based thin-film materials have been attracting a lot of attention in many research fields due to their unique material properties. Detection of ionizing radiation is an important application that carbon and diamond based materials, which offer a promising detection material with low manufacturing cost and a variety of physical characteristics for different detection applications. In the current study, the direct current (DC) saddle field Plasma Enhanced Chemical Vapor Deposition (PECVD) method was used to prepare a set of nano-crystalline diamond samples. The relation between the deposition pressure, the gases mixing ratios and the resultant film characteristics were studied. The optical, microstructure and electronic properties of the prepared samples were studied using Raman spectroscopy, FTIR, UV-Visible spectroscopy and I–V characteristics methods. It was found that, an increase in the hydrogen content in the gas mixture leads to a decrease in the crystallinity of the resultant film. A set of samples were selected with different crystalline content and defect DOS to investigate the impact of these parameters on the material's radiation response. It was determined that, the sample with relatively high degree of crystallinity and with the presence of defects close to the valence show promising responses for radiation detection applications. We attributed this results to the fact that, transport is dominated by electrons and shallow defects near the conduction band act as electron traps. On the other hand, hole-traps near the valence band do not have the same impact on the overall transport properties

Keywords: PECVD Carbon Thin-film; Nan-Crystalline Diamond; Diamond Like Carbon; Radiation Detection.

AUTHOR'S DECLARATION

I hereby declare that this thesis consists of original work of which I have authored. This is a true copy of the thesis, including any required final revisions, as accepted by my examiners.

I authorize the University of Ontario Institute of Technology (Ontario Tech University) to lend this thesis to other institutions or individuals for the purpose of scholarly research. I further authorize University of Ontario Institute of Technology (Ontario Tech University) to reproduce this thesis by photocopying or by other means, in total or in part, at the request of other institutions or individuals for the purpose of scholarly research. I understand that my thesis will be made electronically available to the public.

Sameh Hegazy

STATEMENT OF CONTRIBUTIONS

I hereby certify that I am the sole author of this thesis and that no part of this thesis has been published or submitted for publication. I have used standard referencing practices to acknowledge ideas, research techniques, or other materials that belong to others. Furthermore, I hereby certify that I am the sole source of the creative works and/or inventive knowledge described in this thesis.

ACKNOWLEDGEMENTS

To my Supervisory Committee, Prof. Franco Gaspari ; I am really thankful for a lot of things most importantly the critical tricks in physics I used to catch in our conversations. Those tricks really enlightened my mind and helped me build an imagination or creating a picture of the material I am working on besides the great experimental tricks I have learned during working on the Vacuum system. Prof. Anotny Waker; I am really thankful for his continuous support and encouragement especially at the beginning steps of the project which essentially was initiated by a piece of advice from him and the last piece of measurement was also at his lab.

To my colleagues, I would like to thank all my colleagues who made the studying environment competitive and friendly in the same time. Especially I would like to mention Iraklii Ebralidze for his help with preparing the gold contacts, Holly Fruehwald for her help with the training on the Raman equipment, Ibrhim Giagouso for his help with holding the load lock gate (which is heavy by the way) until I finish hooking up the substrates to the substrate holder and finally my friend Tracy James Hokin who gave the vacuum system a funny name “medusa”.

To my Friend Ibrahim Hany who we started our first steps in the world of detection together and we used to have a strong debates around which is better for radiation detection, bulk materials or thin-film materials. And my friend Refaat Bekhiet who we started our first steps in the world of vacuum science together a long time ago and we still give counseling to each other.

Finally and most importantly, my Family. To my brother; Mohammed Hegazy who was usually there for me with counsel and support. I have no words that can express my gratitude for him but at least I wanted him to know, without him there was no way I can make it on my own.

Table of Contents

1. Introduction	1
2. The Family of Carbon Based Materials	3
2.1. Bonding Hybridization in Carbon Molecules	6
2.1.1. The carbon atom	6
2.1.2. SP hybridization.....	6
2.1.3. SP ² hybridization (Graphite)	7
2.1.3.1. Graphite crystal structure	9
2.1.4. SP ³ hybridization (Diamond).....	9
2.1.4.1. The Diamond material.....	10
2.2. The Ternary Diagram	12
2.3. Classification of Non-Crystalline Carbon Materials	13
2.4. Nano-Crystalline Diamond(NCD)	15
3. Solid State Radiation Detection	16
3.1. Interaction of Radiation with Matter	17
3.1.1. Interaction of electromagnetic radiation with matter	17
3.1.2. Interaction of heavy charged particles with matter	21
3.1.3. Interaction of neutral particles with matter (neutrons).....	22
3.2. Solid-State Detection Mechanism	22
3.3. Material Requirements for Solid-State Detection	24
3.4. Diamond Based Radiation Detectors	26
4. The Deposition Technique	29
4.1. Carbon Based Films PECVD Growth Mechanism	29
4.1.1. The role of atomic hydrogen.....	30
4.1.2. Film nucleation	32
4.2. The principle of DC Saddle field glow discharge	33
4.3. The experimental Set up	35
4.3.1. The vacuum system.....	35
4.3.2. The gases feeding system	39
4.3.3. The substrate holder	40
4.3.4. Power delivery system	41
5. Experimental Work	42
5.1. Samples Preparation	42

5.1.1.	Substrate selection.....	42
5.1.2.	Substrates cleaning procedures.....	43
5.1.3.	Vacuum system operational procedures.....	44
5.1.4.	Samples preparation conditions.....	45
5.2.	Samples Characterization.....	46
5.2.1.	Fourier transform infrared spectroscopy (FTIR).....	46
5.2.2.	Raman spectroscopy	47
5.2.2.1.	The generation of the Raman signal.....	47
5.2.2.2.	Raman spectrum of amorphous/diamond like carbon thin-films.....	48
5.2.2.3.	Raman spectrum of nano-diamond materials.....	50
5.2.3.	UV-Visible and measuring the band gap	50
5.2.4.	I-V characteristic and radiation measurement	51
6.	Results and Discussion	53
6.1.	FTIR Results.....	53
6.1.1.	S1 results and discussions	53
6.1.2.	S2 results and discussion.....	55
6.1.3.	S3 results and discussion.....	56
6.1.4.	S5 results and discussion.....	58
6.1.5.	S6 results and discussion.....	59
6.1.6.	S7 results and discussion.....	60
6.2.	Raman Spectroscopy Results	62
6.2.1.	S1 results and discussion.....	62
6.2.2.	S2 results and discussion.....	64
6.2.3.	S3 results and discussion.....	66
6.2.4.	S4 results and discussion.....	67
6.2.5.	S5 results and discussion.....	69
6.2.6.	S6 results and discussion.....	70
6.2.7.	S7 results and discussion.....	72
6.3.	UV-Visible and Band gap Measurements	73
6.3.1.	S5 Band gap measurement	73
6.3.2.	S6 Band gap measurement	74
6.3.3.	S7 Band gap measurement	74
6.4.	I-V Characteristics and Radiation Experiments	75

6.4.1.	S5 dark measurement	75
6.4.2.	S5 radiation measurement.....	78
6.4.3.	S6 radiation measurement.....	80
6.4.4.	S7 radiation measurement.....	81
7.	Conclusions and Recommendations for Future Work	83
7.1.	Conclusions.....	83
7.2.	Future Work.....	84
	References	85

LIST OF TABLES

CHAPTER 2

Table 2. 1 Intrinsic material properties of Diamond at room temperature	8
---	---

CHAPTER 3

Table 3. 1 comparison of some important material properties of diamond and silicon as one of the most popular material used in solid state detection industry.....	22
--	----

CHAPTER 5

Table 5. 1 samples preparation Conditions	40
---	----

CHAPTER 6

Table 6.1 S1 fitting results.....	45
-----------------------------------	----

Table 6.2 S2 fitting results.....	47
-----------------------------------	----

Table 6.3 S3 fitting results.....	48
-----------------------------------	----

Table 6.4 S5 fitting results.....	49
-----------------------------------	----

Table 6.5 S6 fitting results.....	50
-----------------------------------	----

Table 6.6 S7 fitting results.....	51
-----------------------------------	----

Table 6.7 S1 fitting results.....	52
-----------------------------------	----

Table 6.8 S2 fitting results.....	54
Table 6.9 S3 fitting results.....	55
Table 6.10 S4 fitting results.....	56
Table 6.11 S5 fitting results.....	57
Table 6.12 S6 fitting results.....	59
Table 6.13 S7 fitting results.....	60

LIST OF FIGURES

CHAPTER 2

Figure 2.1 Graphene and carbon nanotubes as (A) single wall carbon nanotube (SWCNT) and (B) multi-wall carbon nanotube (MWCNT) structures.....	4
Figure 2.2 representation of electronic configuration in carbon atom while in ground and excited state .	5
Figure 2.3 electronic configurations of SP^1 , SP^2 and SP^3 carbon hybridization	6
Figure 2.4 Formation of the SP hybrid orbital and SP sigma bond.....	7
Figure 2.5 (a) SP^2 hybridization orbitals, (b) in-plane σ bonds and out of plane π bonds	8
Figure 2.6 the single crystal SP^2 bonded structure (single crystal graphite).....	9
Figure 2.7 SP^3 hybridization and a cubic cell of diamond structure	10
Figure 2.8 ternary phase diagram of different carbon materials relating its SP^2 , SP^3 and H content.....	12
Figure 2.9 the three stage model that explains the amorphisation trajectory of carbon materials and its relation to the SP^2 and SP^3 content. Note that in stages 1–2 to a strong SP^2 cluster size (L_a) decrease corresponds a relatively small SP^3 increase, whilst the opposite is seen in stage 3.	13

CHAPTER 3

Figure 3. 1 Cross-sections of the three types of interaction mechanism of electromagnetic ionizing radiation as a function of photon energy for carbon.	15
--	----

Figure 3. 2 the dependence of the change of the incident photon wavelength on the scattering angle in Compton scattering interaction.....	17
Figure 3. 3 Bragg Curve describing the passage of heavy charged particle through matter.....	18
Figure 3. 4 electron-hole pair production mechanism and the effect of impurity levels in the band gap on the electron-hole pair production process	20
Figure 3. 5 typical design of simple diamond-based radiation detector	22
CHAPTER 4	
Figure 4. 1 schematic of the CVD growth mechanism of carbon thin-films	26
Figure 4. 2 Schematic of the reaction process occurring at the diamond surface leading to stepwise addition of CH ₃ species and diamond growth.	27
Figure 4. 3 DC saddle field configuration in its basic form	28
Figure 4. 4 a) saddle field triode configuration, b) saddle field shielded triode configuration	29
Figure 4. 5 schematic diagram of the experimental set up and its components	30
Figure 4. 6 two photos of the butterfly valve showing its totally closed position and totally opened position	31
Figure 4. 7 system baking out heaters	32
Figure 4. 8 the substrate holder showing the heater mount and clamps to fix the substrates	33
Figure 4. 9 substrate heater connection diagram.....	34

Figure 4. 10 Substrate heater electrical connection.....	34
--	----

CHAPTER 5

Figure 5. 1 samples preparation Conditions	39
--	----

Figure 5. 2 schematic diagram explaining the mechanism of Raman scattering, molecular vibrational transitions and the stokes/anti-stokes frequencies	40
--	----

Figure5. 3 Three-stage model of the variation of the Raman G position and the D-to-G intensity ratio, $I(D)/I(G)$, with increasing disorder . The dotted left-pointing arrows in (b) mark the non-uniqueness region in the ordering trajectory	41
---	----

Figure 5. 4 schematic diagram for I-V characteristic setup	43
--	----

CHAPTER 6

Figure 6. 1 S1 de-convoluted FTIR spectrum	45
--	----

Figure 6. 2 S2 de-convoluted FTIR spectrum	46
--	----

Figure 6.3 S3 de-convoluted FTIR spectrum	48
---	----

Figure 6. 4 S5 de-convoluted FTIR spectrum	49
--	----

Figure 6.5 S6 de-convoluted FTIR spectrum	50
---	----

Figure 6. 6 S7 de-convoluted FTIR spectrum	51
--	----

Figure 6. 7 S1 de-convoluted Raman spectrum in the range $1100-1700\text{cm}^{-1}$ excited by 532nm laser wavelength at 50% laser power and 10S exposure time	52
---	----

Figure 6. 8 S1 wide range raw data.....	53
Figure 6. 9 S2 de-convoluted Raman spectrum in the range 900-1900cm ⁻¹ excited by 532nm laser wavelength at 50% laser power and 10S exposure time	54
Figure 6. 10 S3 de-convoluted Raman spectrum in the range 1200-2200cm ⁻¹ excited by 532nm laser wavelength at 50% laser power and 10S exposure time	55
Figure 6. 11 S4 de-convoluted Raman spectrum in the range 900-1900cm ⁻¹ excited by 532nm laser wavelength at 50% laser power and 10S exposure time	56
Figure 6. 12 S5 de-convoluted Raman spectrum in the range 1000-1800cm ⁻¹ excited by 532nm laser wavelength at 50% laser power and 10S exposure time	57
Figure 6. 13 S6 de-convoluted Raman spectrum in the range 1000-1800cm ⁻¹ excited by 532nm laser wavelength at 50% laser power and 10S exposure time	58
Figure6. 14 S7 de-convoluted Raman spectrum in the range 900-1900cm ⁻¹ excited by 532nm laser wavelength at 50% laser power and 10S exposure time	59
Figure 6.1 5 S5 UV-Visible data fitted to Tauc equation a) for m value 0.5 representing direct allowed transition, b) for m value 1.5 representing direct forbidden transition	60
Figure 6. 16 S6 UV-Visible data fitted to Tauc equation a) for m value 0.5 representing direct allowed transition, b) for m value 1.5 representing direct forbidden transition	61
Figure 6. 17 S7 UV-Visible data fitted to Tauc equation a) for m value 0.5 representing direct allowed transition, b) for m value 1.5 representing direct forbidden transition	62
Figure6. 18 Schematic diagram showing the energy band diagram of the three samples	62

Figure 6.19a) S5 I-V characteristic curve recorded in the dark condition from +10V to -10V in both forward direction and reverse direction, b) schematic diagram for the connection set up 63

Figure 6. 20 S5 I-V characteristic curve recorded in the dark condition from +10V to -10V in both forward direction and reverse direction, flipped configuration..... 64

Figure 6. 21 S5 I-V characteristic curve recorded under irradiation condition from +10V to -10V in both forward direction and reverse direction and schematic diagram for the connection set up and the source-sample configuration 64

Figure6. 22 S5 dark measurement comparison before and after radiation 65

Figure 6.23 effect of giving the sensor a prime dose on the Dark current 66

Figure 6. 24 S6 I-V characteristic curve recorded under dark and irradiation condition from +10V to -10V in both forward direction and reverse direction and schematic diagram for the connection set up and the source-sample configuration..... 66

Figure 6. 25 S7 I-V characteristic curve recorded under dark and irradiation condition from +10V to -10V in both forward direction and reverse direction and schematic diagram for the connection set up and the source-sample configuration..... 67

LIST OF ABBREVIATIONS AND SYMBOLS

CNT	Carbon Nano Tube
MWCNT	Multi Wall Carbon Nano Tube
DLC	Diamond Like Carbon
ta-C	Tetrahedral amorphous Carbon
ta-C:H	Tetrahedral amorphous Carbon Hydrogenated
a-C	amorphous Carbon
a-C:H	amorphous Carbon Hydrogenated
PL-C:H	Polymer Like Carbon Hydrogenated
NCD	Nano Crystalline Diamond
UNCD	Ultra Nano Crystalline Diamond
CVD	Chemical Vapor Deposition
PECVD	Plasma Enhanced Chemical Vapor Deposition
HPHT	High Pressure High Temperature
DC	Direct Current
AC	Alternative Current
DCSF	Direct Current Saddle Field Glow Discharge
RF	Radio Frequency
MW	Microwave
FTIR	Fourier Transformed Infrared Spectroscopy
UV-VIS	Ultra Violet – visible
FTO	Fluorine doped tin oxide

Sccm	Standard Cubic Centimeter Per Minute
VDOS	Vibrational Density Of State
μ	charge carrier mobility
τ	charge carrier life time
e	electron
h	hole
θ	angle

1. Introduction

Diamond based radiation detectors have been attracting significant research interest due to its thermal stability, ultra-wide band gap (~ 5.5 eV), very high breakdown electric field (10 MV/cm) and its high resistance for radiation damage. These unique properties made diamond a very promising detection material in hard radiation environments like high intensity gamma and X-ray fields and heavy charged particles. Diamond is a Carbon allotrope, indicating that, carbon based materials can be an optimum solution for micro-dosimetry and tissue equivalent detectors area of research.

On the other hand, Diamond preparation has many challenges that are being tackled recently. Mainly the preparation temperature and the complexity of the preparation technique. Commonly, Diamond is being prepared by PECVD method at temperatures as high as 850 – 1200 °C which is a very high preparation temperature requiring complexity in the preparation reactor and high cost. Also the most common methods of plasma generation used are microwave and RF plasmas which add more complexity to the system. ¹

Diamond Like Carbon (DLC) and Nano-Crystalline Diamond (NCD) are allotropes of carbon based materials that exhibit a very similar material properties to those of Diamond with the advantage of low preparation temperature and/or simpler plasma generation method and consequently lower cost². In this study, an investigation on the feasibility of using NCD/DLC thin films as radiation detectors was conducted. Samples were prepared at relatively low preparation temperature (200 °C) using the DC Saddle Field Glow Discharge method, which is much simpler than conventional RF and microwave methods.

The main objectives of the thesis are:

- Building a plasma enhanced chemical vapor deposition system with versatile features that enable a control of the preparation parameters over a wide range of values.
- Preparing and characterizing set of carbon based films to draw a map of deposition regions of the equipment
- Investigating selected samples and testing their potential use in the field of Radiation Detection

The thesis is organized as follows: In chapter 1, a brief introduction about the difference between SP^2 and SP^3 bonding structure and related material properties will be given, and the Ternary phase diagram illustrating different types of DLC and finally diamond and nano-crystalline diamond materials will be introduced. In chapter 2, a brief introduction about the interaction of radiation with matter, radiation detection mechanism, i.e. e-h pair generation, and important material properties that affect the charge carrier transport are presented. Chapter 3 presents a brief introduction on the principles of the saddle field glow discharge PECVD technique, carbon film growth and detailed description of the deposition system and its operational procedures. In chapter 4, a brief introduction about the preparation conditions of the samples is given with an introduction of the characterization techniques used in this study (UV-VIS, FTIR and Raman) and a detailed description of the I-V Characteristic set up. In chapter 5, the collected data are presented alongside with comparisons and discussions about the results. Finally, conclusions and recommendation for future work are presented in chapter 6.

2. The Family of Carbon Based Materials

As one of the most available elements in the periodic table, carbon comes with the rank of the fifteenth most abundant element in the earth's crust and the fourth in the universe after hydrogen, helium and oxygen.³ Over the years, carbon has been playing an essential role in the development of human life starting from charcoal in primitive cultures and ending with the tremendous amount of carbon materials applications in the form of nanomaterials nowadays. Carbon can exist in three main allotropies; namely graphite, diamond and fullerene. Furthermore, each allotropy can exist in crystalline and amorphous forms. More and more, the coexistence of different allotropies and/or degree of crystallinity is also being explored which means the carbon has a very big family with a large number of members.^{1, 2}

Starting from zero dimensional material (0D), fullerenes are the only known stable and finite molecular form of carbon materials. They are different from diamond and graphite in this aspect. In other words, diamond and graphite are infinite solid network. On the other hand, fullerenes are a closed structure and finite molecule (zero dimensional material) that exist in the solid phase. Fullerenes has been proven to be a very promising materials in synthetic cosmetics, pharmaceuticals, organic photovoltaics and superconductivity. Fullerene is a family of molecular, geodesic structures in the shape of cage like spheroids. These spheroids consist of sets of pentagons and hexagons with the general composition of C_{20+2m} where m is the number of hexagons and can take values of 0, 1, 2, 3, etc. Figure 2.1 shows the structure of C_{60} which takes the shape of a soccer ball, making it the most symmetrical member in the fullerene family with the most interesting properties.⁵

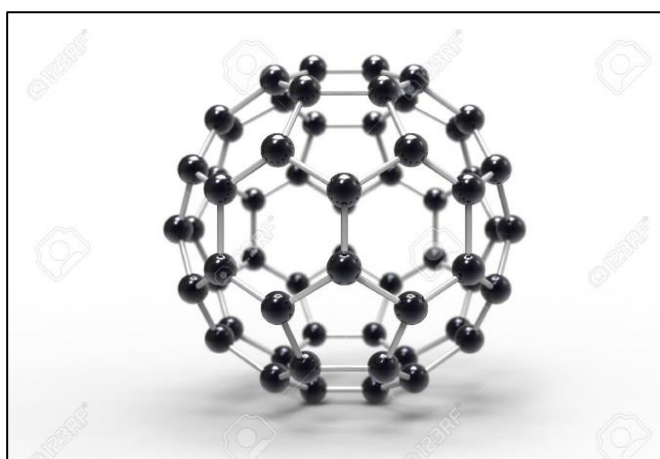


Figure2. 1 The soccer ball structure of C_{60} , the most symmetrical form of fullerene.

On the level of one dimensional materials (1D), carbon nanotubes (CNT) are tubular hollow structures which can exist with one cylindrical coaxial wall known as single wall carbon nanotube (SWCNT) and multiple cylindrical coaxial walls known as multiple wall carbon nanotube (MWCNT). CNT can have diameters in the range of 1-100nm and length starting from few tens nanometers up to few mm. CNT can be thought of being formed by rolling a graphene sheet to produce the cylindrical shape. The properties of the CNTs are highly tunable between metal like conductivity to semi conductivity depending on the diameter to length ratio and the chirality of the SWCNT. Due to its chemical activity, functional groups can be attached to the walls of CNT which make it a very promising material in the area of pharmaceuticals especially drug delivery applications and organic semiconductors^{3,6}

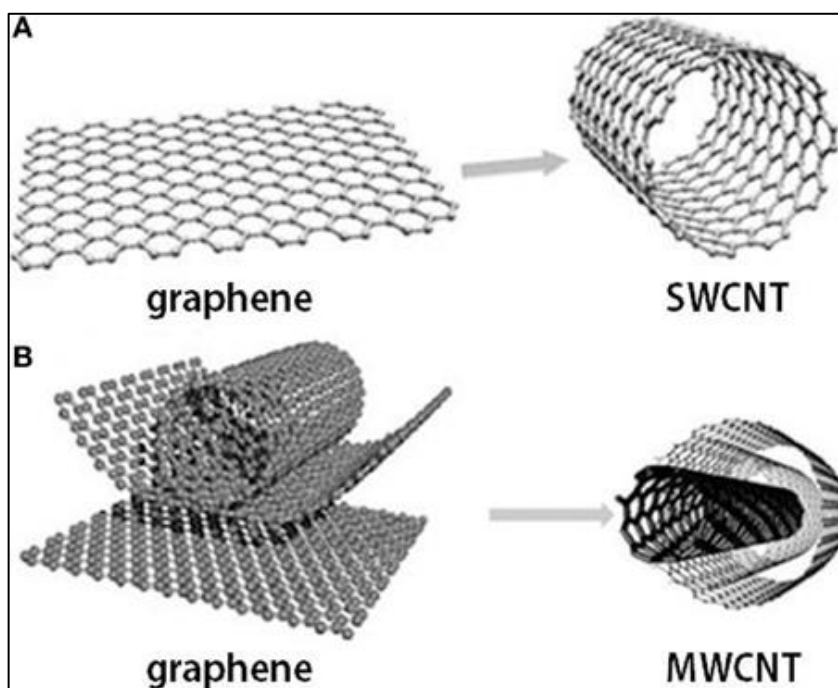


Figure 2.1 Graphene and carbon nanotubes as (A) single wall carbon nanotube (SWCNT) and (B) multi-wall carbon nanotube (MWCNT) structures.⁴

Graphene is the 2D material form of Carbon. It was experimentally discovered for the first time in 2004 by two researchers at The University of Manchester, Professor Andre Geim and Professor Kostya Novoselov who won the Nobel Prize in physics for this great discovery. With the discovery of graphene it was the first time humans actually were able to prepare a two dimensional crystalline material. Graphene consists of a single, one atom thick layer of SP^2 hybridized carbon atoms arranged in a 2D graphitic honeycomb lattice structure. The great interest in graphene came mainly for three reasons. Firstly, its

electron transport, which can be described by the Dirac equation and this allows access to quantum electrodynamics in a simple condensed matter. Secondly, the superior electron transport properties are complemented by a stable chemical and mechanical characteristics at room temperature. And lastly, Graphene can be considered the building block of other dimensional carbon materials. For example a carbon nanotube (CNT) (1D material) can be considered as a graphene sheet rolled over to form a cylinder. Another example would be Graphite (3D material), Graphite can be considered as stacked graphene sheets one upon another and connected together via the Van der Waal weak force.^{5,6}

3D Carbon materials: graphite and diamond are the two opposite allotropies of carbon in the crystalline form. In between them, there exist a wide range of materials with different bonding structure and degree of crystallinity. Carbon materials can exist in the form of: nano-crystalline graphite, amorphous carbon, tetrahedral amorphous carbon and nano-crystalline diamond. In this study the focus of interest is on thin-film carbon based materials, more specifically thin-film diamond and nano-crystalline diamond. In the next sections a quick overview of carbon bonding hybridization and the ternary phase diagram of carbon materials and its related material properties will be reviewed.

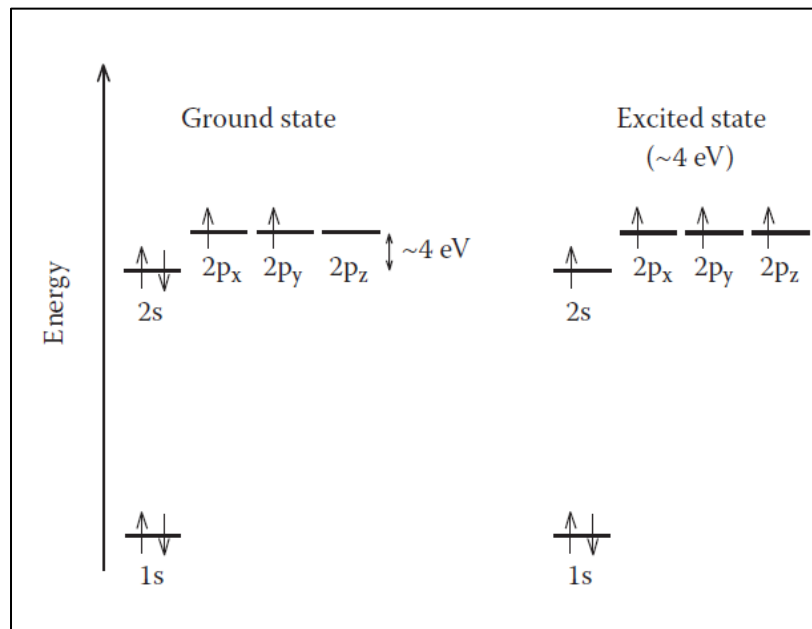


Figure 2.2 Representation of electronic configuration in carbon atom while in ground and excited state¹.

2.1. Bonding Hybridization in Carbon Molecules

2.1.1. The carbon atom

In its elemental form, the carbon atom has an atomic number of 6 with 4 valence electrons in its outer shell which can take the electron configuration of: $1S^2 2S^2 2P_x^1 2P_y^1 2P_z^0$ in its ground state as can be seen from figure 2.3. Also it can be noticed that, the energy difference between the 2S orbital and the 2P orbital is very small ($\sim 4\text{eV}$). As a result, and according to Hund's rule, at room temperature the valence electrons give rise to the electronic configuration $1S^2 2S^1 2P_x^1 2P_y^1 2P_z^1$ denoted as excited state in figure 2.3.

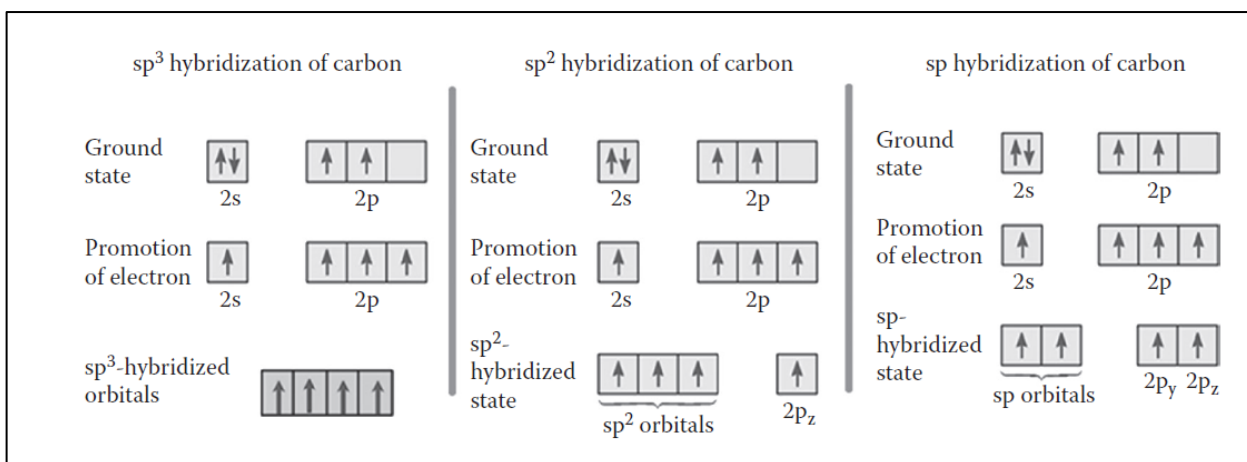


Figure 2.3 Electronic configurations of SP^1 , SP^2 and SP^3 carbon hybridization¹.

Another consequence of the small energy difference between the 2S orbital and the 2P orbital, when compared to the C atom binding energy with its neighbor while forming the molecule is that, the electronic wave functions for these four electrons can readily mix with one another, thereby changing the occupation of the 2S and the three 2P atomic orbitals, so as to enhance the binding energy of a C atom with its neighboring atoms which is known as hybridization. Carbon can hybridize in three forms: SP^1 , SP^2 and SP^3 as can be seen in figure 2.3.³

2.1.2. SP hybridization

In SP hybridization only one electron from the 2P orbital hybridizes with the single electron in the 2S orbital to form one σ orbital while the other electrons hybridize to form π bonds. The resulting molecule is a linear molecule in the perfect case, called carbyne, as can be seen from figure 2.4.^{9,10}

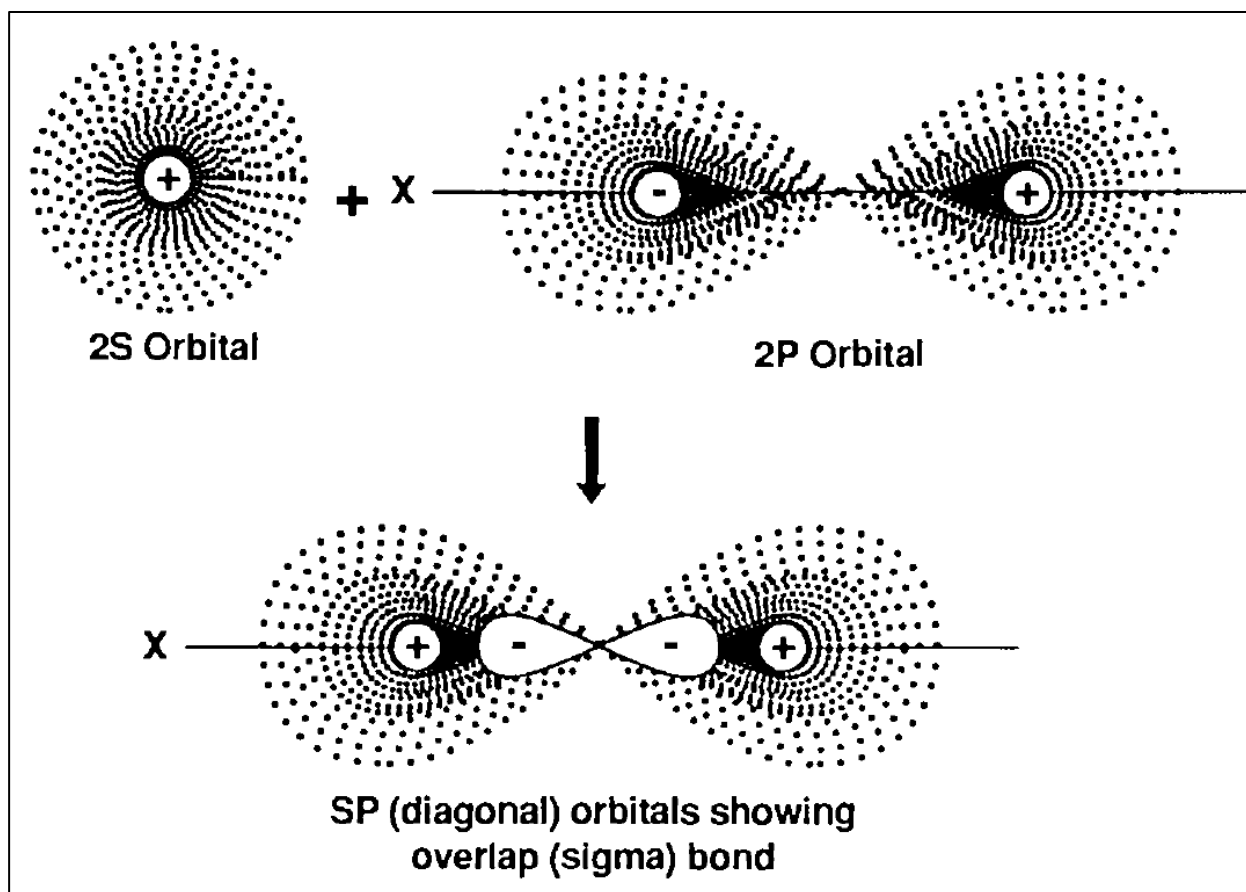


Figure 2.4 Formation of the SP hybrid orbital and SP sigma bond.¹⁰

2.1.3. SP² hybridization (Graphite)

In SP² hybridization two electrons from the 2P (P_x and P_y) orbital hybridizes with the single electron in the 2S orbital to form 3 SP² σ orbitals while the other electrons hybridize to form a π bond as can be seen from figure 2.5 (a). In this case, the in plane (x,y plane) σ orbitals form the strong covalent bonding while in the z axis direction the only bonding mechanism is the weak Van der Waal bonding as can be seen from figure 2.5 (b). Consequently, the carbon atoms arrange themselves in the x-y plane in hexagonal or aromatic rings. Each plane can be considered as a giant graphene molecule and when tying these layers together the graphite in its crystalline form is formed.^{3,4}

Figure 2.5(b) also shows, the overlap between the two P_z orbitals (weak π bonds) in two adjacent carbon atoms which represents the C-C double bond network in a given plane. These electrons can be considered delocalized (free electrons) and uniformly distributed between all the carbon atoms in the that plane resonating between the valence electron. These electrons are what makes graphite conduct

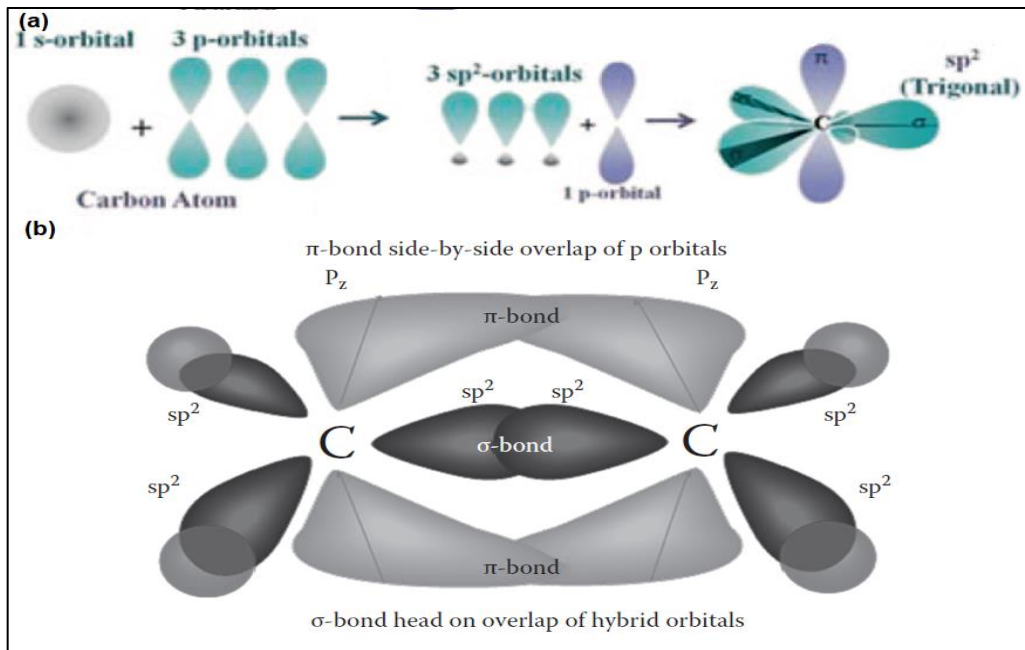


Figure 2.5 (a) SP^2 Hybridization orbitals², (b) in-plane σ bonds and out of plane π bonds¹.

electricity and heat giving it a metal like behavior. Moreover, it makes the layers soft and slippery which makes it an excellent solid lubricant, but also responsible for the tendency of graphite to fracture along planes.^{3,4}

2.1.3.1. Graphite crystal structure

In its single crystal form, the graphite crystal structure is in a stable hexagonal layered structure. The carbon atoms are arranged in a honeycomb lattice with a bond length of 0.142nm. The layers are stacked in the order of ABAB pattern with a lattice spacing between two identical sheets i.e. A&A or B&B of 6.7Å°. The distance between the primed atoms in layer A on one graphene and the adjacent graphene sheet B is half the orthogonal lattice spacing $C/2$ as can be seen from figure 2.6. Due to the short length of covalent bond, a strong chemical bond is formed within the sheet (150–170 kcal/g atom). On the other

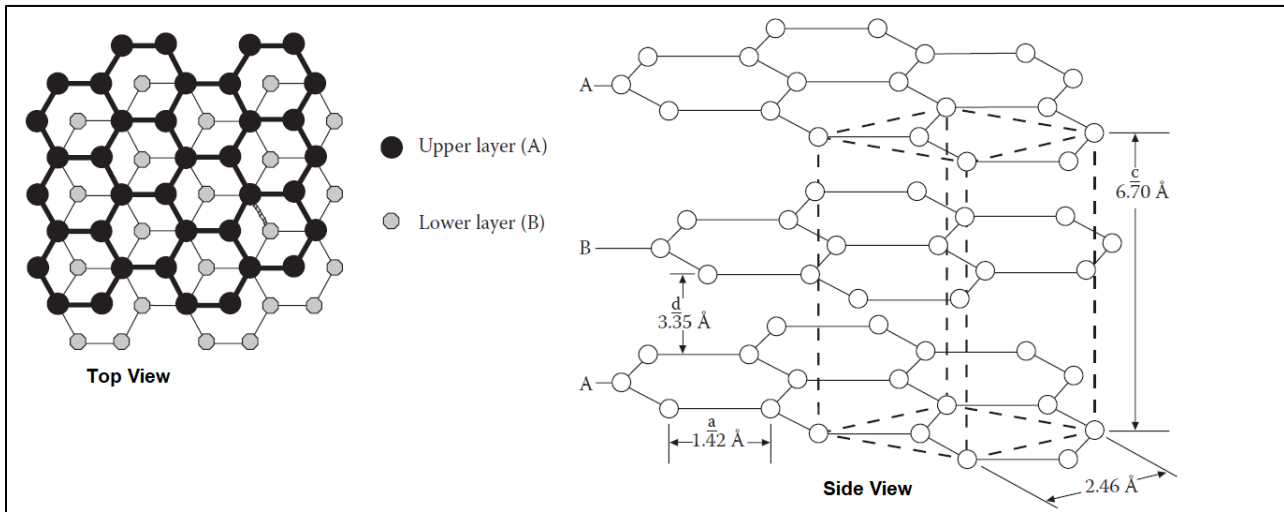


Figure 2.6 The single crystal SP2 bonded structure (single crystal graphite)

hand, the chemical bonding between the sheets is only about 2% of that within the plane (1.3–4 kcal/g atom) ¹¹

2.1.4. SP³ hybridization (Diamond)

In SP³ hybridization all three electrons from the 2P (P_x , P_y and P_z) orbital hybridize with the single electron in the 2S orbital to form 4 equivalent SP³ orbitals as can be seen from figure 2.7. The resulting bonds are 4 equivalent σ bonds with a unique symmetrical tetrahedral structure with the highest electron density compared to the other two bonding mechanisms. The resulting bond is one of the strongest bonding mechanism known. The resultant structure from this bonding mechanism in 3-D is the diamond where the angle between each covalent bond is 109° 28' and the overall symmetry is cubic. ³

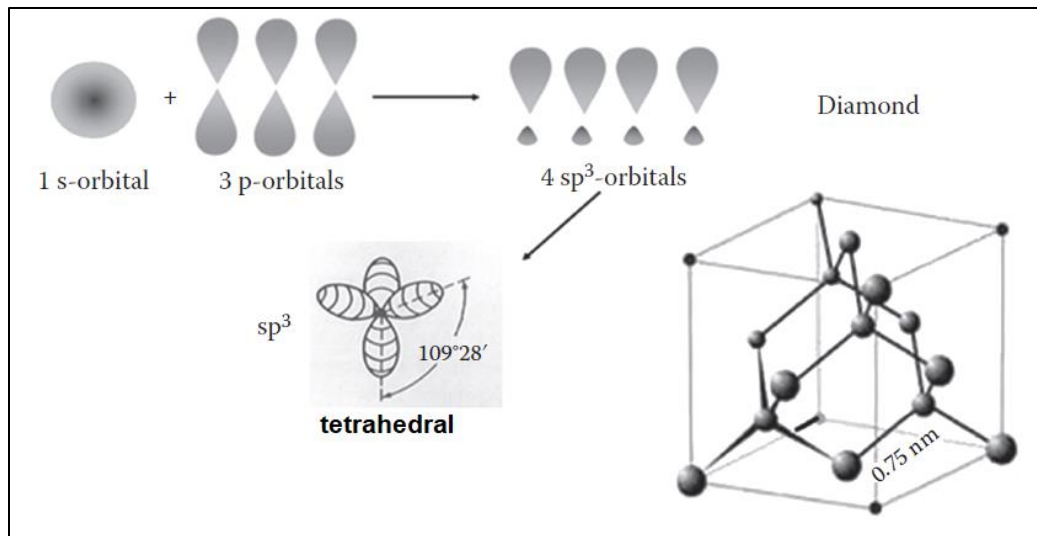


Figure 2.6 SP^3 Hybridization and a cubic cell of diamond structure¹.

2.1.4.1. The Diamond material

Diamond is one of the most outstanding materials known. Due to the unique symmetry in its crystal structure, it exhibits unique material properties that makes it a viable solution in many applications. With the development going on in the world of materials science and materials preparation techniques, diamond can be synthesized in lab both in bulk form and as a thin-film material, with characteristics even better than natural diamond. The strength embedded in the σ bonds in diamond and the high atomic density of $1.76 \times 10^{23} \text{ cm}^{-3}$ leads to diamond having superior physical properties:

- From the mechanical point of view, diamond is the hardest material known, has the lowest thermal expansion and is extremely wear-resistant.
- It is chemically inert
- It has a very high thermal conductivity
- It is highly resistant to radiation damage
- It is optically transparent over a wide range of the light spectrum, starting from far infrared to the ultraviolet region.
- From the electrical properties point of view, crystalline diamond has a 5.5 e.V band gap which puts it on the edge between being insulator and a wide band gap semi-conductor making it very promising in high power electronics and radiation detection. Diamond has fifteen times higher average breakdown voltage than common semiconductors, five times the average mobility and half the dielectric constant of silicon.

A summary of the diamond material properties is presented in Table 2.1

The brief introduction of the two most common allotropies of carbon (graphite and diamond) is quite useful when we try to analyze the “in-between” forms. In the next section, the carbon materials ternary diagram, which represents a map of all non-crystalline carbon materials and their hydrogenated counterparts, is introduced.

Table 2.1 Intrinsic material properties of Diamond at room temperature^{5,12,13}

Property	Average value
Hardness (GPa)	70~150
Density(g cm ⁻³)	3.51
Thermal conductivity(Wcm ⁻¹ K ⁻¹)	24
Bandgap (eV)	5.47
W-value (eV)	13
Breakdown field (MV cm ⁻¹)	10
Displacement energy (eV atom ⁻¹)	43
Electron mobility (cm ² V ⁻¹ s ⁻¹)	1800
Hole mobility (cm ² V ⁻¹ s ⁻¹)	1200
Electron saturation velocity (×10 ⁷ cm s ⁻¹)	2
Hole saturation velocity (×10 ⁷ cm s ⁻¹)	0.8
Dielectric constant	5.7

2.2.The Ternary Diagram

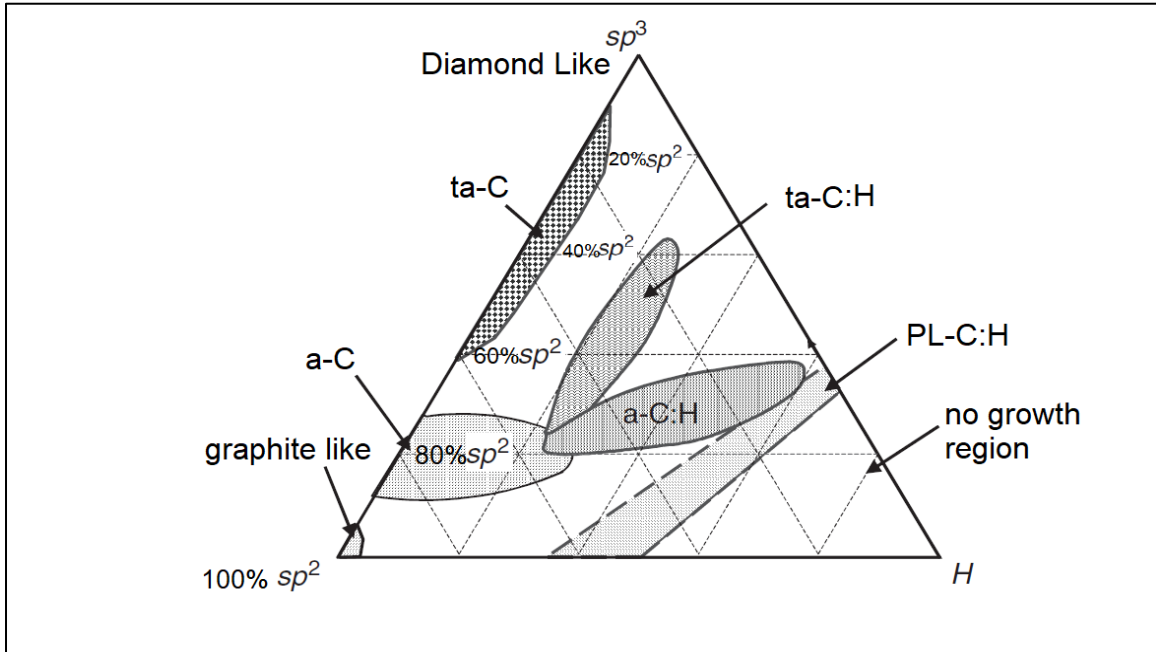


Figure 2.7 Ternary diagram of different carbon materials relating its SP^2 , SP^3 and H content¹⁰.

In its non-crystalline form, carbon can be prepared in a very wide range of forms each with characteristic material properties making carbon thin-films a good and flexible candidates in many applications. During the deposition, in many cases, hydrogen is incorporated with carbon with percentages up to 50%. The resulting film properties is highly dependent on the hydrogen content of the film in addition to the main carbon bonding frame work SP^2 and/or SP^3 relative content. A ternary diagram, presented in figure 2.8, can be used as a graphical representation for the different types of amorphous carbon films and was first introduced by W. Jacob et al.¹⁴ In this section the ternary phase diagram of amorphous carbon materials will be presented alongside the three stage model introduced by Ferrari et al.¹⁵ to explain the amorphisation trajectory from graphite to ta-C.

The key parameters that determine film characteristics are:

- The SP^3 content
- The clustering of the SP^2 content
- The orientation of the SP^2 content
- The cross-sectional nano-structure
- The H or N content

The elastic constants of the film is mainly affected by the SP^3 content alone. On the other hand, films with different optical and electronic properties can be obtained from films with the same SP^3 but different hydrogen content, SP^2 clustering and/or SP^2 cross-sectional nano-structure. ¹⁵

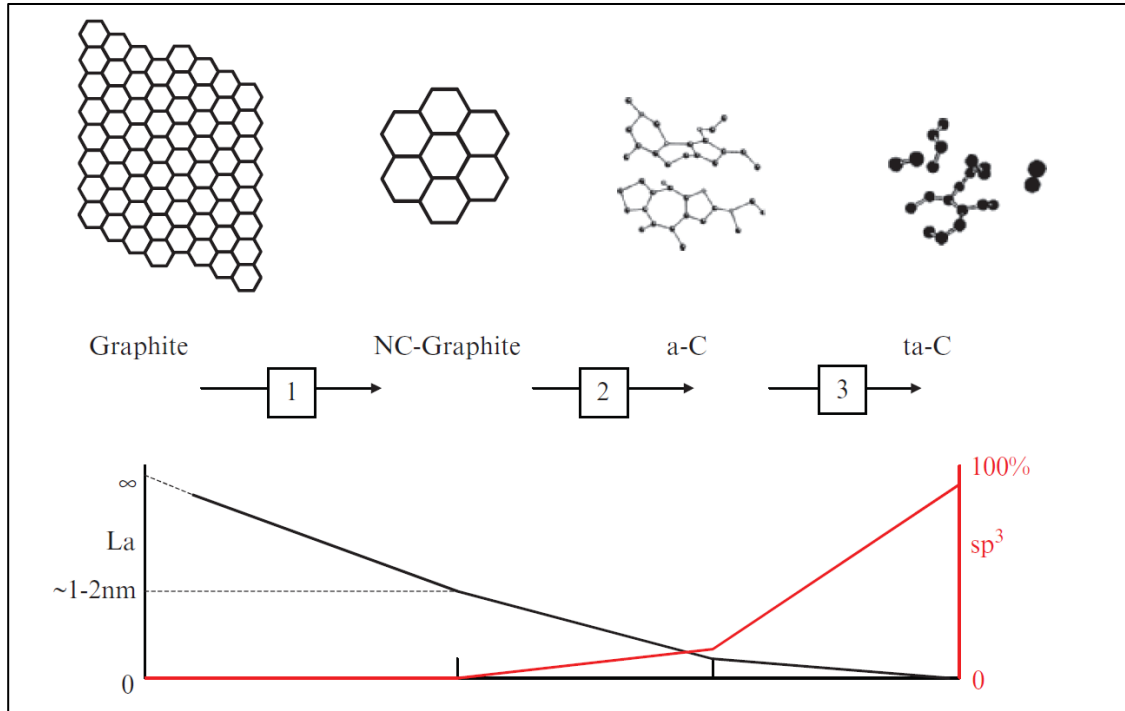


Figure 2.8 The three stage model that explains the amorphisation trajectory of carbon materials and its relation to the SP^2 and SP^3 content. Note that in stages 1–2 to a strong SP^2 cluster size (La) decrease corresponds a relatively small SP^3 increase, whilst the opposite is seen in stage 3. ¹²

As can be seen from figure 2.9, starting from ordered SP^2 (crystalline graphite) the crystallite size La is infinity (single crystal) and the SP^3 content is 0%. With some disordering in the ring shape we are moving through stage 1 and transforming from Graphite to nano-crystalline graphite. In stage 2, more disordering in the SP^2 phase and some SP^3 is introduced (0-20%) (a-C). By introducing more disorder in the SP^2 , we are approaching stage 3 where the SP^3 is significantly increased up to 85% (ta-C). ¹⁵

2.3. Classification of Non-Crystalline Carbon Materials

Graphite-like Carbon: graphite-like carbon is an interesting form of carbon material. On the microstructure scale, graphite like carbon has a material properties in between single crystal graphite and amorphous carbon. It consists of a locally dense graphite-like network, i.e., a predominantly SP^2 -bonded material with reduced inter-planar cluster distances, generating high compressive stress and high local density. It can be prepared with very small SP^3 content (\sim from 0 to 5%) and also can be doped with a very

small amount of hydrogen as can be seen from figure 2.9. Graphite like carbon films usually possess high stress, and good hardness and can be prepared by ion beam-assisted deposition method.^{16,17}

Amorphous Carbon a-C: amorphous carbon films are soft films with SP² bonded framework as a dominant bonding mechanism. It can contain SP³ content with a small percentage (from 0 to ~20%) and/or a relatively small hydrogen content (from 0 to ~45%) as can be seen from figure 2.9. According to Ferrari's three stage model, a-C can be located within stage 2 with a huge disorder in the SP² aromatic ring shape. Usually a-C films possess an electronic band gap less than 1 e.V and 1.6g/cm³ density. The most common preparation technique for a-C is the magnetron plasma sputtering deposition technique, although it can also be prepared via plasma enhanced chemical vapor deposition (PECVD) and DC glow discharge.^{15,16,18}

Amorphous hydrogenated Carbon a-C:H : amorphous hydrogenated carbon is the hydrogenated counterpart of a-C. a-C:H are softer films with higher hydrogen content (from ~40% up to ~85%) and SP² is still the dominant bonding mechanism. The increase in the hydrogen content yields more disturbance in the SP² bonding structure resulting in the ability of higher SP³ content up to ~ 40% as can be seen from figure 2.7. Also, a decrease in the density to 1.3g/cm³ and an optical band gap higher than 1e.V; it can be prepared by reactive magnetron sputtering or PECVD techniques.^{16,18}

Tetrahedral amorphous Carbon ta-C: ta-C or diamond like carbon is a form of amorphous carbon with SP³ as the dominant bonding mechanism up to 85%. According to Ferrari three stage mode, ta-C can be located in stage 3 where the aromatic SP² rings get so disordered until they opens up into linear chains as can be seen from figure 2.10. As a result, ta-C films are very hard films (more than 20GPa) with a relatively wider electronic band gap (2-2.5eV) and higher density (2.4g/cm³). It can be prepared by PECVD, electron cyclotron wave resonance (ECWR), plasma beam source (PBS) and pulsed laser deposition.^{15,18}

Tetrahedral hydrogenated amorphous Carbon ta-C:H : ta-C:H is the hydrogenated counterpart of ta-C. As can be seen from figure 2.9, the incorporation of hydrogen into ta-C resulting in eventual increase in the SP² (up to 70%) content i.e. ta-C:H tends to have higher SP² content when compared to ta-C. As a result, ta-C:H films are softer films (less than 20GPa) with smaller band gap (1-2eV) and lower density (2g/cm³). The most common preparation techniques for ta-C:H films are ECWR and PECVD.^{15,18}

Polymer like hydrogenated amorphous Carbon PL-C:H : PL-C:H is where the hydrogen content becomes significant (40-60%). The remaining carbon content can take SP², SP³ or mixture of both with different percentages. The resulting film is soft with an electronic band gap of 2-4eV and 1.2g/cm³ density. PECVD is the most common method to grow PL-C:H films.¹⁸

2.4. Nano-Crystalline Diamond(NCD)

Due to its superior material properties, single crystal diamond figures in many applications requiring extreme performance. However, two main drawbacks in single crystal diamond obstacle the development in this material. Firstly, the manufacturing cost, as the most common preparation methods are high pressure high temperature synthesis (HPHT) and CVD. The other reason is, the lack of suitable dopants for electronic applications. Recently, nano-crystalline diamond has attracted a lot of attention as it offers many bulk diamond properties in a thin film package or small particle form.^{19,20}

From the ternary phase diagram we can see that, tetrahedral amorphous carbon is the form of non-crystalline carbon that exhibits diamond like properties or in other words, it can be described as amorphous diamond. However, in between single crystal diamond and amorphous diamond or diamond like carbon another category of carbon material comes into the picture, namely nano-crystalline diamond. So the range of crystallinity is the distinguishing parameter between nano-crystalline diamond and diamond like carbon. Starting from complete amorphousness in DLC where the dominant bonding mechanism is SP^3 hybridization but the atoms are randomly distributed without any range of ordering.

Ultra nano-crystalline diamond (UNCD), is a term firstly introduced by Argonne National Laboratory. These films have a range of crystallinity around 5 nm. At this point, grain and grain boundary require definition. The grain is an area or volume over which a regular atomic arrangement can be recognized. In between two grains a group of amorphous atoms separating the two grains from each other is called the grain boundary. So it can be said, UNCD films have a grain size around 5nm with a considerable amount of amorphous grain boundaries and they have similar material properties to Diamond-Like-Carbon (DLC). Nano-crystalline diamond (NCD) on the other hand is where the grain size is more than 5nm and less 100nm. Films with grain size more than 100nm are exhibiting very similar properties to that of bulk crystalline diamond.¹⁹⁻²¹

The grain boundary to volume ratio, is the key parameter to responsible for the characteristics of the resulting film, leading to be either bulk diamond properties or more DLC properties. The existence of the grain boundary also introduces another dimension due to the probability of SP^2 bonding across the grains, which is one of the main differences between carbon and Si. To describe a NCD film, the question is not only how big is the grain size, but also, what is the nature of the grain boundary bonding; is it amorphous SP^3 or amorphous SP^2 ? Also some recent reports have shown NCD decorated with graphene sheets on the grain boundary.^{19,20,22,23}

3. Solid State Radiation Detection

Radiation detection can be defined as, the conversion of the interaction of a specific type of ionizing radiation with an active volume into an electrical signal that is collected by an external electronic circuits. This electronic signal can be interpreted afterwards to be a measure of the ionizing radiation energy and/or obtaining information about its characteristics i.e. counts, type (particle or electromagnetic wave), arrival time, position and direction. Radiation detection has been playing an essential role in the development of many applications. Starting from fundamental sciences in the lab, the progress in radiation detection research yielded better characterization techniques (electron microscope, X-ray diffraction, materials spectroscopy etc). The nuclear industry on the other hand is another area where radiation detection is essential to monitor the radiation levels in nuclear power plants, nuclear fuel manufacturing and management facilities and waste management facilities. Another one of the most important fields where the development of accurate radiation detectors was a primary objective is dosimetry, where it is essential to be able to measure the amount of energy deposited into a specific medium, for example a human tissue, to study and understand the radiation interaction with live cells and consequently determine the safety limits of radiation exposure and to develop the needed radiation dose for a specific treatment in radiation therapy applications. ²⁴⁻²⁶

Ionizing radiation can be classified into two main categories particles and electromagnetic wave. Under the category of particles another two subcategories depending on the charge. So that, a first subcategory is neutral particles for example neutrons and the other subcategory is charged particles which can be divided again into heavy charged particles (alpha particles and protons) and light charged particles (electrons and beta particles). On the other hand, electromagnetic radiation in the scope of radiation detection is usually associated with X- and Y- rays. The active volume or the sensing element in a radiation detector can be in the gaseous state i.e gas filled detector, ionization chamber (Geiger-Müller detector and proportional counter detector), solid state i.e solid state detectors (semi-conductor detector and scintillation detectors) or in the liquid state(liquid ionization chambers and liquid scintillator). ²⁴

Among the three categories of sensing mediums, solid state semi-conductor detectors can provide a privilege of the combination of sensitivity per unit volume, flexibility in packaging, and efficient conversion of ionizing radiation into electrical signals suitable for measurement with modern instrumentation. In this chapter an overview of solid state detection mechanism will be given. Starting

with a summary of the basic mechanisms by which radiation interacts with matter. After that, the basic mechanism of charge carrier production when a solid state sensing element is exposed to radiation is discussed. The important material properties that may affect the charge carrier transport through the medium will also be discussed. And finally, an introduction to diamond based radiation detectors, which is the focus of interest of this study, will be presented. ²⁵

3.1. Interaction of Radiation with Matter

3.1.1. Interaction of electromagnetic radiation with matter

It is interesting that the interaction mechanism by which ionizing electromagnetic radiation may interact with a detection medium does not depend on the phase of that medium i.e. gas, liquid, solid, crystalline or amorphous. What happens after the interaction, however, is highly dependent on the phase of the detection medium. For example: charge pair production can be through ionization process as in gaseous detectors or through excitation process as in solid state detectors. Another example is the charge transport through the detection medium and its collection to the external circuit. Lastly, the number of events (interactions) that take place between the incident photons and the atoms of the detection medium. ²⁴

Photons can interact with matter in one of three basic mechanisms namely photoelectric effect, Compton scattering and pair production. Each type of these interactions has a specific threshold and interaction cross-section. The interaction cross-section and its threshold is mainly dependent on the atomic number of the interacting medium and the photon energy. Figure 3.1 describes the relation between the photon energy and the cross-section of the three types of interactions along with the total interaction cross-section for carbon. ²⁴

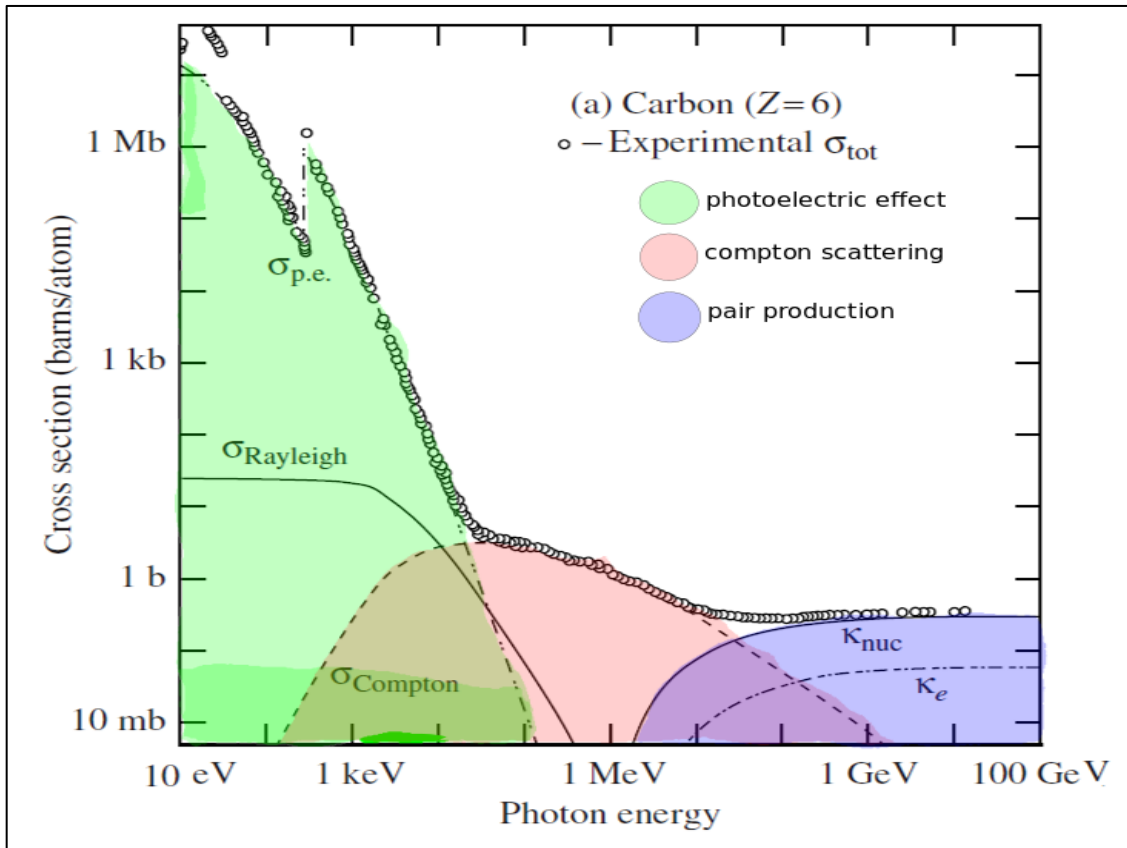


Figure 3. 1 Cross-sections of the three types of interaction mechanism of electromagnetic ionizing radiation as a function of photon energy for carbon. ²¹

Photoelectric effect: the photoelectric effect phenomena was firstly explained by Einstein and it was the first proof of light particle-wave dual nature. The phenomena is quite simple: when light is shined on a material, electrons are emitted. What was surprising at that time is, the emission of electrons did not primarily depend on the intensity of the incident light but on its frequency. In other words, if the frequency of the incident light is smaller than a specific threshold depending on the target material, electrons are not emitted. It was noted that, in this type of interaction a photon is interacting with an atomic electron in the target material with a particle like nature. So, the photon collides with one of the bound electrons losing all of its energy to that electron and knocking it out with an energy equal to the electron binding energy subtracted from the energy of the incident photon. It has been found that the K-shell electrons are the most probable electrons to participate in this kind of reaction. As a result, a vacancy in the K-shell is left after the electron is ejected. This vacancy is then filled with one of the outer shells electrons to stabilize the atom resulting in the

emission of a photon with energy equal to the difference between the two energy levels usually in the energy range of X-rays. This X-ray photon also can knock out an orbital electron called Auger electron.

The probability cross-section of the photoelectric effect is highly dependent on the Z-number of the target material i.e. the higher the Z-number of the target material the stronger the photoelectric effect probability. On the other hand, it is inversely proportional with the photon energy as can be seen from figure 3.1.²⁴

Compton scattering: Compton scattering is the interaction mechanism where an elastic scattering happens between the incident photon and a free electron in the material (or loosely bounded electron) at rest, which is the first difference between Compton scattering and photoelectric effect. Another difference is that, in Compton scattering the incident photon loses some of its energy not all of its energy as in the photoelectric effect, to the electron which suggests multiple Compton scatterings take place until the photon energy is low enough to make a photoelectric effect interaction and disappear.

From figure 3.1 we can see that, the cross-sectional probability of Compton scattering is the dominant when the incident photon energy is in the range between 500 keV and 1 GeV. The reason for this is, for Compton scattering to take place, the photon energy has to be considerably higher than the electron binding energy so that the approximation of the free electron at rest is valid.

The amount of energy lost by the incident photon to the electron in a single Compton scattering depends on two main factors, the energy of the incident photon and the photon scattering angle after the interaction i.e. the scattering process is not isotropic which is a great advantage in spectroscopic applications. Figure 2.2 shows the relation between the change in the photon wave length and its scattering angle. It can be noticed that, at $\theta = 0^\circ$, the change in wavelength is zero which means no energy transferred from the photon to the electron and the maximum change which represents the maximum amount that can be transferred from the photon to the electron is at $\theta = 180^\circ$ which is called back scattering.²⁴

Pair production: pair production is the interaction mechanism which has the lowest cross-section among the three types of interactions that might take place between photons and matter and also has the highest threshold photon energy to happen i.e. the incident photon has to have at least 1.02 MeV for pair production to happen as can be seen from figure 3.1.

Unlike the photoelectric effect and Compton scattering where the interaction takes place between the incident photon and orbital electrons of the material, in pair production the photon disappears and an electron and a positron pair is created instead. This explains the 1.02MeV energy threshold for pair production,

as the incident photon must possess an energy equal to or higher than the rest mass energy of the created particles (electron and positron i.e. double the mass of an electron) and this is the first condition for pair production to happen. The second condition for pair production is that pair production usually happens when the incident photons come in a close vicinity of a heavy particle typically an atomic nucleus. Pair production can also occur in the vicinity of lighter particles, such as electrons. In this case, the process is given the terminology of triplet production or triplet pair production. This process is given that name because, after the disappearance of the incident photon three particles will be sharing the energy of the incident photon. The electron-positron pair that is created from the conversion of the incident photon and the electron which the process happened close to it will also be scattered from its orbital and will consume some of the incident photon energy, for that reason the energy threshold for this process is higher than pair production i.e. 2.04MeV.

In a pair-production, the generated positron usually has a very short life time as it is created in an environment which is typically electron rich. As a result, the positron will combine with an electron from the material and vanish through the process of annihilation creating photons which in turn go through one of the previous two types of interactions (photoelectric effect or Compton scattering).²⁴

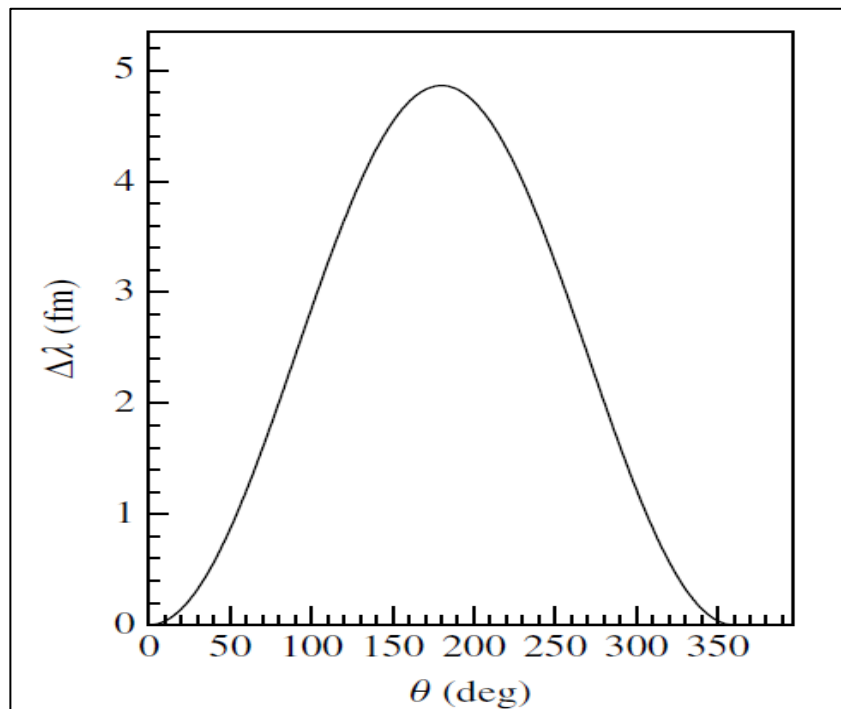


Figure 3.2 The dependence of the change of the incident photon wavelength on the scattering angle in Compton scattering interaction.²¹

3.1.2. Interaction of heavy charged particles with matter

By definition when we refer to heavy charged particles we are referring to particles with atomic weight ≥ 1 such as protons or α particles. Unlike photons, the dominant mechanism by which heavy charged particles interact with matter is through Coulomb force interactions with the electric field of the orbital electrons or with the nucleus. However, the net result of all of these interactions is a reduction of the charged particle kinetic energy. So it is convenient to describe the passage of a heavy charged particle through matter by the term stopping power of the medium. Stopping power is the rate by which a charged particle loses energy per unit length as it passes through the medium. Also stopping power can be understood as a measure for the ability of the charged particle to cause ionizations (through losing energy to the medium) along its track as it is travelling through the medium. It is interesting that, the medium stopping power increases with decreasing energy carried by the charged particle. In other words, as the energy carried by the charged particle decreases the amount of energy lost per single interaction or per unit length of the material increases. As a result, the charged particles lose most of its energy around the end of its track until eventually the charged particle loses all of its energy and comes to rest. This relation is described by the so called Bragg curve which is presented in figure 3.3. As can be seen from figure 3.3, the stopping power reaches its maximum just before the energy of the charged particle drops to zero i.e. just before the charged particle comes to rest.^{21, 24, 25}

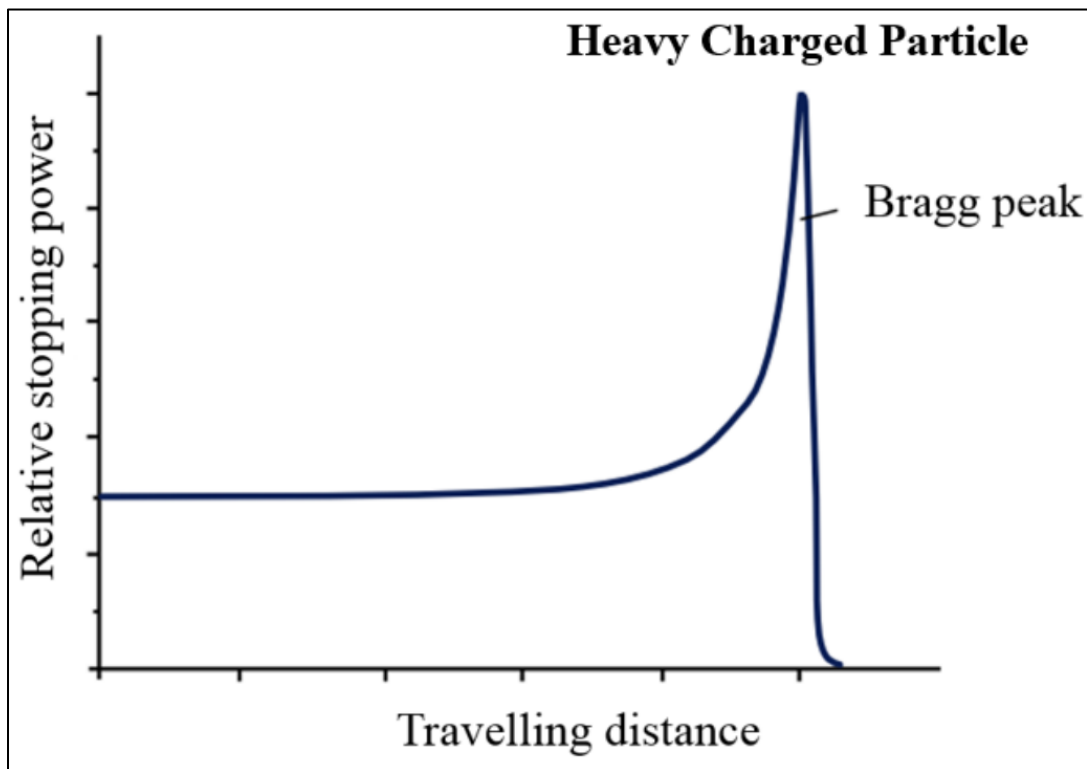


Figure 3. 3 Bragg Curve describing the passage of heavy charged particle through matter²⁴.

3.1.3. Interaction of neutral particles with matter (neutrons)

Since neutrons are chargeless particles they have the ability to travel through the material without being affected by the electric field of the atoms. Alternatively, neutrons interact with matter through strong nuclear force when they come in a close vicinity with the nucleus. The interaction mechanism is mainly dependent on the energy of the neutrons. Slow neutrons (neutrons with energy less than 0.5 eV), may interact with one of two reaction mechanisms namely elastic scattering and nuclear interactions. However, the number of atomic nuclei that has a high probability to absorb the neutron is relatively low. Examples for these materials are helium, boron, lithium, cadmium and gadolinium. Consequently, elastic scattering is the dominant interaction mechanism with slow neutrons. The energy deposited by a slow neutron into the detection medium through elastic scattering is too low to produce electronic signal directly. As a result, the only way to detect slow neutrons is through nuclear reactions where the slow neutron is absorbed by the nuclei and produce a detectable species as a reaction process. Examples for such interactions would include (n, α) , (n, P) or (n, γ) reactions. ^{21, 22}

For higher energy neutrons on the other hand, as the energy of the neutrons increases, the probability of the neutron being absorbed by the nuclei decreases. However, fast neutrons pre-dominantly interact with matter through elastic scattering process with the nucleus. As a result of this collision interaction between the neutron and the nucleus, a proton is knocked on and goes through interactions with the medium as a charged particle. ^{21, 22}

3.2. Solid-State Detection Mechanism

The term solid state detector is most commonly referring to semi-conductor based radiation detectors. As radiation passes through the semi-conductor it loses its energy through one of the mechanisms discussed in the previous section. The energy deposition can cause three distinct phenomena. Firstly lattice excitation, that is where the incident radiation losses some of its energy to the crystal lattice of the material causing an increase in its vibration. Secondly ionization, which is the most important process for detection purposes, in which an electron absorbs the deposited energy by the radiation and jumps from the valence band into the conduction band creating an electron-hole pair. And lastly, atomic displacement which is responsible for what is known as radiation damage. ²⁴

Electron-hole pair creation: at very low temperatures (where the thermal excitation energy is lower than the material band gap) all of the electrons are in the valence band and the conduction band is empty. The outer shell electrons which are participating in the covalent bonds are bound electrons i.e. not free to move. However, at room temperature, when the thermal excitation energy is enough to excite some of the valence

electrons to the conduction band leaving behind an electron vacancy (hole) in the valence band. These electrons in the conduction band are free to move when an electric field is applied creating a relatively small current known as the Dark Current or material noise. When radiation passes through the material and deposits its energy, the process is significantly enhanced creating higher current i.e. the radiation current or signal. It has been observed that, the average energy needed to create e-h pair is independent on the type of the incident radiation but depends on the semi-conductor material and its temperature. As a result, any radiation with energy slightly higher than that needed to create an e-hole pair (note that, the energy needed to create e-h is slightly higher than the material band gap when taking into account the portion absorbed in the lattice vibration) will be able to create e-h which will accumulate and create a charge pulse that can be measured by external electronic circuits. The magnitude of this pulse is directly proportional to the energy deposited by the radiation whereas the number of these pulses represents the intensity of the radiation. Figure 3.4 shows the e-h pair production mechanism in a semi-conductor.^{24,25}

Rather than the transition from the valence band to the conduction band, another transition from an impurity level (an energy level inside the band gap) to the conduction band can be seen in figure 3.4. An energy level inside the band gap can be created from crystal imperfection or from impurities in the material. The existence of such levels enhances the production of e-h pairs which is not a favorable process in ionizing radiation detection because it may introduce nonlinearity in the detector response.

The existence of an energy level inside the band gap opens the chance for an electron to jump from the valence band to that defect level. Now two possible scenarios for that electron may happen. The first scenario is for it to stay for a while in that defect level then jump to the conduction band to complete the e-h pair production cycle. In this case, a time delay in the e-h pair production which causes nonlinearity in the detector response. The other scenario is, this electron will fall back into the valence band and recombine with a hole. In this case no charge pair is produced which also will introduce nonlinearity in the detector response. Hence, the position and the density of these defect levels mainly determines the detector intrinsic energy resolution.²⁴

It is worth mentioning that, the e-h pair production process in semi-conductor detectors is very similar to the production of e-ion pair production process in gaseous detectors. Except, the energy needed to create e-h pair in semi-conductor is on average 4 or 5 times less than that needed to create e-ion pair in gaseous detector. As a result, for the same amount of energy deposited by radiation the amount of charge pair produced in a semi-conductor detector is much higher than that in a gaseous detector. On the other hand, one would expect the amount of noise equivalent charge in a semi-conductor detector would be higher by

approximately the same factor. In fact, this is not the case in most semi-conductors which makes this category of detector far superior than gaseous detectors in terms of intrinsic energy resolution which is a very important property especially in spectroscopic applications. ²⁴

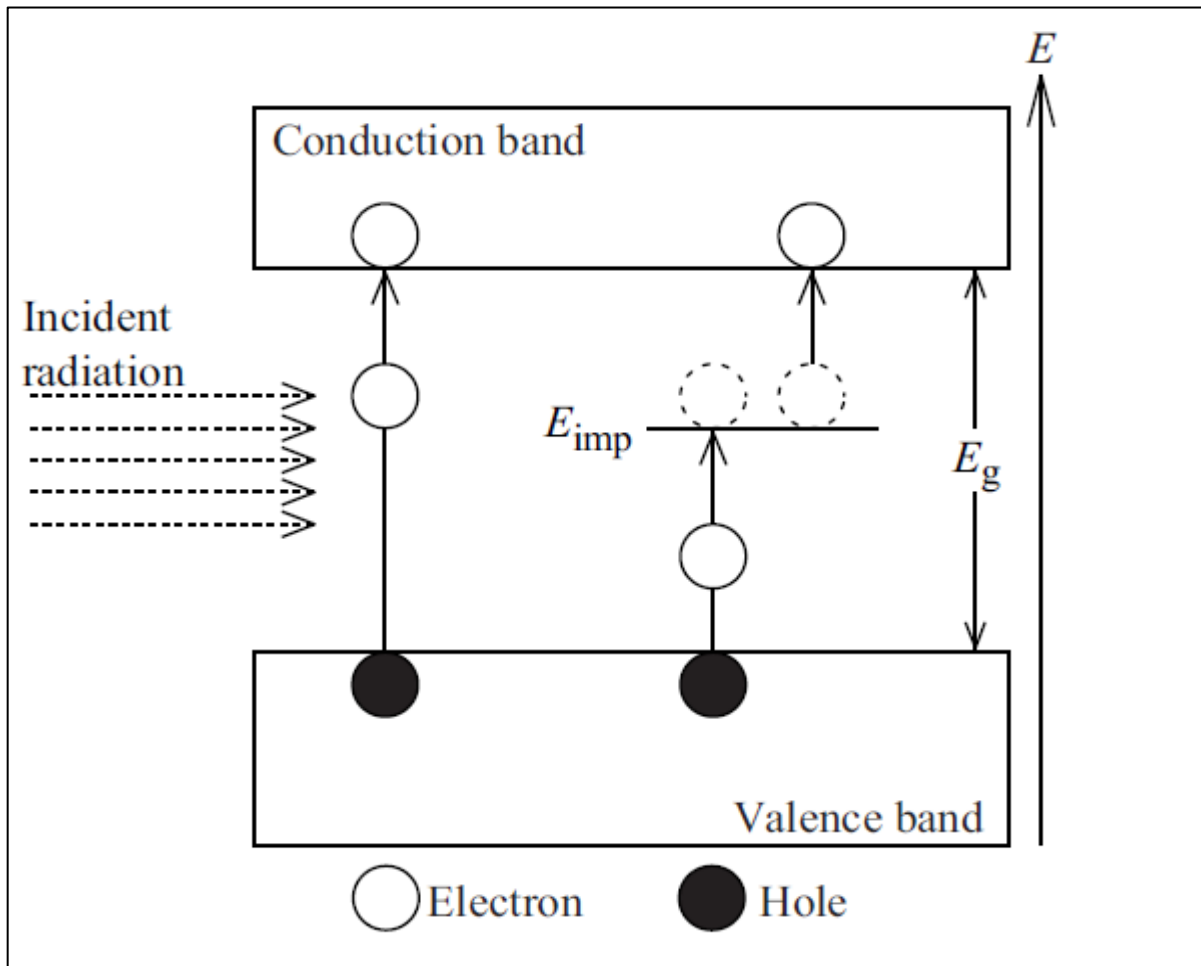


Figure 3. 4 Electron-hole pair production mechanism and the effect of impurity levels in the band gap on the electron-hole pair production process²¹.

3.3. Material Requirements for Solid-State Detection

Charge carrier transport: after an e-h pair creation by absorbing energy from the incident radiation, these charge carriers can be collected at electrodes by applying an electric field. There are two question arising at this point. Firstly, how mobile are the charging carries during their transport from their point of creation to the collection electrodes. In other words, the velocity of the charge carries (cm/s) at a specific applied electric field (v/cm). In practice the term used to describe this property is known as charge carrier’s mobility (μ) with the units $\frac{cm^2}{V.s}$. The other question is, how long an electron will survive before it gets recombined with a hole from an impurity level or fall down into the valence band and the e-h pair get lost. The term used to describe this property is known as charge carrier life time (τ) in seconds.

The quantity ($\mu \tau$) the mobility life time product is an important figure of merit for detector material. A large ($\mu \tau$) product will allow the advantage of fabrication the detector at larger sizes as the charge carriers can be collected over large distances before being lost. In cases where the electrons or holes are not fully collected as in many compound and thin-film detectors, the large ($\mu \tau$) product will means larger electronic signal. ²⁵

Resistivity and noise: one of the most important characters in semi-conductor materials for radiation detection is its resistivity. The collection of charge carriers generated by other means than radiation creates noise in the detector response. One of the most important sources of noise is what is known as leakage current or dark current. Leakage current is the current that flows through the semiconductor when it is biased with an electric potential in the absence of radiation. The higher the resistivity the lower the dark current which means less noise.

The dark current is mainly dependent on the number of electrons in the conduction band. As we are speaking about a semi-conductor, the number of electrons in the conduction band will depend mainly on two parameters i.e. the band gap and the temperature. In that frame, semi-conductor detectors have two categories. Room temperature detectors, where the band gap of the semi-conductor is wide enough to prevent high leakage current and giving an acceptable signal to noise ratio at room temperature. The other category is the cooled detectors, where the detector material has a narrow band gap so it has to be cooled to give acceptable signal to noise ratios. ²⁵

Pulse shape and response time: the accumulation of the generated charge carriers generates an electronic pulse. The response pulse can be characterized by its rise time and the falling time. The rise time is characteristic for the detector material design and its response time whereas the falling time is more dependent on the read out circuitry. A semi-conductor material designed and fabricated to give a fast response permits the advantage of high timing resolution and consequently the ability of separating between two subsequent responses. Many factors may affect the speed of the response such as the device thickness, the charge carrier mobility, the applied biasing voltage, the capacitance of the device and the read out circuitry. The ability to separate pulses determines the maximum useful count rate. ²⁵

Resistivity for radiation damage: one of the most important requirements for a material to be used as a radiation detector is its susceptibility to radiation damage. Radiation induced material damage is mainly due to the atomic displacements that destroys the lattice structure in the material upon exposure to radiation. These defects can aggregate and cluster around the radiation track in the material or may be dispersed creating

point defects. As a result energy defect levels are created and significantly affects the detector performance. One of the parameters that can be affected by radiation damage is the leakage current. Radiation damage can create an increase in the detector leakage current due to the contribution from the created impurity levels. The leakage current's strong dependence on temperature can be a way to get around and compensate for this increase by decreasing the operation temperature which is a common practice with detectors used in hostile radiation environments, such as in particle accelerators, where radiation-induced damage is generally very high.

Radiation damage can also induce a change in doping levels and hence inverting the semi-conductor type (from n to p and vice versa) or create non-uniformity in the doping concentrations. The radiation dose at which such effects become significant varies with material, radiation energy and radiation type. In semiconductors, the effect of damage becomes significant when the concentration of deep and shallow traps in the bandgap caused by the defects created by the radiation approaches the same order of magnitude as the level of dopant added to the material or of other intrinsic defects.^{24,25}

3.4. Diamond Based Radiation Detectors

Due its unique radiation tolerance, diamond is one of the most promising technologies for radiation detection especially in harsh radiation environments and dosimetry applications. Also the ability to dope diamond with hydrogen during its growth makes it very promising candidate for neutrons detection. In this section the typical structure of a diamond detector will be presented and the most important material properties that make diamond a unique detection material will also be reviewed.

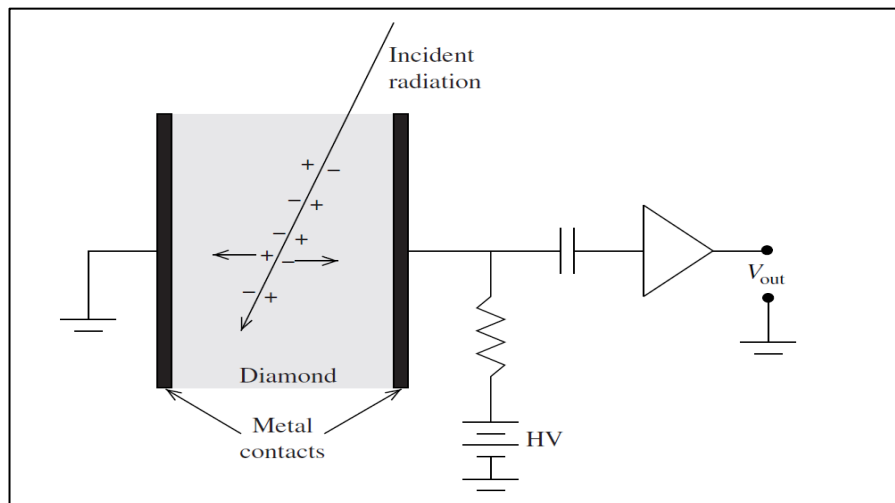


Figure 3. 5 Typical design of simple diamond-based radiation

Table 3. 1 Comparison of some important material properties of diamond and silicon as one of the most popular material used in solid state detection industry¹³

Property	Diamond	Silicon
Mass density (g/cm ³)	3.52	2.3
Dielectric constant	5.7	11.9
Displacement energy (eV/atom)	43	13-20
W-value (eV)	13	3.6
Band gap (eV)	5.5	1.12
Resistivity (Ω cm)	$>10^{11}$	2.3×10^5
Breakdown field (V/cm)	10^7	3×10^5
Electron mobility (cm ² /V.s)	1800	1350
Hole mobility (cm ² /V.s)	1200	480

As silicon is one of the most important materials used in the solid state radiation detection industry, table 2.1 shows a comparison between diamond and silicon material properties.

At first sight on table 2.1, an important property that gives diamond superiority over silicon is the diamond wide band gap which is approximately 5 times the silicon band gap. This wide band gap gives diamond two main advantages as a solid state radiation detection material. The first is the ability to fabricate the diamond detector without the need to create a P-N junction as is the case in most semi-conductors radiation detectors, including silicon, as can be seen from figure 3.5. The other consequence of the wide band gap is the ability to operate the diamond detector in room temperature due to its small dark current. Where on the other hand, most semi-conductor based radiation detectors have to be cooled to low temperatures to have a small dark current value and hence an acceptable signal to noise ratio.²⁴

Displacement energy is another key advantage of diamond detectors. From table 2.1 we can see that, the amount of energy needed to knock out an atom from its lattice position (displacement energy) in diamond is almost two times higher than that in silicon. This makes diamond detectors more resistant to radiation damage which means a longer life time and more suitability for working with harsh radiation environments. Also the lower dielectric constant and the higher breakdown field gives diamond detectors the ability to be operated over wider range of operating biasing voltages and of having lower capacitance for the same biasing volt.²⁴

Also one of the great advantages of diamond is the enhanced electron and hole mobility. This enhances the charge collection efficiency and gives the ability to design diamond detectors with large active volumes. Given that the thermal conductivity of diamond is almost 20 times higher than that of silicon this is also helps prevent internal temperature increase which means more stable electrons and holes motilities.²⁴

4. The Deposition Technique

Plasma enhanced chemical vapor deposition has been extensively used to grow diamond related and carbon based thin films. The characteristics and film growth mechanism is mainly dependent on the type of the plasma used as an activation medium in the chemical vapor deposition process and the preparation condition. RF and microwave plasma assisted chemical vapor deposition are the most successful techniques to deposit diamond and carbon related thin-films so far. However, both techniques have their challenges and complexity. For instance, the working pressure, in both techniques to maintain coupling conditions between the plasma and the wave frequency of the power supply (RF or microwave) is necessary to be limited to extremely low pressure (10^{-3} to 10^{-4} torr). More importantly, the complexity of the power supply as it is necessary to have a matching network between the power supply and the plasma adds more cost complexity to the deposition system. An alternative route to generate plasma with sufficient density for the CVD growth was used. DC saddle field glow discharge exploits the use of a DC power supply which is way simpler power supply than RF and microwave power supplies and semitransparent electrodes to work as an electron confinement method to generate dense plasma for the CVD process. In this chapter, an overview of the Carbon film growth mechanism via PECVD technique will be presented. After that, the principles of the saddle field glow discharge will be reviewed. Finally the system components and its operation procedures will be explained.

4.1. Carbon Based Films PECVD Growth Mechanism

As the name implies, chemical vapor deposition involves a chemical reaction of gas phase reactants on the surface of a substrate resulting in the formation of the thin film. The CVD growth of Carbon based materials is achieved by the activation/dissociation of carbon containing gas precursor while maintaining the substrate temperature at an adequate temperature for the carbon atom to aggregate and start the nucleation process and hence the film growth. The activation step of the gaseous reactants can be achieved by thermal methods such as hot filament (HF), DC, RF or microwave (MW) discharge, or a combustion flame (e.g. an oxyacetylene torch). Figure 4.1 represents a schematic diagram of the process happening during the carbon film growth. As can be seen, the process deals with many fundamental aspects of the CVD, i.e. gas phase chemistry, complex heat and mass transport, nucleation, surface chemistry bulk chemistry and diffusion, and temporal dynamics.^{26, 27}

At first, the process gases mix in the vacuum chamber before starting their transport by diffusion towards the substrate. While the gases mixture is traveling, it passes by the activation medium “the plasma region” which provide energy to the atoms in the gases mixture. This energy causes the molecular species to fragment into reactive radicals, the formation of ions and electrons, and heats up the gas environment into a

few thousand kelvins. At this point, these reactive species continue to undergo a complex set of chemical interactions until they finally approach the substrate surface. Now physical interaction will start to take place. Molecules and ions can be adsorbed and can react on the surface of the substrate, desorb back again into the gas phase, or diffuse around near to the surface until a suitable reaction site is approached. A lot of possible scenarios here lead to a variety of possible outcomes including the formation of diamond, graphite or DLC.²⁹

Many types of gas mixtures have been used as processes gases including acetylene (C₂H₂), acetylene mixed with argon (the most common mixture for microwave plasma enhanced chemical vapor deposition), carbon oxide mixed with hydrogen, pure methane (CH₄), methane mixed with argon and methane mixed with

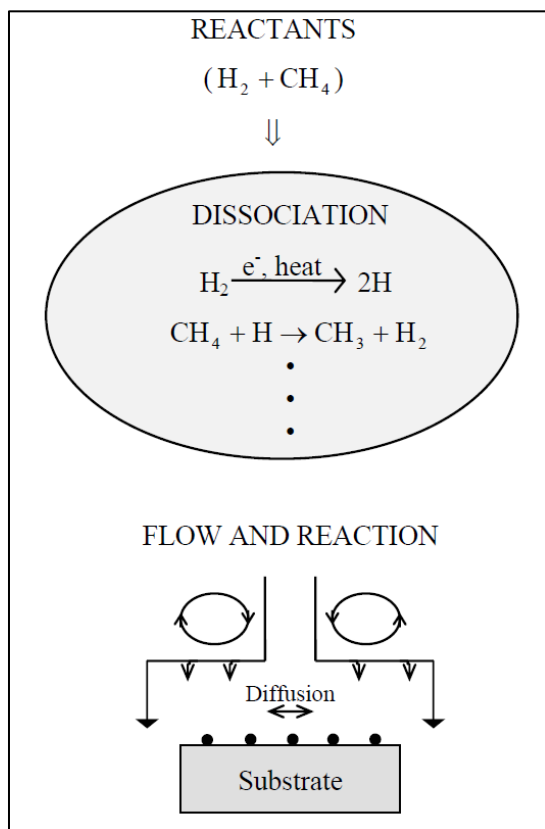


Figure 4. 1 Schematic of the CVD growth mechanism of carbon thin-films²⁷.

hydrogen which is the mixture used in the current study. As can be noticed, all of the gas mixtures necessarily contain hydrogen as hydrocarbons provide one of the source gases. Control of the hydrogen incorporation in the films plays an important role in determining final material properties during the film growth.²⁹

4.1.1. The role of atomic hydrogen

The first important role hydrogen plays during in CVD carbon materials growth during the dissociation step. Upon reaching the plasma region, the hydrogen molecule split into 2 atomic hydrogen species as

explained in figure 4.1. These atomic hydrogen species are chemically active and tends to take another hydrogen from a methane molecule to form H_2 and reduce the CH_4 molecule into CH_3 radical. This reduction process continues on and on until we have single atomic carbon C which in turn start the film growth on the surface of the substrate when the necessary temperature is maintained.²⁹

The other important role occurs during the film formation. The H atoms are very efficient in breaking up long chains of hydrocarbons and prevent the formation of polymers as explained in figure 4.2. Also it is known that, hydrogen atoms are eager to react with and remove SP^2 carbon rather than SP^3 . Hence it prevents the formation of graphitic content on the surface while leaving the diamond clusters behind.²⁹

Finally, H is crucial for the termination of the dangling bonds at the surface. The bulk of diamond is fully SP^3 bonded in crystalline form. However, at the surface dangling bonds are formed which needs to be terminated in some way to prevent cross-linkage and subsequent reconstruction to the graphite form. This termination is performed by hydrogen atoms or sometimes by HO radical which helps stabilizing the diamond lattice.²⁹

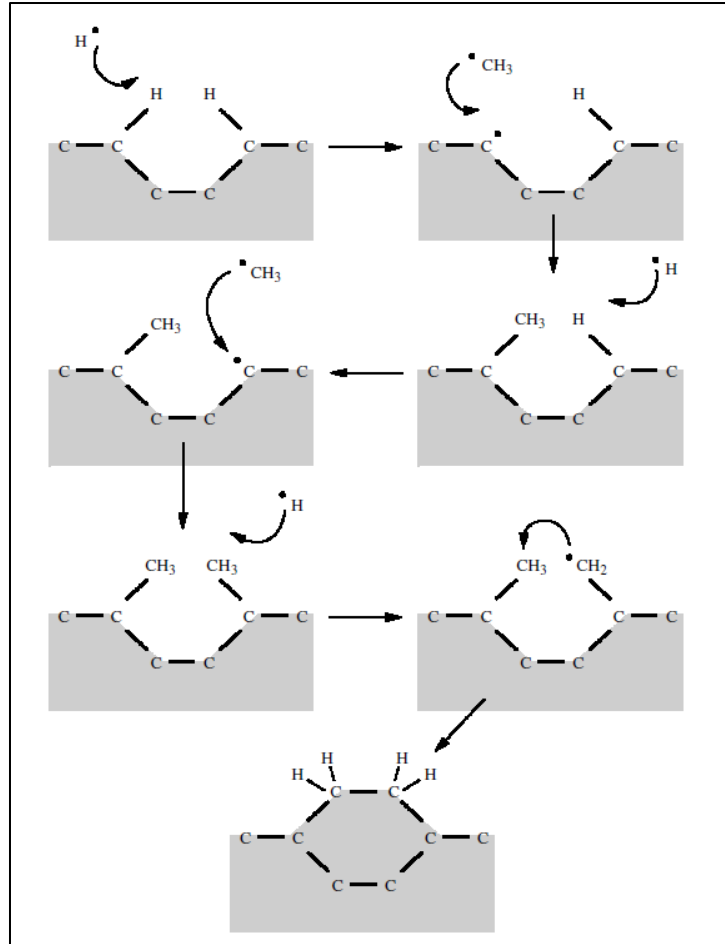


Figure 4. 2 Schematic of the reaction process occurring at the diamond surface leading to stepwise addition of CH₃ species and diamond growth.²⁶

4.1.2. Film nucleation

The growth of diamond films starts when individual carbon atoms start to nucleate on the surface substrate in an atmosphere that encourages the initiation of the tetrahedral SP³ bonding lattice. There are two types of growth process for diamond films, namely homo-epitaxial growth and hetero-epitaxial growth depending on the substrate type. In homo-epitaxial growth, the substrate is natural diamond. In this case the substrate is providing a growing template for the tetrahedral network and the diamond lattice is just extended atom-by-atom as deposition proceeds.²⁹

In the hetero-epitaxial growth, on the other hand, this template is not provided for the C atoms to follow and all the non-diamond forms of carbon that deposit on the substrate surface are immediately etched back to the gas phase by the hydrogen. Consequently, the initial induction period of diamond is prohibitively low (hours or even days). Alternatively, substrate pre-treatments can be made to enhance the diamond growth.²⁹

Example of the pre-treatments that can be made for the substrate surface to enhance the diamond nucleation can be: abrasion of the substrate surface by mechanical polishing using diamond grit ranging in size from 10 nm to 10 m where this pretreatment can enhance the diamond nucleation by creating surface scratches suitably shaped to work as growth template, contamination of the surface by a nanometer sized diamond crystals which act as crystal seeds, or both.²⁹

4.2. The principle of DC Saddle field glow discharge

As mentioned earlier, the plasma provides the activation/dissociation environment that is necessary to provide sufficient energy for the reactant species. To obtain this, the plasma temperature needs to be elevated to high temperatures. This can be done by increasing the path length of the electrons in the glow discharge, also referred to as the electron confinement. The motivation for increasing the path length of the electron is to give the electrons the chance to make more collisions with the gaseous atoms and hence inducing more ionizations and increasing the temperature of the medium. Many techniques have been employed to increase the electron path length in the field of plasma applications, such as applying magnetic field, like in the plasma magnetron sputtering technique so that the electron would take a helical path rather than straight line. Another example would be the use of high frequency alternating electric field (RF or microwave) so that the ions will not sense the change in polarity because its heavy mass makes them less responsive while the electrons, which are way lighter than ions, will start to oscillate following the alternations in the polarity of the magnetic field.³¹

Another method to extend the path length of the electrons in plasma by means of oscillation is the saddle field configuration. The idea is quite simple: we use a semitransparent electrode with a relatively high

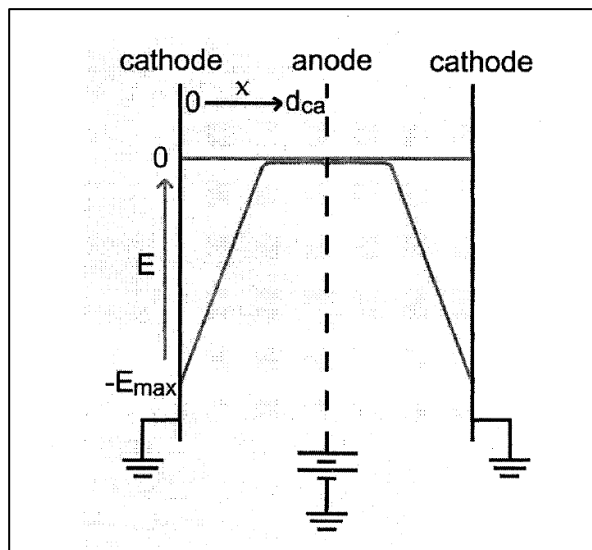


Figure 4. 3 DC saddle field configuration in its basic form²⁹.

potential with respect to other blank/semitransparent electrodes or the vacuum chamber. Consequently, the electron will be repelled by the low potential electrode toward the high potential one (the semitransparent electrode) but when it arrives the semi-transparent electrode will let the electron go through the other side by its momentum until it gets repelled from the low potential on other side, thus reversing its direction toward the high potential again. This oscillation process will continue going on until the electron is lost in a recombination reaction or so. As a result of this oscillation process the electron will have the chance to make more ionization events and raise the temperature of the plasma. Figure 4.3 shows a schematic of the saddle field configuration in its basic form.³²

The saddle field configuration has two main advantages when compared to the RF/MW plasma techniques. First of all is the simplicity as simple direct current power supply will be enough to maintain the plasma without the need for complicated matching network as the case with RF/MW power supplies. Wider ranges of operating pressure and the versatility of compromising between the deposition rate and the uniformity over large areas of deposition depending on the number of semitransparent electrodes used.^{31,32}

There are three configurations that are commonly used for the generation of the saddle field i.e. triode, shielded triode and pentode. In the triode configuration, see figure 4.4a, a highly asymmetric saddle field is generated between the semitransparent anode and the two substrate holders with higher plasma intensity in the right half. This configuration has the advantage of high deposition rate when compared to the other two configurations but less deposition uniformity over large areas. In the shielded triode configuration, see figure 4.4b, another semitransparent electrode is used so that the plasma will be shielded between the two electrode and the back substrate holder. In other words, the substrate holder has been shielded from the plasma. as a result the deposition rate is less but it has the advantage of uniform deposition over large area due to the large distance between the plasma and the deposition region. Finally the pentode configuration, which is the configuration used in this study, is using three transparent electrodes to produce symmetrical saddle field while keeping the substrate out of the plasma region in order to better control the incident ion energy.³²

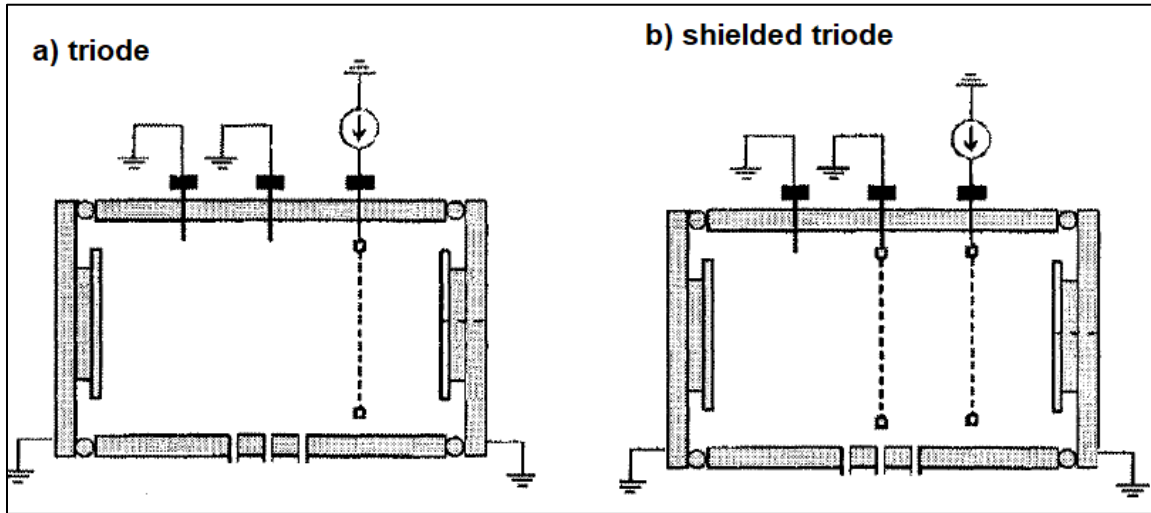


Figure 4. 4 a) Saddle field triode configuration, b) Saddle field shielded triode configuration²⁹.

4.3. The experimental Set up

In this project, the SFGD plasma enhanced chemical vapor deposition was built from scratch. The experimental set up consists of vacuum system, gas feeding system, substrate holder and power delivery system. Figure 4.5 shows a schematic diagram of the experimental setup and its components.

4.3.1. The vacuum system

The vacuum system consists of the following component: the vacuum chamber, mechanical pump, turbo pump, low vacuum gauge, high vacuum gauge, butterfly valve, high vacuum isolation valve, and baking out heaters. The vacuum chamber is a horizontal cylinder made of high grade stainless-steel with inner volume of approximately 15L and two load lock gates one at each side with a diameter of 26cm. the mechanical pump, a Leybold Heraeus Trivac D16A Rotary Vane Dual Stage Vacuum Pump, was responsible for providing the necessary initial vacuum level to initiate the turbo pump during the startup stage, and then backing out behind the turbo pump while the turbo pump is running.

The turbo pump used in this work is PFEIFFER TMU71 with TC600 motor driver and DCU 100 control unit. The turbo pump is one of the most sensitive and expensive items in the system which needs to be handled carefully. The operational region of the turbo pump starts from vacuum level around $5 \cdot 10^{-2}$ torr and is responsible for approaching the ultimate vacuum level which was $8 \cdot 10^{-6}$ in this work.

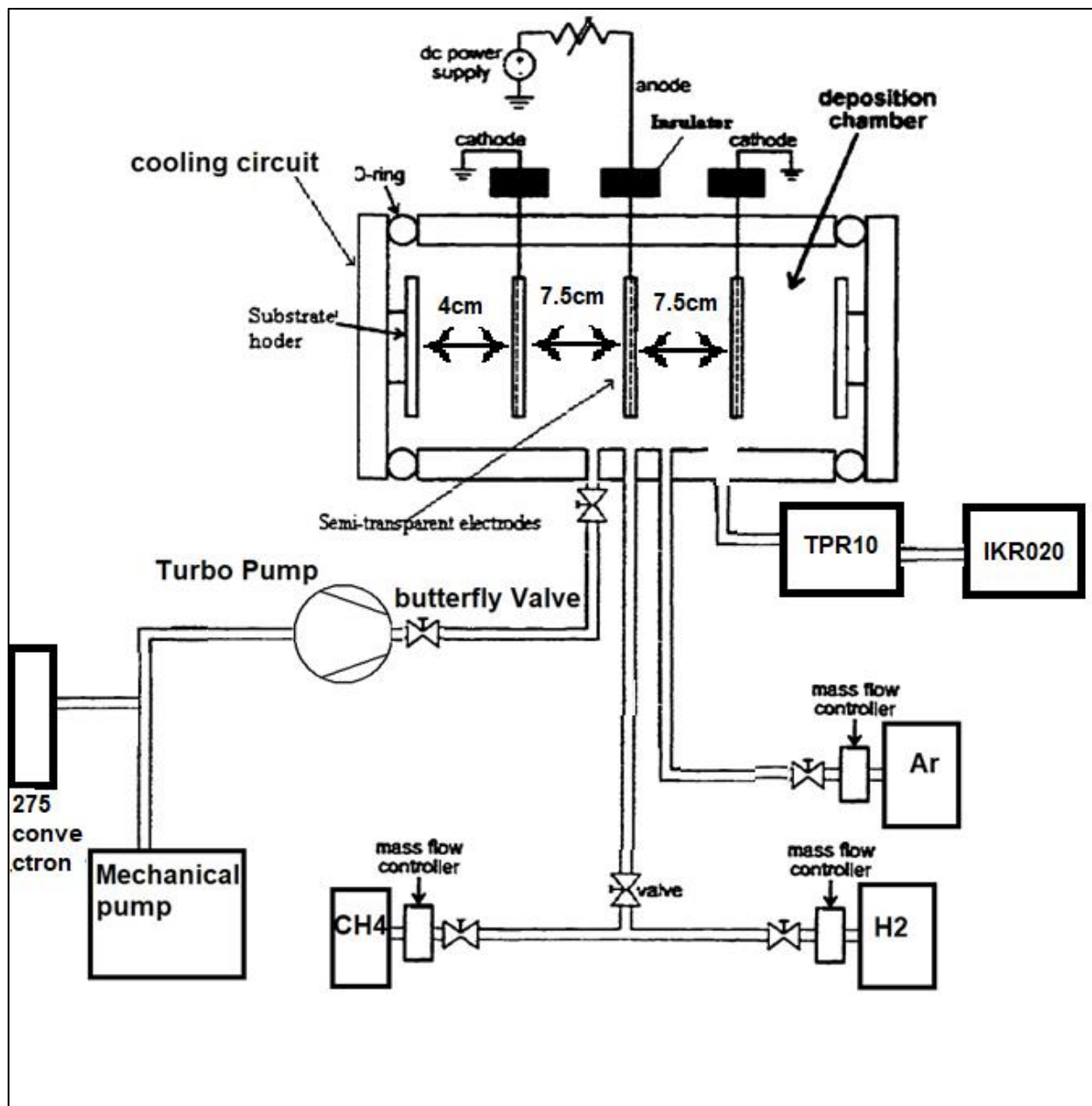


Figure 4. 5 Schematic diagram of the experimental set up and its components.

To measure the vacuum level in the system three vacuum gauges were distributed in different spots in the system. On the fore line between the turbo pump and the mechanical pump, a low vacuum gauge (275 Convectron gauge with its display unit) was used to monitor the backing efficiency of the mechanical pump and to ensure the vacuum level didn't exceed the safety operation of the turbo pump. Using the controlling unit Balzers TPG300, another two gauges were mounted to measure the vacuum inside the chamber. A low

vacuum gauge model TPR10 (from atmosphere to 10^{-3} torr) and a high vacuum gauge model IKR020 (from 10^{-3} to 10^{-8} torr) as can be seen from figure 4.5.

The butterfly valve, is not an elementary component in the vacuum system but yet its existence add a great versatility in the operation of the system. The main idea of the butterfly valve is to control the pumping speed of the turbo pump and consequently it gives the ability to extend the operation region to high pressures without threatening a turbo pump failure. Another great advantage is the ability to play around the total operating pressure and the gases mixing ratio i.e. increasing the gases mass flow rate while keeping the pressure constant and/or increasing the operating pressure while keeping the mixing ratios constant. The butterfly valve controls the pumping speed by changing the cross-sectional area of the exposure window between turbo pump and the system. It does so by controlling the position of a rotatable circular disc rotating around its vertical axis to ensure the homogenous pumping out of the pump as can be seen from figure 4.6. An MKS butterfly valve 253B series controlled via MKS-252C controller and readout unit was used in the current



Figure 4. 6 Two photos of the butterfly valve showing its totally closed position and totally opened position.

study controlled via and readout unit. It controls the valve to put it in 100% opened (totally open), 0% opened (totally closed) or partially opened (any value between 0 to 100%) positions. In some advanced systems, it is also possible to control automatically the position of the butterfly valve by connecting it to the vacuum gauge and the mass flow controller of the gases.

It should be mentioned that, the butterfly valve is not high vacuum sealed. Which means that, when it is fully closed the turbo pump is still affected by the pressure inside the chamber. Therefore an isolation valve is used, that is high vacuum sealed valve, which when closed, separates the turbo pump from the system. The isolation valve is important to protect the turbo pump against any sudden increase in the system pressure and

during the system shutdown procedures, when the turbo pump is slowing down and the vacuum inside the chamber is approaching atmosphere.

Another common component with vacuum systems is represented by the system baking out heaters which are used to establish a higher level of ultimate vacuum and hence impurities free environment. The idea is that, while evacuating the vacuum chamber its walls will start to outgas impurities trapped in between the atoms due to the reduced pressure. To enhance and accelerate this out gassing process, the walls are normally heated to typically 100-120°C. In the current study, the system was baked out using heating strips rounded around the body of the system as shown in figure 4.7. The backing out procedures are as following:

- The system is first pumped down to the highest approachable vacuum by the turbo pump.
- The backing out heaters are turned on, the temperatures of the walls and sensitive points in the systems (joints, vacuum gauge ports or any point that contain any element not rated to that temperature) are monitored with thermocouples and temperature readout unit (Omega, model 115KC)
- An increase in the system pressure will be noticed at the beginning due to the increase in the gaseous molecules energy but once saturation is approached the pressure will start to slowly go down again.
- The system should be held at this temperature for the same amount of time as it took to approach its ultimate vacuum then the heaters should be turned off and the system should



Figure 4. 7 System baking out heaters.

be left to cool down to room temperature and approaching its new ultimate vacuum level.

4.3.2. The gases feeding system

The gases feeding system consists of one individual gas line for argon gas supply, one individual gas line for compressed air supply, two connected gases lines via a mixing point for hydrocarbon gases supply, a set of pneumatic valves distributed in different location in the system controlled by a set of electrical relays and three mass flow controllers to control the argon and hydrocarbons gas lines.

The argon line, is controlled by the unite high performance mass flow controller model UFC-1200A, a unite readout unit model URS-100, and a pneumatic valve isolating the line from the chamber to avoid any sudden increase in the chamber. The argon gas line was used for the plasma testing during the system initiation and to perform regular plasma cleaning for the system.

The hydrocarbons supply is represented by, a hydrogen gas line and a methane gas line connected through a mixing point, which was used to establish the hydrocarbon/hydrogen gases mixture. Each line was controlled by an MKS precision mass flow controller model 1197A and an MKS controller/readout unit model MKS247 which can control up to four gas lines. A pneumatic valve was located directly in front of each mass flow controller to work as a shut off valve and prevent intermixing between the gas lines. The mixing point was located far enough from the vacuum chamber port which also isolated by a pneumatic valve to ensure gasses homogenous mixture before approaching the vacuum chamber.

The pneumatic valves, Swagelok model ss-4BK-TW-1C were used in the system controlled by Honeywell orifice electrical relays to set the valves on and off. Pneumatic valves are on/off type valves that is normally closed and it opens when it receive sufficient compressed air pressure. The pneumatic valve is typically connected to the compressed air line through an electrical relay which has an orifice that opens when it is given the required electrical signal, hence allowing the compressed air to hit the pneumatic valve to put it in the open position.

4.3.3. The substrate holder

As mentioned earlier, the vacuum chamber has two load lock gates, one at each side. One of them has been used as substrate holder as shown in figure 4.8, while the other is used to lock the other side of the chamber. The substrate holder has three main functions. The first is to hold the substrates inside the vacuum chamber during the film deposition. A heater is used to provide controllable heating supply to maintain the substrate at the desired temperature during the deposition. A cooler is used to maintain the load lock sealing

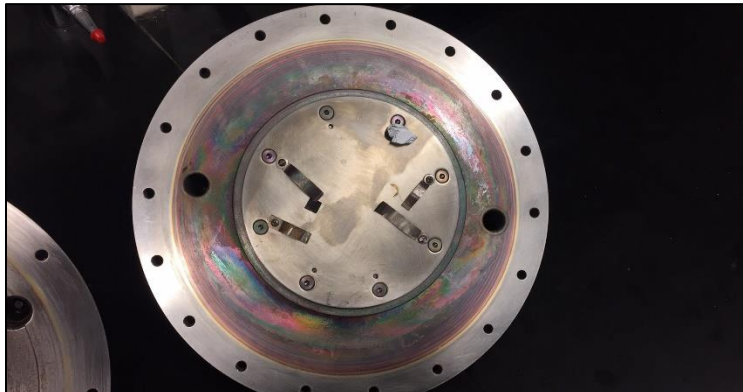


Figure 4. 8 The substrate holder showing the heater mount and clamps to fix the substrates.

O-ring at sufficiently low temperature to not expand or melt while heating the substrate and to cool down the substrate to room temperature after turning off the heater.

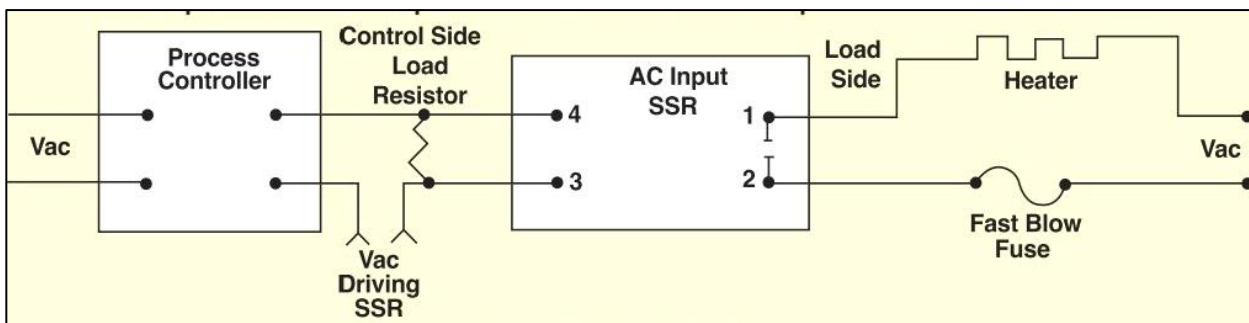


Figure 4. 9 Substrate heater connection diagram.

The heater controlling circuit was established following the diagram shown in figure 4.9. The process control used is an Omega temperature controller CN8500 series connected with solid state relay Omega model SSR240AC50. The substrate temperature was measured using a K-type thermocouple passing from the vacuum to the non-vacuum side using Ideal-Vac feedthrough flange part number P108110 to provide the temperature feedback for the temperature controller unit. On the other hand, the temperature controller compares the feedback temperature with the set value previously specified by the user. Depending on the



Figure 4. 10 Substrate heater electrical connection.

difference between these two values the controller starts to give the order to the solid state relay through ports 3&4 to make an open/closed cycles between the two terminals 1&2 on the solid state relay side, which is connected to the rear side of heater as shown in figures 4.9 and 4.10.

4.3.4. Power delivery system

As mentioned earlier, the saddle field configuration used in the current study is a pentode configuration with three semitransparent electrodes separated from each other by 7.5cm and from each load/lock gate by 4cm as can be seen from figure 4.5. The outer two electrodes are grounded while the middle electrode is connected to Spellman DC power supply SL600 series with a shunt 500 Ω resistant connected in series to prevent the in-rush current that flows at beginning of the plasma ignition.

5. Experimental Work

In this chapter the experimental activities performed in this study will be presented. The chapter is divided into two sections, in the first section the samples preparation steps will be presented whereas in the second section a quick glance on the characterization techniques will be presented alongside with a description of each characterization equipment used in this study.

5.1. Samples Preparation

The main objectives at this step of the project, after building the PECVD system that is capable of depositing carbon based thin-films with a wide range of deposition parameters, was to prepare a set of carbon thin-films to draw a map of deposition regions of the equipment. Based on the microstructural characteristics of the prepared samples, some samples were selected for further investigations and for testing their potential as radiation detector materials. Samples preparation can be divided into five main steps: substrate selection, substrate cleaning, pre-deposition gold coating for selected samples, carbon film deposition and finally post-deposition for selected samples.

5.1.1. Substrate selection

All of the samples were prepared at the same substrate size which is 2cmx2cm, however different types of substrate materials were used in each deposition experiment to suite the different types of characterizations needed. Samples were characterized by four techniques, namely: Raman spectroscopy, Fourier Transform Infrared spectroscopy (FTIR), UV-Visible spectroscopy (for selected samples) and I-V characteristic under irradiation and in dark conditions(pre- and post-irradiation).

For the Raman spectroscopy and FTIR measurements, the main selection rule was the transparency of the substrate material in the infrared light region and its thermal stability at the deposition temperature. Single crystal silicon substrates with one sided polishing (100) orientation were used for these two measurement. For the UV-Visible spectroscopy the objective of the measurement was to determine the carbon film optical band gap. For this reason the substrate selected for this measurement should have a sufficiently wider band gap to ensure the absorption of the light will happen in the film without being affected by the substrate. Therefore, fused silica substrates, purchased from MTI Corporation item number SOF101005s1, were used for this measurement.

For the I-V characteristic and radiation response experiments, the carbon film needed to be sandwiched between front and back metal contacts as shown in figure 5.1. Two types of metals, gold and fluorine doped tin oxide (FTO) coated glass were used in this study as back electrode to investigate the

dependence of metal interface with the carbon film on the metal material. For the gold contact, thin gold films were deposited on single crystal silicon substrates using TED PELLA, INC. sputter coater model 108 auto. Glass coated FTO substrates were purchased from MTI Corporation (item number FTO252511TEC7gp25e). After depositing the carbon film on the back contact, another thin gold layer was deposited on the surface of the carbon film taking careful consideration to mask the back contact film to avoid short circuit between the two electrodes.

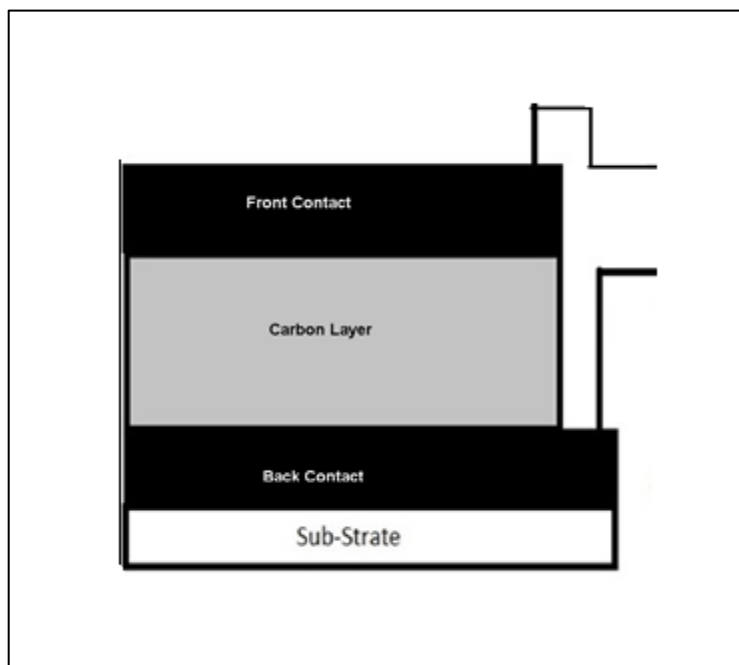


Figure 5. 1 Device structure for I-V and Radiation experiments.

5.1.2. Substrates cleaning procedures

After selecting the substrates and cutting the silicon wafers to the desired size all the substrates went through cleaning process before being placed into the vacuum chamber. The cleaning process is very important in the whole process as contaminated substrates would affect the vacuum efficiency and also will produce contaminated thin-films. To prevent cross contamination, all tools (i.e. beakers, tweezers, substrate glass covers, substrates fixing clamps, and nuts) were firstly cleaned. The substrates and tools cleaning procedures can be summarized as following:

- Rubbing under running di-ionized water and soap to eliminate any soft organic and/or inorganic contaminants on the surface.
- Ultrasonic bath for 30 minutes in di-ionized water to remove any traces from the soap cleaning step

- Ultrasonic bath for 30 minutes in acetone to eliminate any hard organic contaminants on the surface
- Ultrasonic bath for 30 minutes in isopropyl alcohol to eliminates any remaining traces from the acetone cleaning step
- Ultrasonic bath for 30 minutes in warm di-ionized water (approximately 40°C) to remove any remaining traces from the isopropyl alcohol.
- And finally drying in compressed air

After everything is cleaned and dried the process of mounting the substrates on the substrate holder begins. The substrates were fixed using stainless-steel clamps which exert a gentle force on the substrate surface when tightened with a screw from the other side as can be seen from the substrate holder picture in figure 4.8.

To prevent any interaction between the fixing clamp and the substrate at the elevated deposition temperature, very thin (approximately 0.5mm thickness) slices of silica glass were used at the point of contact between the clamp and the substrate. This glass cover also worked as a mask for the back contact layer in the selected samples for I-V measurements to provide a window to make the electrical connections. After the substrates are mounted, the load lock gate is then closed and the system operational procedures starts.

5.1.3. Vacuum system operational procedures

Vacuum system start up: the procedure start with turning on the mechanical pump while having the turbo pump off and the butterfly valve is in the totally open position and the isolating valve also opened and the system should be left until the ultimate vacuum level of the mechanical pump is approached ($5 \cdot 10^{-2}$ Torr). The system usually approaches that level within less than an hour, otherwise, the system should be checked for leakage. At this point, it is recommended to perform several cycles of flushing the system with argon gas, i.e close the isolating valve and flow argon gas into the system until the pressure reaches atmosphere, and then allow the mechanical pump to evacuate again by opening the isolating valve. This process ensures a cleaner vacuum environment and higher ultimate vacuum level. At this stage, the turbo pump is started. When the turbo pump start rotating, the rotating frequency starts to increase gradually from zero until it reaches its nominal frequency (1500Hz) within less than 10 minutes. If the turbo pump rotational frequency didn't saturate or saturated at a value less than 1500Hz, this a sign that the turbo pump needs maintenance or the system needs to be checked for leakage. At this point the system should be left until the ultimate vacuum level of the turbo pump is approached ($8 \cdot 10^{-6}$ Torr, in approximately 12hours)

Starting the substrate heater: after reaching the ultimate vacuum in the system the substrate heater is to be started by setting up the desired temperature and at the same time starting up the cooling chiller to protect the sealing O-ring from overheating. The substrate heater usually approaches the temperature set value within 2-3 hours. During the heating process, some perturbation in the vacuum level and turbo pump rotation frequency may be observed due to outgassing, but eventually the vacuum level will get back to its ultimate value.

Introducing the hydrocarbon mixture (gas precursor): after approaching the ultimate vacuum again and with stable set temperature, all the valves along the junction between the vacuum system and the valve at the mixing point (see figure 4.5) should be opened to extend the vacuum to this point. At this stage, the mixing ratios of each gas should be adjusted with the mass flow controllers allowing the gas mixture to flow into the chamber. Consequently, the opening percentage of the butterfly valve and/or the mass flow controllers set values can be adjusted to obtain the desired deposition pressure and mixing ratios. At this point the power supply should be adjusted to the desired operating mode (constant current, constant volt or constant power) and the desired values. In the current study, all the samples were prepared using the constant current mode at the current value 200mA.

Shut down procedures: after the desired deposition time is passed the shutdown procedures starts. First the power supply and the substrate heater are switched off. Then the whole gas feeding system should be closed and the system should be left to be cooled down to room temperature under the ultimate vacuum. Then, the isolating valve between the turbo pump and the vacuum chamber is closed. After that, the turbo pump is turned off and left for some time until its rotational frequency approach zero while keeping the mechanical pump running until this point. Then the mechanical pump is also shut down and the system can be vented until atmospheric pressure is approached.

5.1.4. Samples preparation conditions

There are too many parameters that can affect the growth of the thin-film for example the substrate temperature, the plasma condition (the current and the voltage), the operating pressure and the gases mixing ratios. In this study, all the samples were prepared at the same substrate temperature (200°C), deposition time (5 hours) and constant plasma current (200mA) whereas the parameters that have been varied are the operating pressure and the gases mixing ratios. Table 5.1 summarizes the preparation condition for the prepared samples in this study.

Table 5. 1 Samples preparation Conditions

Parameter/sample ID		S1	S2	S3	S4	S5	S6	S7
Operating Pressure(mTorr)		80	80	80	80	500	160	160
Gases mixture		100%CH ₄	75%CH ₄	50%CH ₄	25%CH ₄	100%CH ₄	100%CH ₄	75%CH ₄
	H ₂ sccm	0	2.8	4	5.1	0	0	2
	CH ₄ sccm	7.8	5.1	4	2.9	13.5	8	6
Butterfly valve opening percentage		50%	50%	50%	50%	30%	30%	30%
Plasma condition								
Current mA	Volt V							

5.2. Samples Characterization

Four characterization techniques were used to study the samples. UV-Vis spectroscopy to measure the band gap and the positions of defects levels inside the band gap, FTIR spectroscopy to give an idea of the bonding structure, Raman spectroscopy to analyze the microstructure and finally current voltage characteristics and radiation testing. In this section, a brief introduction about each characterization technique and its application to characterize carbon based materials will be presented with a description of the characterization experiment.

5.2.1. Fourier transform infrared spectroscopy (FTIR)

FTIR is a characterization technique based on the interaction of Infra-red light with the specimen to determine the bonding types that exist in the sample. In an FTIR spectrum, the absorption band is defined by the wavenumber at which the absorption occurs (which corresponds to the existence of specific types of bond) and the intensity of the band (which corresponds to the amount of this bond in the sample). So, in general, the FTIR spectrum is a graphical representation between transmission percentage (T%) vs. IR Frequency in terms of wave-number (cm⁻¹). Like in Raman spectroscopy, the absorption process depends on molecular vibrations

but it provides less information than the Raman as the absorption in the FTIR depends on first order selection rule (change in the dipole moment) of the molecule whereas the Raman depends on second order selection rule (rate of change in dipole moment). The FTIR absorption spectrum of carbon materials consists of C-H stretching modes at 2800–3300 cm^{-1} and C-C modes and C-H bending modes below 2000 cm^{-1} .^{33–35}

A PerkinElmer FTIR spectrometer, spectrum 100 series, was used to perform the FTIR measurements in this study. The measurements were recorded in the transmission mode where the sample compartment contains two holders. At one of the holders a bare silicon substrate was mounted to be used as background spectrum whereas a silicon substrate coated with the carbon film to be characterized is mounted on the other holder. The reading were recorded in the range from 400 to 4000 cm^{-1} , with a 16 cm^{-1} resolution and 50 accumulations. After the data was recorded it was then plotted and de-convoluted using origin pro software.

5.2.2. Raman spectroscopy

5.2.2.1. The generation of the Raman signal

Figure 5.2 explain the light interaction with matter during Raman scattering. In a typical Raman experiment, the sample is shined with a laser beam in the Visible or Ultraviolet range. When a laser photon is hitting the surface of the sample with energy $h\nu_0$ three scenarios might happen:

- Elastic scattering interaction (Raleigh scattering): no energy transfer and no information about the molecular structure is carried out by the scattered photon
- Inelastic scattering (anti-stokes): the scattered photon is shifted to higher frequency. This interaction requires the molecule to already be in an excited state at room temp, consequently this interaction has low probability and negligible contribution to the Raman signal

- Inelastic scattering (stokes): the scattered photon is shifted to lower frequency this interaction happens when the molecule is in ground state at room temp, so it has a high probability and forms the Raman signal.¹⁶

5.2.2.2. Raman spectrum of amorphous/diamond like carbon thin-films

Based on the carbon materials ternary phase diagram and the ternary three stage model introduced by Ferrari et al., discussed earlier in sections 1.2 and 1.3. A quick notes on the interpretation of Raman spectrum of carbon based thin films provided in this section.

For a carbon thin-film to be categorized as amorphous or diamond like carbon the Raman data should be de-convoluted and it's necessary to obtain a good data fitting into only two peaks commonly known as the G peak (for graphite) and the D peak (for disordered graphite). The G Peak is due to any SP² pairs, both chains and rings, and are usually located around 1580 cm⁻¹. The D peak is due to the breathing mode of SP² in rings. So basically no rings no D peak. The D peak is usually located around 1360cm⁻¹. Depending on the position of the G peak and the relative intensities of the D&G peaks an amorphization trajectory was developed by Ferrari et al. (presented in figure 5.3) which can be used as a guide to categorize the spectrum into one of the regions in the ternary phase diagram and anticipate its corresponding properties. general observations from figure 5.3 are pointed out: ^{15, 36}

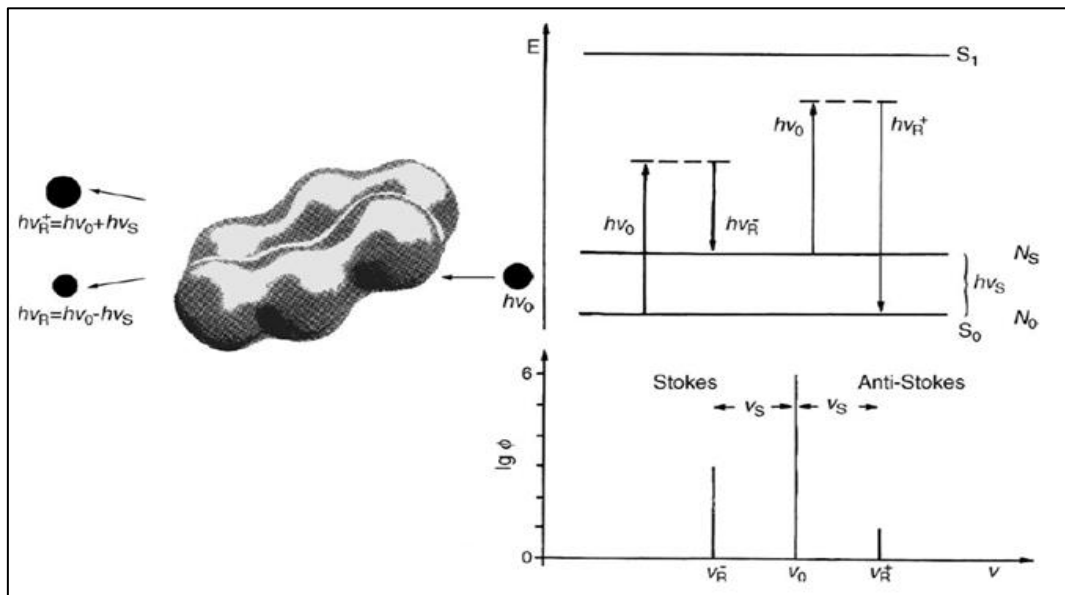


Figure 5. 2 Schematic diagram explaining the mechanism of Raman scattering, molecular vibrational transitions and the stokes/anti-stokes frequencies¹³.

- Starting from a perfect graphite, 100% ordered SP^2 , the Raman spectrum will consist of a single narrow line at 1580 cm^{-1} . (The G Peak)
- Moving in the direction of disorder bond structure but still SP^2 is the dominant content, nano-crystalline graphite, the Raman spectrum will exhibit a broadening in the G peak, a shift toward 1600 cm^{-1} and the appearance of the D peak around 1350 cm^{-1} , representing the breathing mode of the disordered graphite (stage 1)
- Moving into more disorder in the SP^2 content, SP^3 start to grow (0 to 20%), indicative of a-C region, stage 2. The Raman spectrum will exhibit a downshift in the G peak position from 1600 to 1520 cm^{-1} and a decrease in the I_D/I_G ratio.
- By increasing the SP^3 content up 85-90%, we reach the ta-C region, stage 3. The Raman spectrum will exhibit an up shift in the G peak position from 1520 to 1570 cm^{-1} and a significant decrease in the I_D/I_G ratio.

One important parameter when characterizing Carbon films with the Raman technique is the excitation laser wavelength. When using visible light, the spectrum is dominated by SP^2 and has very low

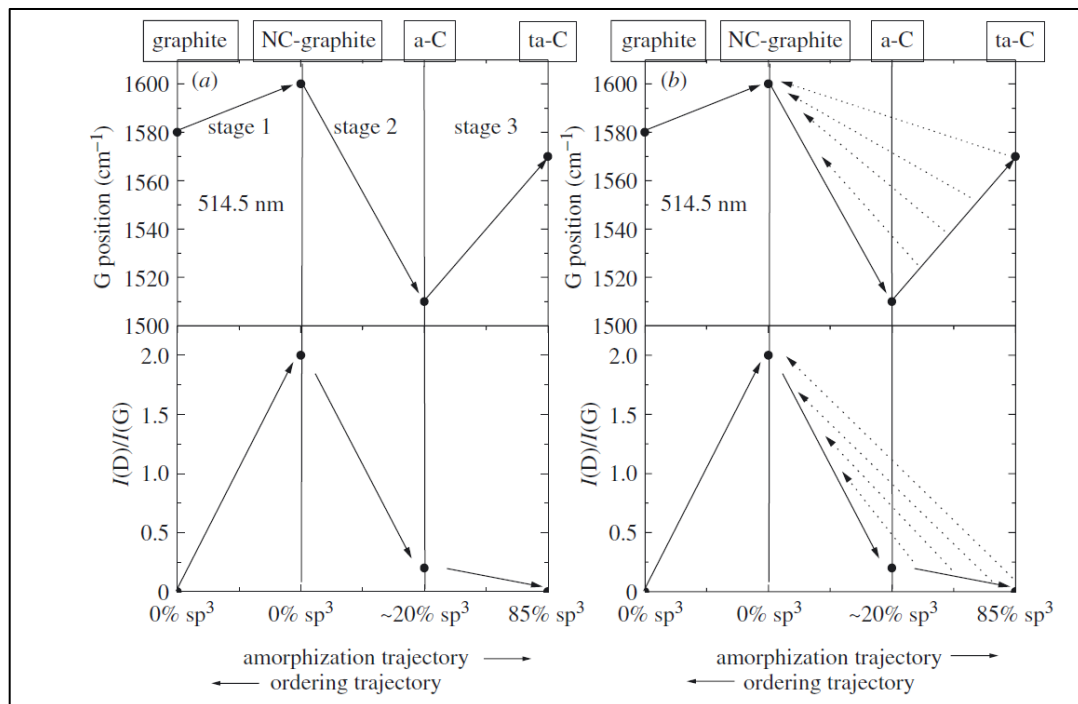


Figure 5. 3 Three-stage model of the variation of the Raman G position and the D-to-G intensity ratio, $I(D)/I(G)$, with increasing disorder . The dotted left-pointing arrows in (b) mark the non-uniqueness region in the ordering trajectory³³.

sensitivity for SP³ stretches, due to resonance effects. As mentioned earlier, the G&D peaks are mainly arising from SP² stretches. When the SP³ is significantly higher than the SP² and/or exhibits a degree of crystallinity, the spectrum will not provide a good fitting with only the G&D peaks and additional peaks will be needed to obtain a better fitting. These new peaks to be added are usually arising from diamond related vibrations and/or grain boundaries and a new category of carbon which is nano-crystalline diamond. ^{16,36,37}

5.2.2.3. Raman spectrum of nano-diamond materials

In addition to the D&G peaks, nano-crystalline and post heat treated diamond usually exhibits three additional peaks located around 1100, 1250 and 1470 cm⁻¹. The peak around 1100 cm⁻¹ has been the topic of a very controversial discussion in the literature. Some of the reports have assigned it to trans-polyacetelen on the grain boundaries while other reports attributed it to surface phonon in nano particle size diamond. More recently, Ferrari et. al ³⁶ presented a convincing argument that this peak is more probable to be arising from trans-polyacetelen at the grain boundaries which must be accompanied with another peak at 1470 cm⁻¹. On the other hand, Praver et. al³⁸ measured the Raman spectrum of bulk single crystal diamond ion implanted with 3.5Mev He ions and showed a broad peak around 1250 and a shoulder around 1120 cm⁻¹. They concluded that this represents the DOS (density of states) of amorphous diamond when compared to a crystalline one. In the current study, as will be seen in the next chapter, when the three peaks were observed in some samples, the 1100 and the 1470 peaks were attributed to be arising from trans-polyacetelen at the grain boundaries whereas the 1250 peak was assigned to vibrational density of state (VDOS). In other samples the peak around the 1470 didn't appear, in this case the 1100 and the 1250 peaks were identified as diamond signature. ^{36,39,40}

Finally, the Raman spectrum of single crystal diamond would exhibit a single narrow line around 1332 cm⁻¹ which represents the first order Raman and a broad band around 2470 to 2670 cm⁻¹ which represents the second order Raman. ³⁸

5.2.3. UV-Visible and measuring the band gap

For some selected samples, namely samples S5, S6 and S7, UV-Visible spectroscopy and Tauc equation were used to measure the optical band gap and getting information about the distribution of defect levels inside the band gap. Tauc equation is a commonly fitting method used to determine optical transition states either direct/indirect and/or forbidden/allowed. Based on the absorption data in the UV-Visible region, Tauc equation presented in equation 1 is plotted. ^{41,42}

$$\alpha h\nu = a (h\nu - E_g)^m \quad \text{eq (1)}$$

Where $h\nu$ is the energy of the incident photon, α is the thin-film absorption coefficient, E_g is the energy gap of the transition, a is arbitrary constant and m is a fitting parameter which has a specific value for each type of transition i.e. $m=0.5$ for direct allowed transition (direct band gap), $m= 1.5$ for direct forbidden (direct defect level), $m=2$ for indirect allowed transition (indirect band gap) and $m=3$ for indirect forbidden transition.³⁷⁻³⁹

Absorption data were collected in the wavelength range 320 nm to 2500nm wavelength, then $(\alpha h\nu)^{1/m}$ vs. $h\nu$ were plotted for $m =0.5$ and $m=2$, so that the intersection of the linear portion of the plot and the X-axis can be used to get information about the band gap and the defect levels inside the band gap respectively.

5.2.4. I-V characteristic and radiation measurement

The basic principle of the radiation experiments are based on monitoring a change in the sample conductivity when exposed to the radiation source. In other words, the I-V characteristic curve is recorded in the dark (in the absence of the radiation) by sourcing voltage and measuring the corresponding current. Then the radiation source is introduced and the I-V characteristic curve is recorded again with expectation to see a shift in the I-V curve. The second step in the testing is to find a physical meaning in light of the information obtained from the other characterization techniques for that change in conductivity.

The I-V characteristic was recorded using a Keysight B2901A Precision Source/Measure Unit, connected via BNC cables (to isolate any electrical noise and to prevent leakage current) to an isolating box which ensures that the sample is not exposed to any light during the measurement and will help unifying the

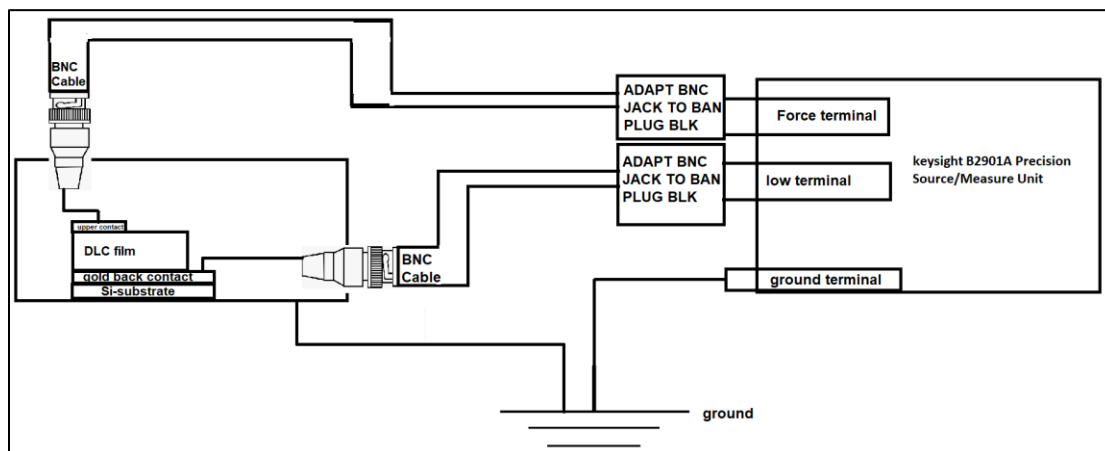


Figure 5. 4 Schematic diagram for I-V characteristic setup.

ground in the circuit as can be seen in figure 5.4. Am-241 5.5MeV α particle source was used as a radiation source.

6. Results and Discussion

6.1. FTIR Results

6.1.1. S1 results and discussions

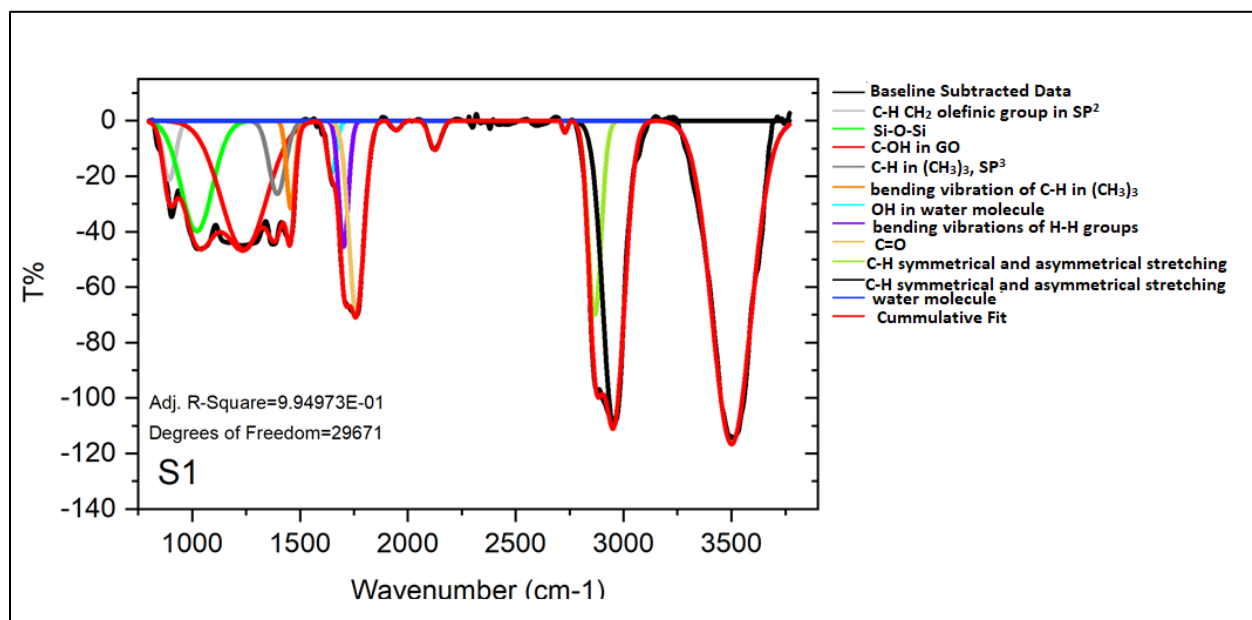


Figure 6. 1 De-convoluted FTIR spectrum of S1.

Table 6. 1 S1 fitting results

Peak Index	FWHM	Center Grvty	Area IntgP
C-H vibrations of CH ₂ olefinic group in SP ²	67.54	893.67	-1.88
Si-O-Si	170.96	1021.3	-8.92
C-OH in GO	248.73	1239.18	-15.13
C-H in (CH ₃) ₃ in SP ³	90.17	1394.17	-3.12
bending vibration of C-H in (CH ₃) in SP ³	45.66	1457.02	-1.89
OH in water molecule	50.03	1646.06	-1.23
bending vibrations of H-H groups	52.24	1701.81	-3.11
C=O	82.29	1761.33	-7.49
C-H symmetrical and asymmetrical stretching	71.23	2865.76	-6.54
C-H symmetrical and asymmetrical stretching	117.00	2953.35	-16.86
Water Molecule	213.50	3500.86	-32.59

Figure 6.1 shows the de-convolution results of the FTIR spectrum of S1 and table 5.1 summarizes its fitting results. The first band can be observed is the band at 894 cm^{-1} , which can be attributed to C-H vibrations of CH_2 olefinic group with SP^2 , similar to the peak previously reported by Varghri et al. at 914 cm^{-1} .⁴⁴ The peak around 1021 can be attributed to stretching vibration of Si-O-Si reported previously by Dasilva et al.⁴⁵ in graphene oxide (GO) films at around 1030 cm^{-1} which may be arising from the substrate.⁴⁵ The peak around 1239 cm^{-1} can be attributed to stretching vibration of C-OH in GO reported previously by Chang et al. and Stankovich et al. at around 1230 cm^{-1} .^{46,47} The peak around 1394 cm^{-1} can be attributed to bending vibration of C-H in $(\text{CH}_3)_3$ with SP^3 bonding reported previously by Chu et al. and Vaghry et. al to lie in the range $1370\text{--}1400\text{ cm}^{-1}$.^{16,44} . Note that these peaks may also be arising from bending vibrations of H-H groups reported previously to lie in the range $1700\text{--}1300\text{ cm}^{-1}$ by Chu et al., Vaghry et al., Alba et al and Bonelli et al.^{39,44,48,49} The peak around 1457 cm^{-1} can be attributed to the bending vibration of C-H in $(\text{CH}_3)_3$ with SP^3 bonding reported previously by Chu et al. to lie between $1460\text{--}1480\text{ cm}^{-1}$ in hydrogenated DLC films.¹³

The peak around 1646 cm^{-1} can be attributed to bending vibration of OH in water molecule which is usually accompanied by a strong absorption band around 3600 cm^{-1} , commonly reported in nano-crystalline diamond thin films.^{50,51} This peak maybe also arising from stretching vibration of C=C in reduced graphene oxide aromatic ring as reported previously by Aldosari, et al., Ban et al., Chhabra et al. and Shahriary et al.^{52–55}

The peak around 1701 cm^{-1} can be attributed to bending vibrations of H-H groups reported previously to lie in the range $1700\text{--}1300\text{ cm}^{-1}$ by Chu et al., Vaghry et al., Alba et al and Bonelli et al.^{39,44,48,49}

The peak around 1761 cm^{-1} can be attributed to carbonyl group C=O reported previously by Chabra et al. to be located between $1760\text{--}17665\text{ cm}^{-1}$.⁵⁵ Also Tu et al. performed a size dependent analysis of the C=O stretching in nano-crystalline diamond films, with thickness ranging from 5 to 500nm, to lie between $1680\text{--}1820\text{ cm}^{-1}$.⁵⁶

Lastly, the two peaks around 2865 and 2953 cm^{-1} can be attributed to C-H symmetrical and asymmetrical stretching vibration from CH_2 and CH_3 groups where hydrogen is binding from a SP^3 hybridized carbon which are commonly reported to lie in the range $2850\text{--}3000\text{ cm}^{-1}$.^{33,51}

6.1.2.S2 results and discussion

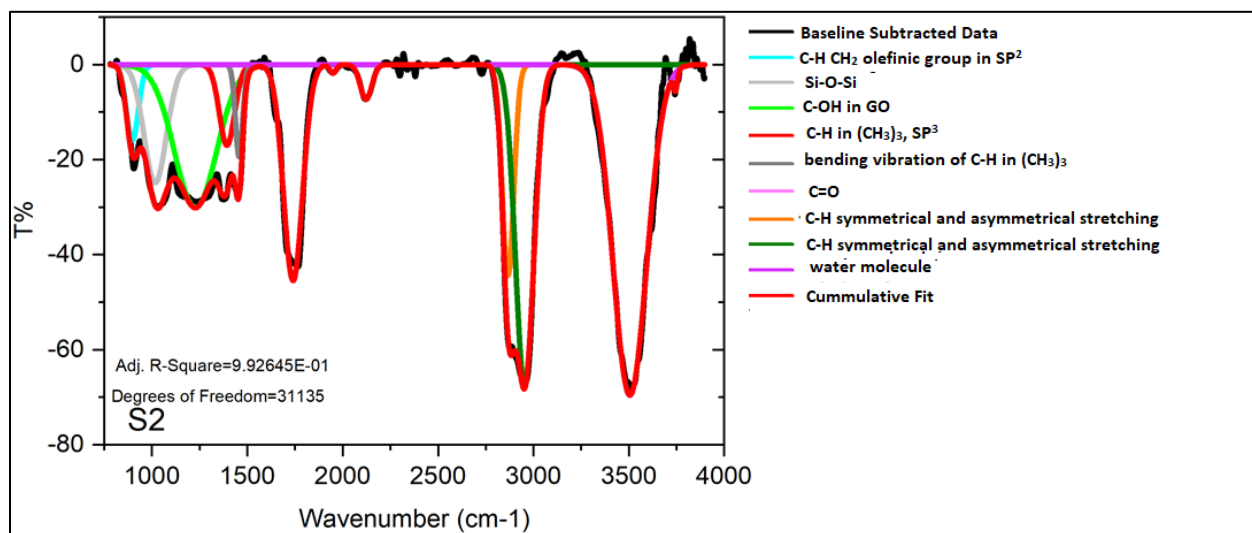


Figure 6. 2 De-convoluted FTIR spectrum of S2.

Figure 6.2 shows the de-convolution results of the FTIR spectrum of sample S2 and table 6.2 summarizes its fitting results. All the peaks featured in Sample 2 are presented also in sample 1, and can take the same attributions as explained in the previous section, except for the disappearance of the following two peaks:

Table 6. 2 S2 fitting results

Peak Index	FWHM	Center Grvty	Area IntgP
C-H vibrations of CH ₂ olefinic group in SP ²	73.64	896.89	-2.54
Si-O-Si	137.10	1016.95	-7.37
C-OH in GO	260.28	1227.95	-16.96
C-H in (CH ₃) ₃ in SP ³	94.05	1393	-3.46
bending vibration of C-H in (CH ₃) in SP ³	45.04	1456.52	-1.88
C=O	117.54	1739.43	-11.57
C-H symmetrical and asymmetrical stretching	71.24	2866.41	-6.84
C-H symmetrical and asymmetrical stretching	113.78	2953.79	-16.63
Water Molecule	207.39	3505.36	-31.25

- The peak around 1646cm⁻¹ which was attributed to OH
- The peak around 1701cm⁻¹ which was attributed to H-H group

The disappearance of the two peaks can be explained by the increase of the hydrogen content in the gases mixture which might add an H to the OH group thus making the band at 3600 cm^{-1} (water molecule) more pronounced and also will break the H-H group into two H_2 .

6.1.3.S3 results and discussion

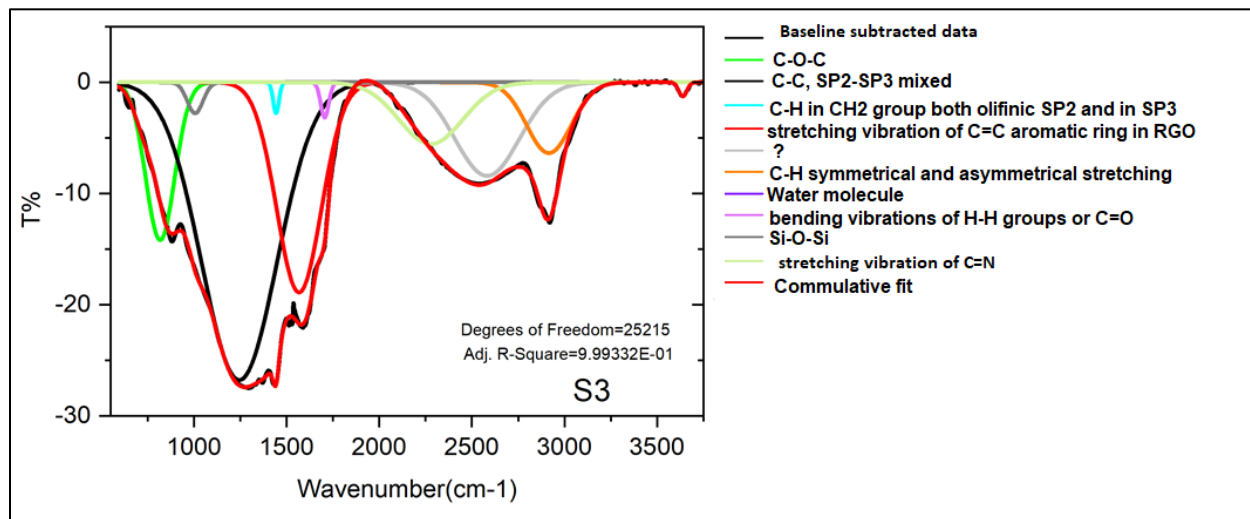


Figure 6. 3 De-convoluted FTIR spectrum of S3.

Figure 6.3 shows the de-convolution results of the FTIR spectrum of S3 and table 6.3 shows its data fitting results. S3 showed some common peaks with the previous two samples as well as the appearance of new peaks. The first peak around 817 cm^{-1} can be attributed to bending vibration of C-O-C in GO films as reported previously by Dou et al. and Obreja et al. to be located around 850 cm^{-1} , which is a new band that didn't appear in the previous two samples^{54, 55}. The band around 1006 cm^{-1} can be attributed to Si-O-Si arising from the substrate similar to the S1 and S2. The peak around 1244 cm^{-1} can be attributed to C-C stretching vibrational mode arising from SP^2 - SP^3 mixed sites reported previously by Bonelli et al. and Chu et al. to be located at around $1300\text{--}1245\text{ cm}^{-1}$ ^{45, 47}. This peak didn't appear in samples S1 and S2 and its appearance in S3 can be explained as the mixed SP^2 - SP^3 sites started to appear in S3 when the crystallite size of the SP^3 content started to be small enough to be intermixed with the SP^2 content. This will also be noticed later with the Raman analysis as this mixing sites will result in the coverage of the SP^2 spectrum over the spectrum of the SP^3 due to resonance effects.

Table 6. 3 S3 fitting results

Peak Index	FWHM	Center Grvty	Area IntgP
C-O-C	184.13	817.70	-9.84
C-C, SP ² -SP ³ mixed sites	478.39	1244.56	-48.32
C-H in CH ² group both olefinic SP ² and in SP ³	36.64	1443.20	-0.38
stretching vibration of C=C aromatic ring in RGO	283.38	1567.30	-20.21
?	408.32	2582.90	-12.97
C-H symmetrical and asymmetrical stretching	282.83	2916.07	-6.80
Water molecule	51.8	3639.10	-0.25
bending vibrations of H-H groups or C=O	51.26	1705.84	-0.61
Si-O-Si	99.94	1006.01	-1.05
stretching vibration of C=N	405.20	2278.00	-8.48

The peak around 1443cm⁻¹ can be attributed to bending vibration of C-H in CH₂ group with both olefinic SP² and SP³ bonding, as reported by Vaghri et al. to be located around 1450cm⁻¹⁴⁴. It can be noticed that this peak is a little shifted with respect to the one observed in S1 and S2. This could be attributed to the assignment in S1 and S2 from (C-H in CH₃) and exclusive SP³ bonding, whereas the S3 peak originates from CH₂ groups, which can be correlated with the increase of the hydrogen content in S3 in the gases mixture. The peak around 1567cm⁻¹ is another new peak that is detected in S3 and not in S1 and S2. It can be attributed to stretching vibration of C=C aromatic ring in reduced graphene oxide (RGO) as previously reported by Obreja et al. and Stanlovich et al to be located at around 1575-1560cm⁻¹^{47,57}. The peak around 1705 cm⁻¹ can be attributed to H-H vibration similar to its assignment in S1 and/or vibrational modes from the C=O carbonyl group as reported by Tu et al. to lie in the range 1820-1680 cm⁻¹ in nano-crystalline diamond thin-films. It also can be noticed that the peak around 1646 which was detected in S1, and attributed to OH, not observed in either S2 or S3. The next peak in the spectrum is located at 2278cm⁻¹ can be attributed to the stretching vibration of C=N reported previously by Chabra et al. to be located at around 2260-2210cm⁻¹⁵⁵.

The peak around 2916cm⁻¹ can be attributed to C-H symmetrical and asymmetrical stretching vibration from CH₂ and CH₃ groups where hydrogen is binding from a SP³ hybridized carbon, and which are

commonly reported to lie in the range 2850 – 3000 cm^{-1} ^{33,51} Lastly the peak around 3839 cm^{-1} can be attributed to water molecule vibration similar to S1 and S2.

6.1.4.S5 results and discussion

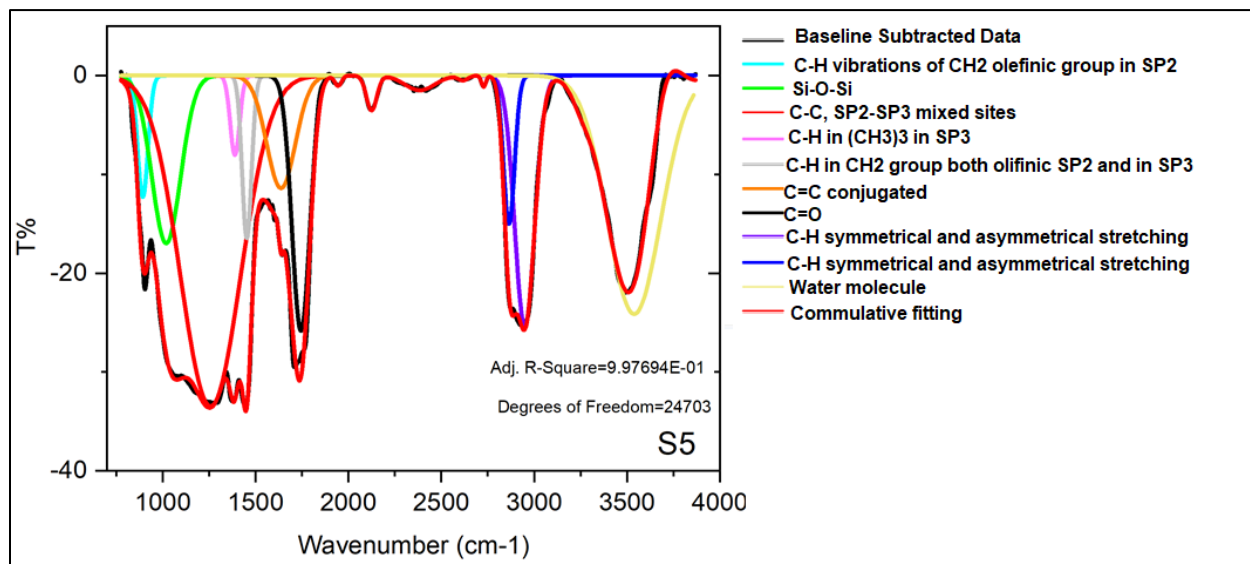


Figure 6. 4 S5 de-convoluted FTIR spectrum.

Table 6. 4 S5 fitting results

Peak Index	FWHM	Center Grvty	Area IntgP
C-H vibrations of CH ₂ olefinic group in SP ²	65.55	892.33	-2.37
Si-O-Si	182.03	1018.39	-9.10
C-C, SP ² -SP ³ mixed sites	381.68	1257.03	-37.60
C-H in (CH ₃) ₃ in SP ³	59.23	1388.04	-1.40
C-H in CH ₂ group both olefinic SP ² and in SP ³	59.29	1452.46	-2.87
C=C conjugated	181.86	1636.37	-6.11
C=O	112.83	1743.62	-8.6
C-H symmetrical and asymmetrical stretching	126.19	2948.8	-9.46
C-H symmetrical and asymmetrical stretching	70.28	2864.3	-3.11
Water molecule	336.95	3538.07	-23.73

Figure 6.4 shows the de-convolution results of the FTIR spectrum of S5 and table 5.4 summarizes its fitting results. The first peak around 892 cm^{-1} can be attributed to C-H vibration of CH₂ olefinic group in SP² configuration which was also detected in samples 1 and 2 but not in sample 3. The peak around 1018 cm^{-1} can be attributed to Si-O-Si vibration arising from the substrate as explained earlier. The peak around 1257 cm^{-1}

can be attributed to C-C vibration from SP²-SP³ mixed sites similar to S3. The peak around 1388 cm⁻¹ can be attributed to C-H vibration in (CH₃)₃ in SP³ configuration. The peak around 1452 cm⁻¹ can be attributed to C-H vibration in CH₂ group with both olefinic SP² and SP³ bonding.

The peak around 1636 cm⁻¹ arises from C=C stretching vibration in conjugated carbon bonds reported previously by Chhabra et al. to be located around 1640-1620cm⁻¹ ⁵⁵ . The peak around 1743 cm⁻¹ can be attributed to C=O as reported by Tu et al. in nano-crystalline diamond films. The two peaks around 2948cm⁻¹ and 2864 cm⁻¹ can be attributed to C-H symmetrical and asymmetrical stretching and finally the peak around 3538cm⁻¹ comes from water molecule vibrations as explained earlier. Two main differences can be observed between the spectrum of sample 5 and the previous samples which can be explained with the huge jump in the deposition pressure of S5 with respect to samples S1,S 2 and S3:

- The disappearance of the graphene content
- The relative increase in the SP² content over SP³ content

6.1.5.S6 results and discussion

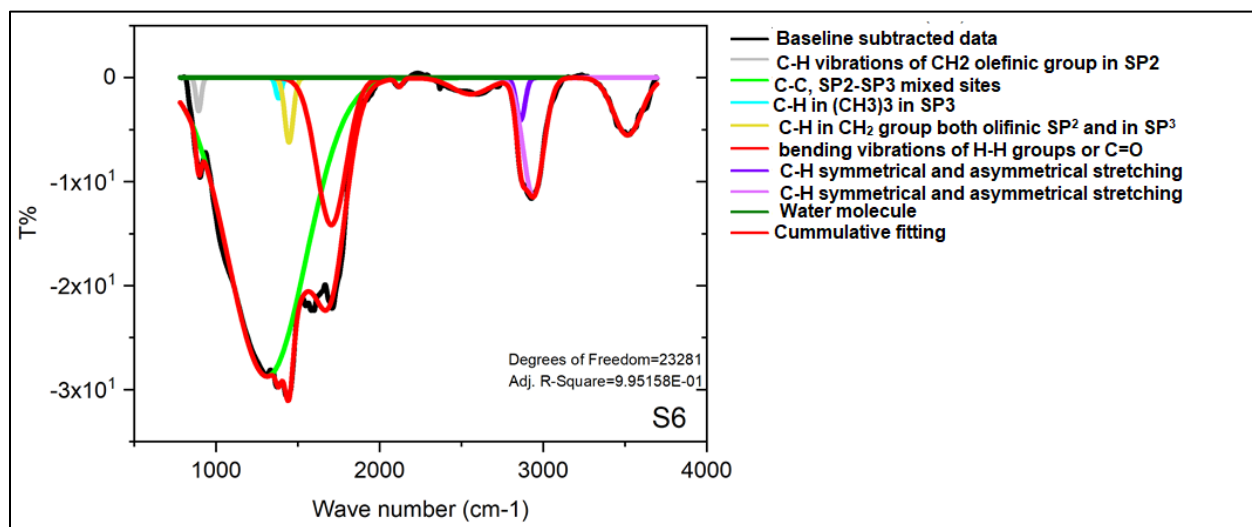


Figure 6. 5 S6 de-convoluted FTIR spectrum.

Table 6. 5 S6 fitting results

Peak Index	FWHM	Center Grvty	Area IntgP
C-H vibrations of CH ₂ olefinic group in SP ²	36.63	893.27	-0.51
C-C, SP ² -SP ³ mixed sites	560.23	1311.47	-69.16
C-H in (CH ₃) ₃ in SP ³	39.70	1382.21	-0.34
C-H in CH ₂ group both olefinic SP ² and in SP ³	59.98	1445.68	-1.62
bending vibrations of H-H groups or C=O	212.83	1704.85	-13.13

C-H symmetrical and asymmetrical stretching	63.25	2861.57	-1.12
C-H symmetrical and asymmetrical stretching	147.00	2939.21	-7.31
Water molecule	201.38	3514.86	-4.76

Figure 6.5 shows the de-convolution results of the FTIR spectrum of S6 and table 6.5 summarizes its fitting results. The peak around 893 cm^{-1} can be attributed to C-H vibration of CH_2 olefinic group in SP^2 configuration. The peak around 1311 cm^{-1} can be attributed to C-C vibration from $\text{SP}^2\text{-SP}^3$ mixed sites similar to S3 and S5. The peak around 1382 cm^{-1} can be attributed to C-H vibration in $(\text{CH}_3)_3$ in SP^3 configuration. The peak around 1452 cm^{-1} can be attributed to C-H vibration in CH_2 group both olefinic SP^2 and in SP^3 . the peak around 1704 cm^{-1} can be attributed to H-H vibration similar to its assignment in S1 and also can be arising from C=O carbonyl group as reported by Tu et al. to lie in the range $1820\text{-}1680\text{ cm}^{-1}$ in nano-crystalline diamond thin-films. The two peaks around 2939 cm^{-1} and 2861 cm^{-1} can be attributed to C-H symmetrical and asymmetrical stretching and finally the peak around 3514 cm^{-1} is assigned to water molecule vibrations as explained earlier.

6.1.6.S7 results and discussion

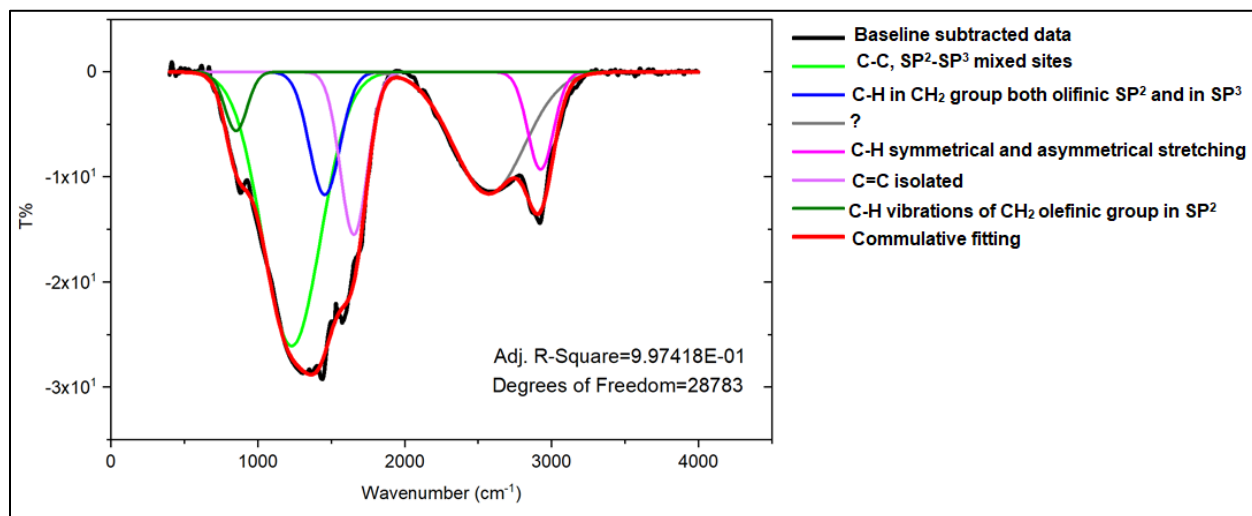


Figure 6. 6 S7 de-convoluted FTIR spectrum.

Table 6. 6 S7 fitting results

Peak Index	FWHM	Center Grvty	Area IntgP
C-H vibrations of CH ₂ olefinic group in SP ²	187.63	851.12	-3.95
C-H in CH ₂ group both olefinic SP ² and in SP ³	464.88	1230.08	-43.48
C-H in (CH ₃) ₃ in SP ³	245.79	1455.30	-10.30
?	569.85	2572.94	-23.69
C-H symmetrical and asymmetrical stretching	206.16	2925.60	-6.85
C=C isolated	217.38	1653.75	-12.06

Figure 6.6 shows the de-convolution results of the FTIR spectrum of S7 and table 6.6 summarizes its fitting results. The peak around 851 cm⁻¹ can be attributed to C-H vibration of CH₂ both the olefinic SP² and in SP³. The peak around 1455 cm⁻¹ can be attributed to C-H vibration in (CH₃)₃ in SP³ configuration. The peak around 2925cm⁻¹ can be attributed to C-H symmetrical and asymmetrical stretching. An important fact to be mentioned about S7 is that, it is the only sample which didn't show the water molecule absorption band, which can be interpreted as a sign of the absence of any range of crystallinity even in the nano-crystalline range. Also, similarly to S5 and S6, S7 didn't show any graphene related bands.

6.2. Raman Spectroscopy Results

6.2.1. S1 results and discussion

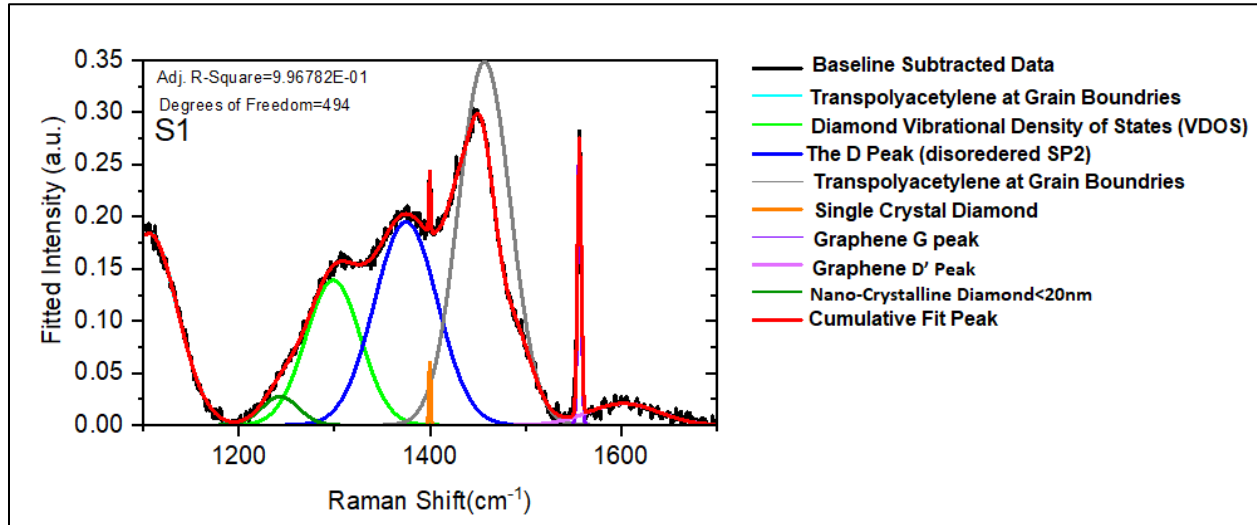


Figure 6. 7 S1 de-convoluted Raman spectrum in the range 1100-1700 cm^{-1} excited by 532nm laser wavelength at 50% laser power and 10S exposure time.

Table 6. 7 S1 fitting results

Peak Index	Fitting Peak type	FWHM	Center Grvty	Area IntgP
Trans-polyacetylene at grain boundaries	Gaussian	69.22	1106.25	13.10
Diamond vibrational density of states (VDOS)	Gaussian	67.76	1298.77	17.67
The D peak (disordered SP^2)	Gaussian	77.83	1374.87	28.47
Trans-polyacetylene at grain boundaries	Gaussian	64.11	1457.06	41.69
Single crystal diamond	Gaussian	2.07	1399.83	0.23
Graphene G peak	Gaussian	4.59	1556.37	2.29
Graphene D' Peak	Gaussian	86.82	1602.51	3.38
Nano-crystalline diamond <20nm	Gaussian	45.37	1243.33	2.34

Figure 6.7 shows the de-convolution results of S1 Raman spectrum in the range 1100-1700 cm^{-1} excited by 532nm laser and table 6.7 shows its fitting results. Firstly, the grain boundaries related peaks can be observed from the graph namely the two peaks around 1106 and 1457 cm^{-1} which can be attributed to trans-polyacetylene as explained earlier in section 4.2.2.3.

Secondly, the diamond related peaks, around 1298.77 and 1243 cm^{-1} can be attributed to vibrational density of states (VDOS) in diamond as previously reported by Beeman et al. who calculated the Raman spectrum of an amorphous, fully SP^3 random network and predicted a main Raman peak around 1265 cm^{-1} ⁵⁸. Also, Praver et al. reported Raman spectrum of ion implanted diamond that exhibited a broad peak around 1250 cm^{-1} together with a shoulder at 1120 cm^{-1} and they concluded that the measured spectrum can represent the DOS in diamond. It has also been reported by Vlasov, I.I. et al. that the peak around 1250 cm^{-1} can be attributed to defects or crystallite size less than 20nm in diamond. Lastly Roy et al. and Ferrari et al. reported that the phonon density of states becomes more pronounced when surface effects becomes significant such as nano-crystalline diamond, heat treated and/or ion implanted, which shows peaks in the range 1240-1280 cm^{-1} ^{59,60}. It's worth mentioning that this results is consistent with the fact that the samples took a long time (approximately 3 hours) to cool down from the deposition temperature (200°C) to room temperature. The peak around 1399 cm^{-1} can be attributed to the first order line of single crystal diamond. The upshift in the diamond related peaks can be explained by the small thickness of the film which will induce an internal strain or by heating effect due to high laser power.

Graphene related peaks, typically found in graphene based materials, can be observed in a Raman spectrum with the G peak at around 1580 cm^{-1} corresponding to primary in-plane vibrational mode; the 2D peak at around 2690 cm^{-1} corresponding to a second order overtone of a different in-plane vibration mode and the D peak at around 1350 cm^{-1} . As the amount of disorder in graphene increases, the Raman intensity increases for the three separate disorder peaks: D (1350 cm^{-1}), which scatters from K to K' (intervalley); D' (1620 cm^{-1}), which scatters from K to K (intravalley); and D+G (2940 cm^{-1}). ⁶¹⁻⁶³

The peak around 1556 cm^{-1} represents Graphene G peak while the peak 1602 cm^{-1} is the graphene D' peak. The graphene 2D peak can also be seen from figure 6.8. The second order band of the diamond and the

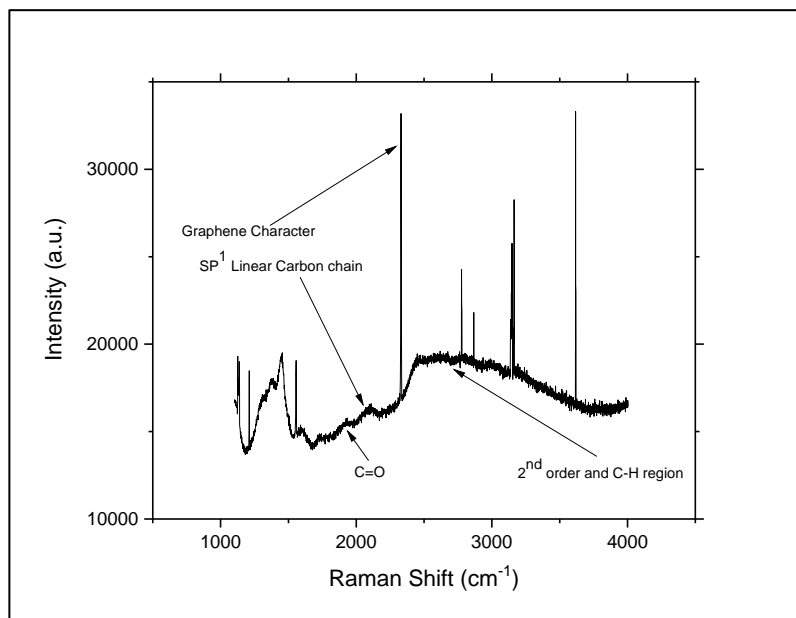


Figure 6. 8 S1 wide range raw data.

C-H related vibration indicating hydrogenation of the film are also shown in the figure.

6.2.2. S2 results and discussion

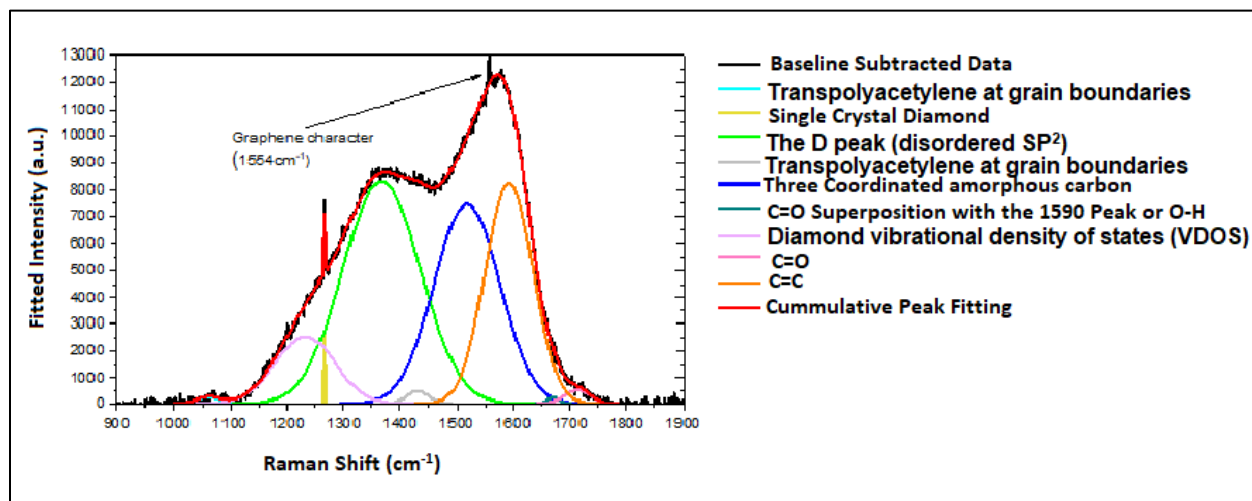


Figure 6. 9 S2 de-convoluted Raman spectrum in the range $900\text{-}1900\text{ cm}^{-1}$ excited by 532 nm laser wavelength at 50% laser power and 10S exposure time.

Table 6. 8 S2 fitting results

Peak Index	Fitting Peak type	FWHM	Center Grvty	Area IntgP
Trans-polyacetylene at grain boundaries	Gaussian	49.54	1061.18	0.35
Single crystal diamond	Gaussian	2.97	1265.12	0.21
The D peak (disordered SP ²)	Gaussian	161.46	1367.21	37.42
Trans-polyacetylene at grain boundaries	Gaussian	46.34	1430.87	0.65
Three coordinated amorphous carbon	Gaussian	136.53	1518.10	28.47
C=O superposition with the 1590 peak or O-H vibration	Gaussian	25.69	1670.79	0.18
Diamond vibrational density of states (VDOS)	Gaussian	126.18	1232.08	8.92
C=O	Gaussian	54.88	1712.59	0.82
C=C	Gaussian	99.78	1592.39	22.93

Figure 6.9 shows the de-convolution results of S2 Raman spectrum in the range 900-1900cm⁻¹ excited by 532nm laser and table 6.8 shows the fitting results. Firstly, the grain boundaries related peaks can be seen from the graph namely the peak around 1061 and 1430 cm⁻¹ which can be attributed to trans-polyacetylene as explained earlier in section 5.2.2.3.

Secondly, looking at diamond related peaks, the one around 1232 cm⁻¹ represents vibrational density of states (VDOS) in diamond and the peak around 1265 cm⁻¹ can be attributed to the single crystal diamond first order line.

Looking at Graphene and SP² related peaks, the peak around 1367 cm⁻¹ represents the D peak. The peak around 1518 cm⁻¹ can be attributed to three coordinated amorphous carbon as predicted by Beeman et al. to be located around 1528 cm⁻¹⁵⁸. The peak around 1670 cm⁻¹ can be arising from a superposition of the SP² carbon band at 1592 cm⁻¹ with O-H stretching vibration.⁵¹ The peak around 1712 cm⁻¹ can be attributed to C=O stretching and finally the peak around 1592 cm⁻¹ can be attributed to C=C SP² stretching vibration of olefinic or conjugated carbon chains.⁶⁴

6.2.3.S3 results and discussion

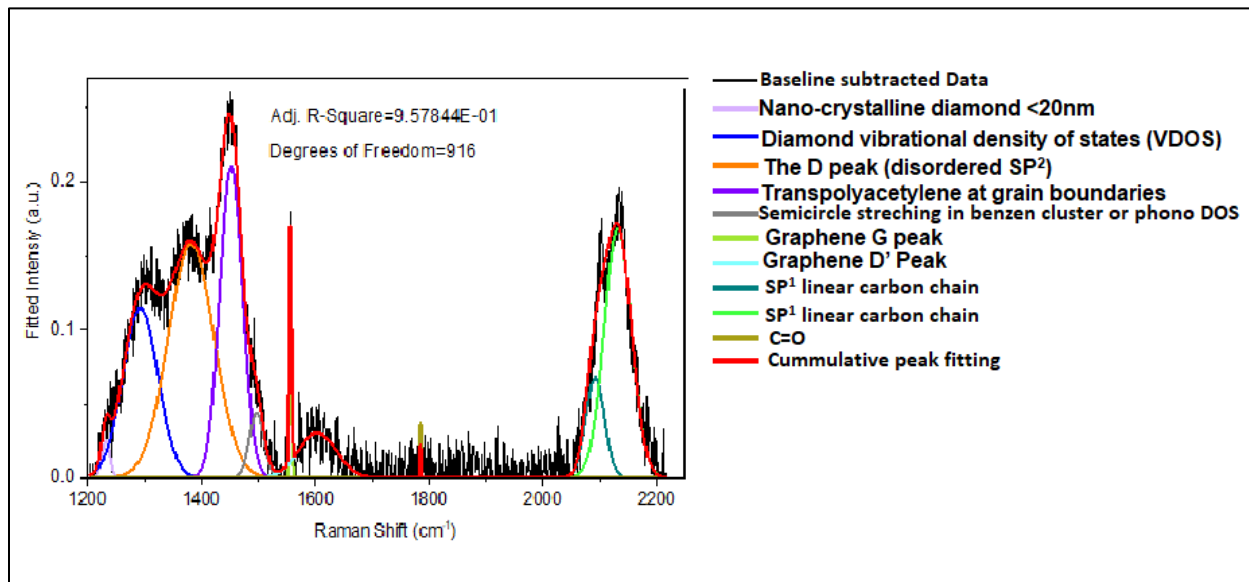


Figure 6. 10 S3 de-convoluted Raman spectrum in the range 1200-2200cm⁻¹ excited by 532nm laser wavelength at 50% laser

Table 6. 9 S3 fitting results

Peak Index	Fitting Peak type	FWHM	Center Grvty	Area IntgP
Nano-crystalline diamond <20nm	Gaussian	16.78	1231.99	0.84
Diamond vibrational density of states (VDOS)	Gaussian	72.93	1292.53	16.64
The D peak (disordered SP ²)	Gaussian	94.48	1381.78	29.76
Trans-polyacetylene at grain boundaries	Gaussian	46.82	1452.22	19.65
Semicircle stretching in benzene cluster or phonon DOS	Gaussian	30.16	1496.98	2.67
Graphene G peak	Gaussian	4.17	1556.26	1.40
Graphene D' Peak	Gaussian	78.11	1603.70	4.78
SP ¹ linear carbon chain	Gaussian	38.94	2091.82	5.25
SP ¹ linear carbon chain	Gaussian	56.22	2131.85	18.88
C=O	Gaussian	1.46	1785.31	0.10

Figure 6.10 shows the de-convolution results of the S3 Raman spectrum in the range 1200-2200cm⁻¹ excited by 532nm laser and table 6.9 shows the fitting results. Firstly, the grain boundaries related peaks can be seen from the graph namely the peak around 1452 cm⁻¹ which can be attributed to transpolyacetylene as explained earlier in section 5.2.2.3.

Secondly focusing on the diamond related peaks, the peak around 1292 cm^{-1} can be attributed to vibrational density of states (VDOS) in diamond and the peak around 1231 cm^{-1} can be attributed to nanocrystalline diamond with crystallite size less than 20nm. The absence of the single crystal diamond peak can be observed in this sample unlike S1 and S2. This could be explained by two scenarios: the crystallite size of the diamond content is small enough to produce the single crystal peak and/or the diamond particles are covered by SP^2 content in which case the SP^2 spectrum will cover the SP^3 due to resonance effects, which is also consistent with the observation of the SP^2 - SP^3 mixed sites detected in the FTIR measurement.

Looking at Graphene and SP^2 related peaks, the peak around 1381 cm^{-1} is the D peak. The peak around 1496 cm^{-1} can be attributed to semicircle stretching of carbon atom in benzene cluster or can be attributed to contribution from phonon DOS^{64,65}. The peak around 1556 cm^{-1} represents the graphene G peak and the peak around 1603 cm^{-1} represents the graphene D' peak.

Finally the two peaks around 2091 and 2131 cm^{-1} can be attributed to carbon SP^1 linear chains³⁶ and the peak around 1785 cm^{-1} can be attributed to C=O vibrations.⁵¹

6.2.4.S4 results and discussion

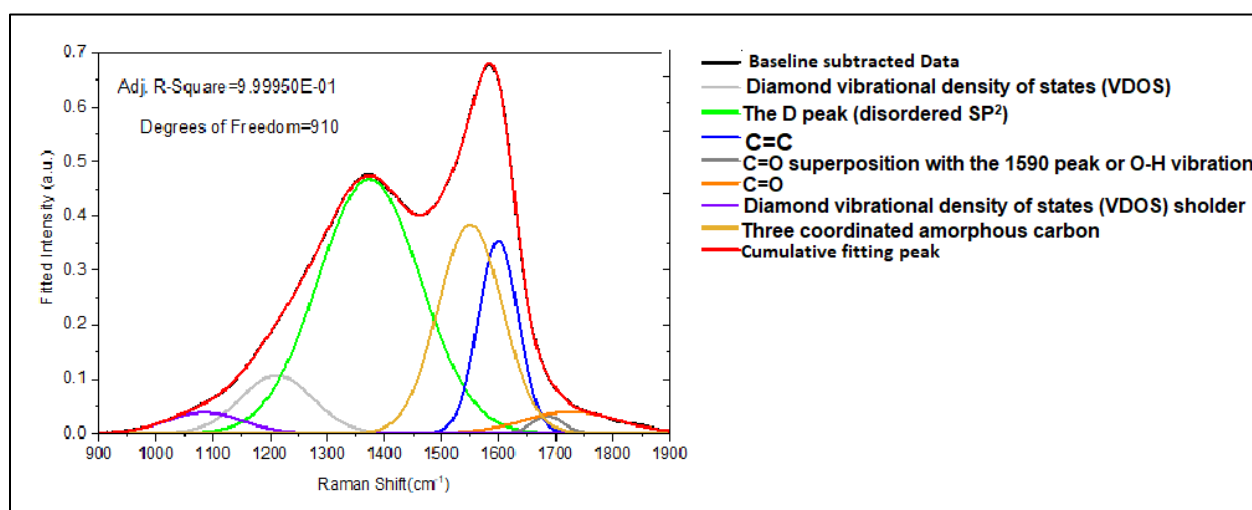


Figure 6. 11 S4 de-convoluted Raman spectrum in the range $900\text{-}1900\text{ cm}^{-1}$ excited by 532 nm laser wavelength at 50% laser power and 10S exposure time.

Table 6. 10 S4 fitting results

Peak Index	Fitting Peak type	FWHM	Center Grvty	Area IntgP
Diamond vibrational density of states (VDOS)	Gaussian	149.08	1211.50	7.55
The D peak (disordered SP ²)	Gaussian	211.66	1373.75	46.91
C=C	Gaussian	82.15	1599.70	13.78
C=O superposition with the 1590 peak or O-H vibration	Gaussian	64.07	1685.92	0.97
C=O	Gaussian	194.85	1727.18	3.71
Diamond vibrational density of states (VDOS) shoulder	Gaussian	156.48	1085.05	2.86
Three coordinated amorphous carbon	Gaussian	132.67	1550.34	2.42

Figure 6.11 shows the de-convolution results of the S4 Raman spectrum in the range 900-1900cm⁻¹ excited by 532nm laser and table 6.9 shows the fitting results. The absence of the grain boundaries peaks can be observed in this sample which can be a sign of amorphousness and the absence of any degree of crystallinity. The SP³ bonding related peaks are present around 1211 cm⁻¹ with its shoulder around 1085 cm⁻¹. Also graphene related peaks are absent which may be the effect of increasing of hydrogen content in the gases mixture as a trend can be observed of the decrease of crystallinity with increasing the hydrogen in the gases mixture from S1 to S4 was observed.

The peak around 1373 cm⁻¹ can be assigned as the D peak for disordered SP². The peak around 1599 cm⁻¹ can be attributed to C=C SP² stretching vibration of olefinic or conjugated carbon chains ⁶⁴. The peak around 1685 cm⁻¹ arises from a superposition of the SP² carbon band at 1592 cm⁻¹ with O-H stretching vibration ⁵¹. The peak around 1727 cm⁻¹ can be attributed to C=O stretching and finally the peak around 1550 cm⁻¹ can be attributed to three coordinated amorphous carbon.

6.2.5.S5 results and discussion

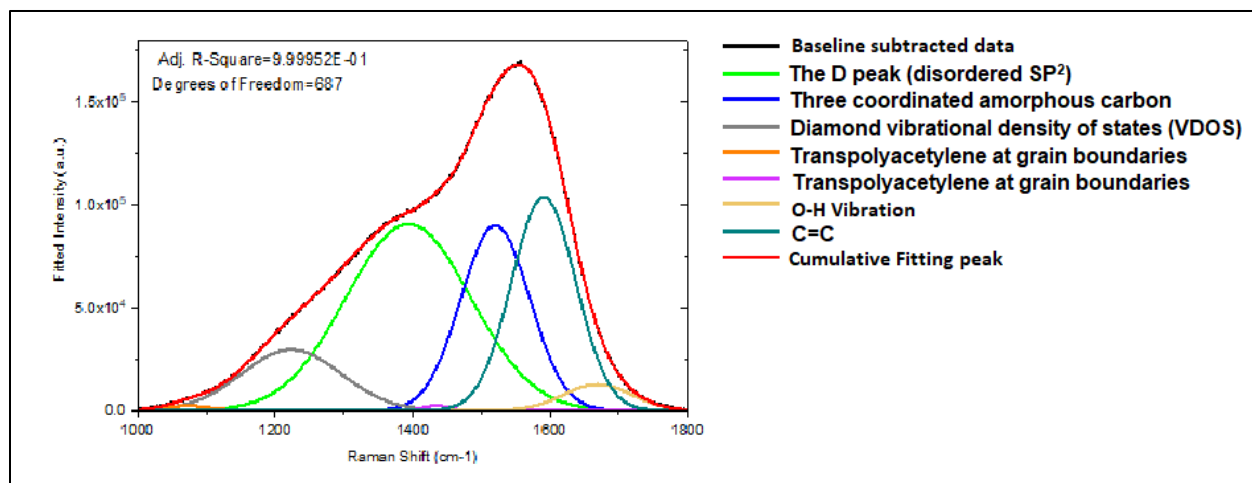


Figure 6. 12 S5 de-convoluted Raman spectrum in the range 1000-1800cm⁻¹ excited by 532nm laser wavelength at 50% laser power and 10S exposure time.

Table 6. 11 S5 fitting results

Peak Index	Fitting Peak type	FWHM	Center Grvty	Area IntgP
The D peak (disordered SP ²)	Gaussian	213.84	1393.89	40.16
Three coordinated amorphous carbon	Gaussian	117.98	1520.51	21.98
Diamond vibrational density of states (VDOS)	Gaussian	171.98	1223.57	10.49
Trans-polyacetylene at grain boundaries	Gaussian	78.43	1073.05	0.38
Trans-polyacetylene at grain boundaries	Gaussian	43.34	1433.81	0.23
O-H vibration	Gaussian	118.39	1669.35	3.13
C=C	Gaussian	109.94	1590.79	23.64

Figure 6.12 shows the de-convolution results of the S5 Raman spectrum in the range 1000-1800cm⁻¹ excited by 532nm laser and table 6.11 shows the fitting results. Firstly, the grain boundaries related peaks can be seen from the graph, namely, the peaks around 1073 and 1433 cm⁻¹ which can be attributed to transpolyacetylene as explained earlier in section 5.2.2.3.

Secondly, for diamond related peaks, the one around 1223 cm⁻¹ can be attributed to vibrational density of states (VDOS) in diamond. The grain boundaries peaks and the VDOS peak were also observed in this sample, however, the single crystal peak is absent, which can be explained by the crystallite size of the diamond content is being less than 20nm. It is interesting to note that this peak was observed for samples S2 and S3,

which were prepared at a lower deposition rate, indication a correlation between rate of growth and crystallinity. To sum up, increasing the pressure generally increases the deposition rate but decreases the crystallinity range in both SP² and SP³ content.

For SP² related peaks, the D in this sample peak is located at around 1393 cm⁻¹. The peak around 1520 cm⁻¹ can be attributed to three coordinated amorphous carbon. The peak around 1590 cm⁻¹ can be attributed to C=C SP² stretching vibration of olefinic or conjugated carbon chains⁶⁴. And finally, the peak around 1669 cm⁻¹ can be attributed to the O-H vibration.

6.2.6. S6 results and discussion

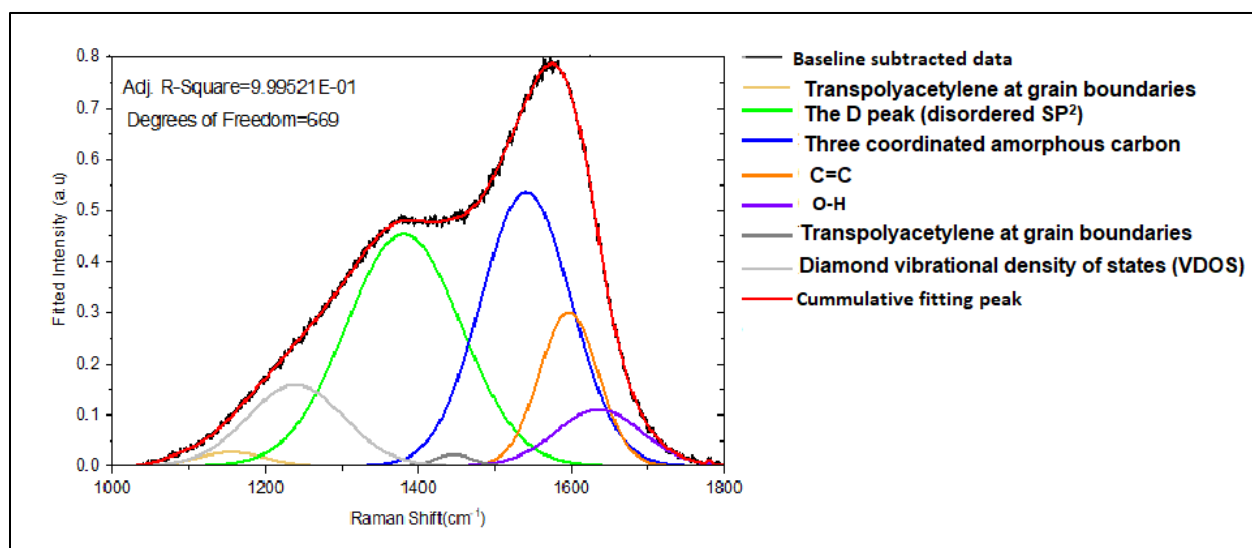


Figure 6. 13 S6 de-convoluted Raman spectrum in the range 1000-1800cm⁻¹ excited by 532nm laser wavelength at 50% laser power and 10S exposure time.

Table 6. 12 S6 fitting results

Peak Index	Fitting Peak type	FWHM	Center Grvty	Area IntgP
Trans-polyacetylene at grain boundaries	Gaussian	100.74	1155.08	1.23
The D peak (disordered SP ²)	Gaussian	177.24	1380.87	35.65
Three coordinated amorphous carbon	Gaussian	139.31	1540.79	33.07
C=C	Gaussian	90.44	1596.77	12.05
O-H vibration	Gaussian	132.71	1635.77	6.52
Trans-polyacetylene at grain boundaries	Gaussian	55.68	1446.06	0.56
Diamond vibrational density of states (VDOS)	Gaussian	148.31	1239.38	10.45

Figure 6.13 shows the de-convolution results of the S6 Raman spectrum in the range 1000-1800cm⁻¹ excited by 532nm laser and table 6.12 shows the fitting results. Firstly, the grain boundaries related peaks can be seen from the graph namely the peak around 1155 and 1446 cm⁻¹ which can be attributed to trans-polyacetylene as explained earlier in section 5.2.2.3.

Secondly, for diamond related peaks, the peak around 1239 cm⁻¹ can be attributed to vibrational density of states (VDOS) in diamond. Similar to S5 the grain boundaries peaks and the VDOS peak were observed in this sample, but the single crystal peak is absent which can be again explained by the crystallite size is being less than 20nm.

SP² related peaks, the D in this sample peak is located at around 1380 cm⁻¹. The peak around 1540 cm⁻¹ can be attributed to three coordinated amorphous carbon. The peak around 1596 cm⁻¹ can be attributed to C=C SP² stretching vibration of olefinic or conjugated carbon chains⁶⁴. And finally the peak around 1635 cm⁻¹ can be attributed to the O-H vibration.

6.2.7.S7 results and discussion

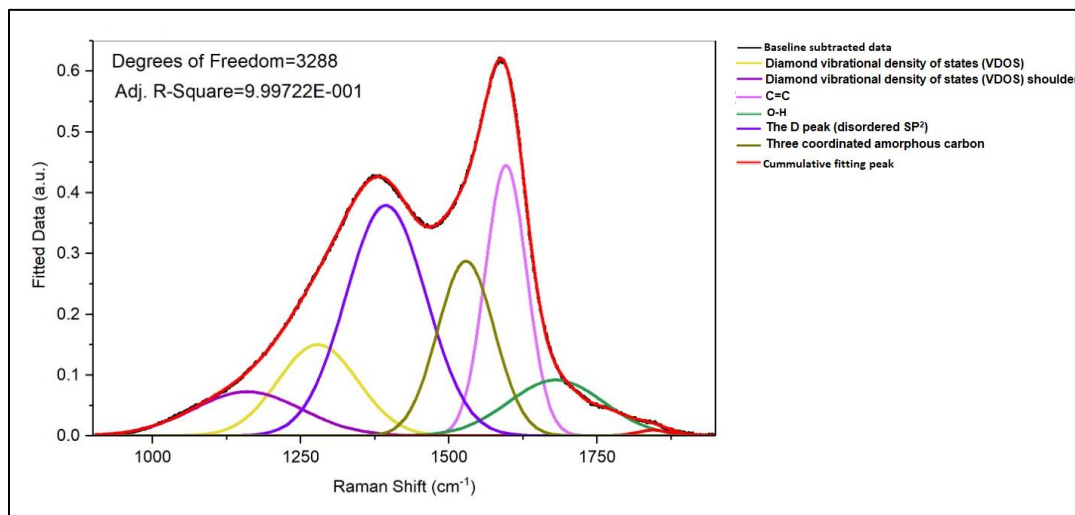


Figure 6. 14 S7 de-convoluted Raman spectrum in the range 900-1900cm⁻¹ excited by 532nm laser wavelength at 50% laser power and 10S exposure time.

Table 6. 13 S7 fitting results

Peak Index	Fitting Peak type	FWHM	Center Grvty	Area IntgP
Diamond vibrational density of states (VDOS)	Gaussian	158.61	1279.01	8.18
Diamond vibrational density of states (VDOS) shoulder	Gaussian	216.00	1160.20	5.36
C=C	Gaussian	82.42	1596.48	12.61
O-H	Gaussian	188.58	1680.92	5.95
The D peak (disordered SP ²)	Gaussian	159.86	1393.95	20.83
Three coordinated amorphous carbon	Gaussian	113.00	1529.08	11.16

Figure 6.14 shows the de-convolution results of the S4 Raman spectrum in the range 900-1900cm⁻¹ excited by 532nm laser and table 6.13 shows the fitting results. The absence of the grain boundaries peaks can be observed in this sample which can be a sign of amorphousness and the absence of any degree of crystallinity in this sample. The SP³ bonding related signals are present as a peak at around 1279 cm⁻¹ and its shoulder around 1160 cm⁻¹. Also graphene related peaks are absent which may be the effect of increasing the hydrogen content in the gases mixture similar to the trend observed for samples S1 to S4.

The peak around 1393 cm⁻¹ is the D peak for disordered SP². The peak around 1596 cm⁻¹ can be attributed to C=C SP² stretching vibration of olefinic or conjugated carbon chains⁶⁴. The peak around 1680 cm⁻¹ can be arises from O-H stretching vibration⁵¹. And finally the peak around 1529 cm⁻¹ can be attributed to three coordinated amorphous carbon.

6.3. UV-Visible and Band gap Measurements

Three selected samples, namely S5, S6 and S7, were chosen for further investigation with UV-Visible spectroscopy in order to evaluate their band gap as well as the position of defect levels in the band gap, which are essential characters for radiation measurement. The band structure of each sample was constructed using the Tauc fitting method as explained earlier in section 5.2.3.

6.3.1. S5 Band gap measurement

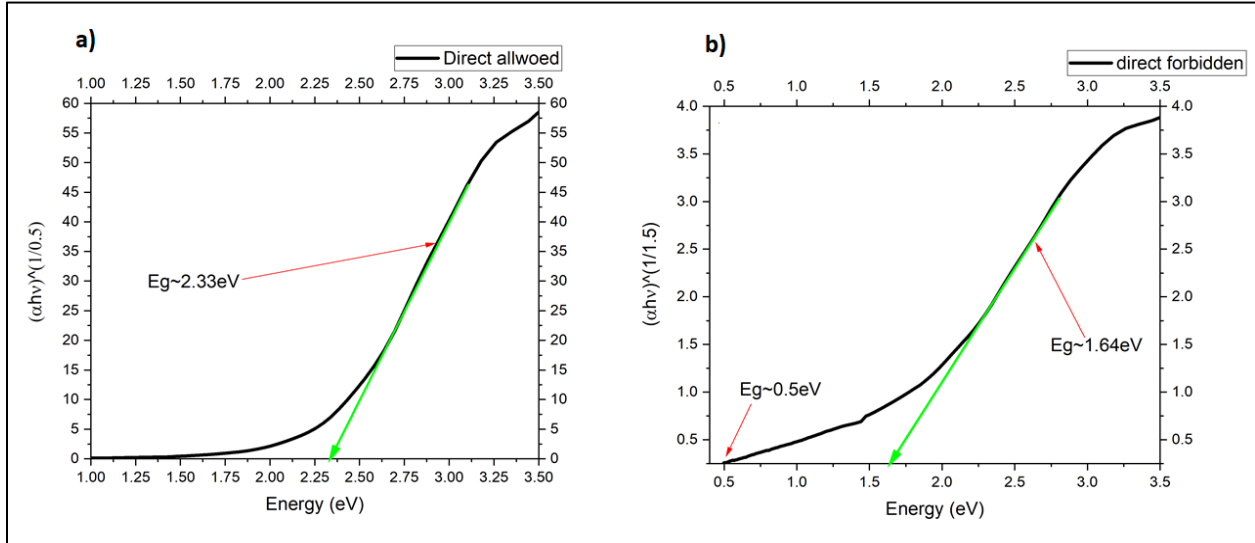


Figure 6. 15 S5 UV-Visible data fitted to Tauc equation a) for m value 0.5 representing direct allowed transition, b) for m value 1.5 representing direct forbidden transition.

Figure 6.15 shows S5 UV-Visible data fitted to the Tauc equation. In figure 6.15a, the fitting parameter $m=0.5$, representing direct allowed transition. By extrapolating the linear portion in the graph at the value for the optical band gap will be obtained from the intersection of the line with the X-axis (E_g 2.3eV). In figure 6.15 b, $m=1.5$ representing direct forbidden transition due to two types of defects. Firstly, a deep defect close to the middle of the band gap at 1.64eV. The other defect is a shallow defect located at 0.5eV. This is indicative of a shallow defect close to the conduction band which can be considered as an electron trap playing an essential role in the I-V behavior as well as the radiation response as will be seen in the next section. Based on this data an energy band structure for S5 is presented in figure 6.18.

6.3.2.S6 Band gap measurement

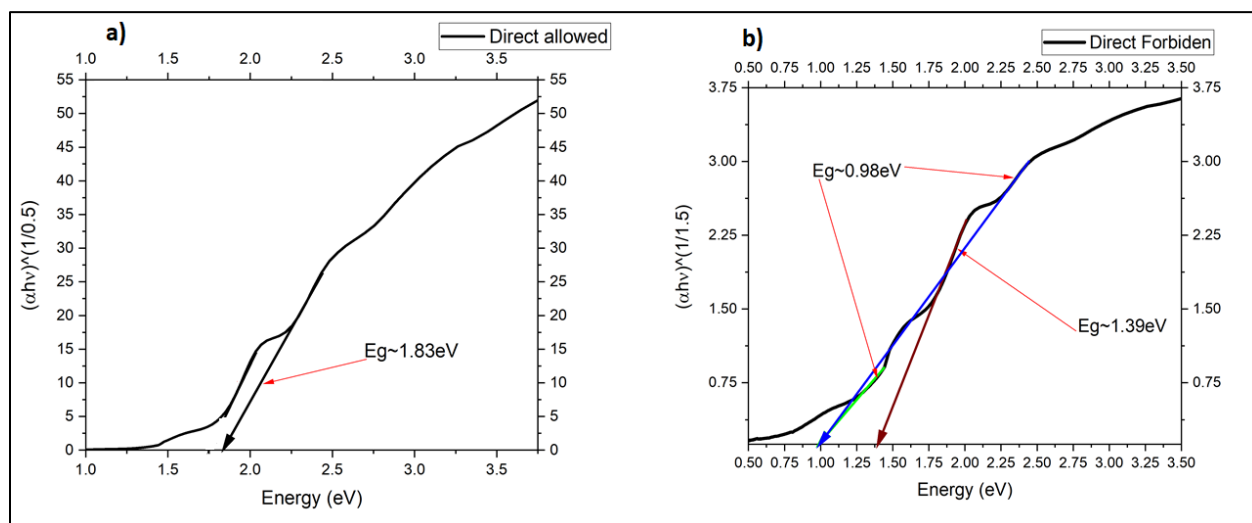


Figure 6. 16 S6 UV-Visible data fitted to Tauc equation a) for m value 0.5 representing direct allowed transition, b) for m value 1.5 representing direct forbidden transition.

Figure 6.16 shows the S6 UV-Visible data fitted to the Tauc equation. In figure 6.16a, $m = 0.5$ for direct allowed transition, giving a value for the optical band gap, $E_G = 1.83 \text{ eV}$. In figure 6.16 b, $m = 1.5$ for direct forbidden transition. We observe a deep defect close to the middle of the band gap at 0.98 eV , and another defect is located at 1.39 eV , indicative of a hole trap close to the valence band. Based on this data an energy band structure for S6 is presented in figure 6.18.

6.3.3. S7 Band gap measurement

Figure 6.17 shows the S7 UV-Visible data fitted to the Tauc equation. In figure 6.17a, $m = 0.5$ for direct allowed transition, giving an energy gap $E_G = 1.92 \text{ eV}$. In figure 6.17 b, $m = 1.5$ for direct forbidden transition. We observe a deep defect close to the middle of the band gap at 1.03 eV , and a defect located at 0.26 eV . The

shallow defect is close to the conduction band which and can be considered as an electron trap. Based on this data an energy band structure for S7 is presented in figure 6.18.

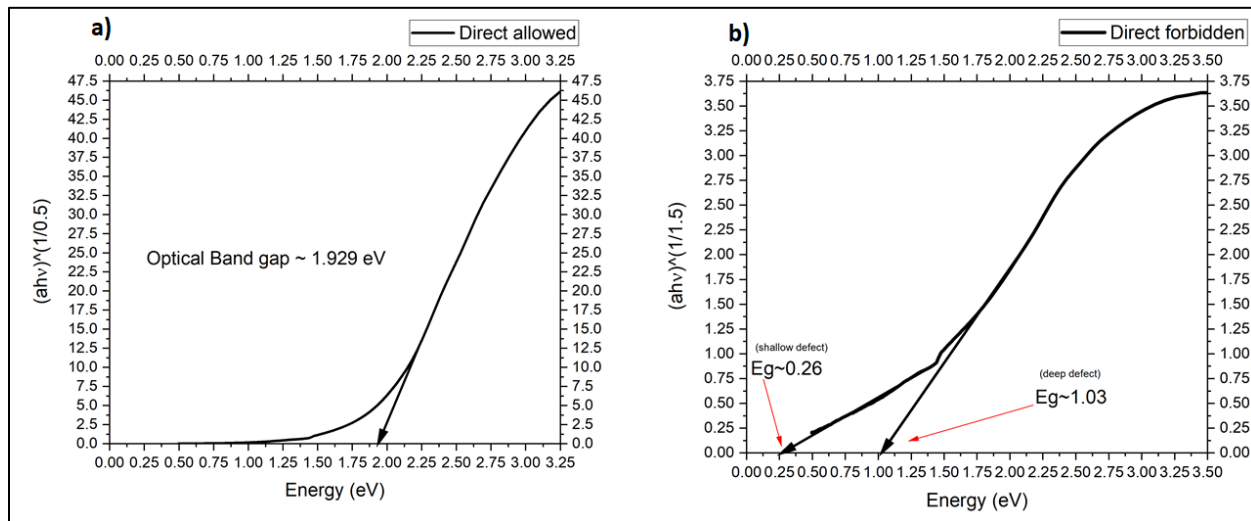


Figure 6. 17 S7 UV-Visible data fitted to Tauc equation a) for m value 0.5 representing direct allowed transition, b) for m value 1.5 representing direct forbidden transition.

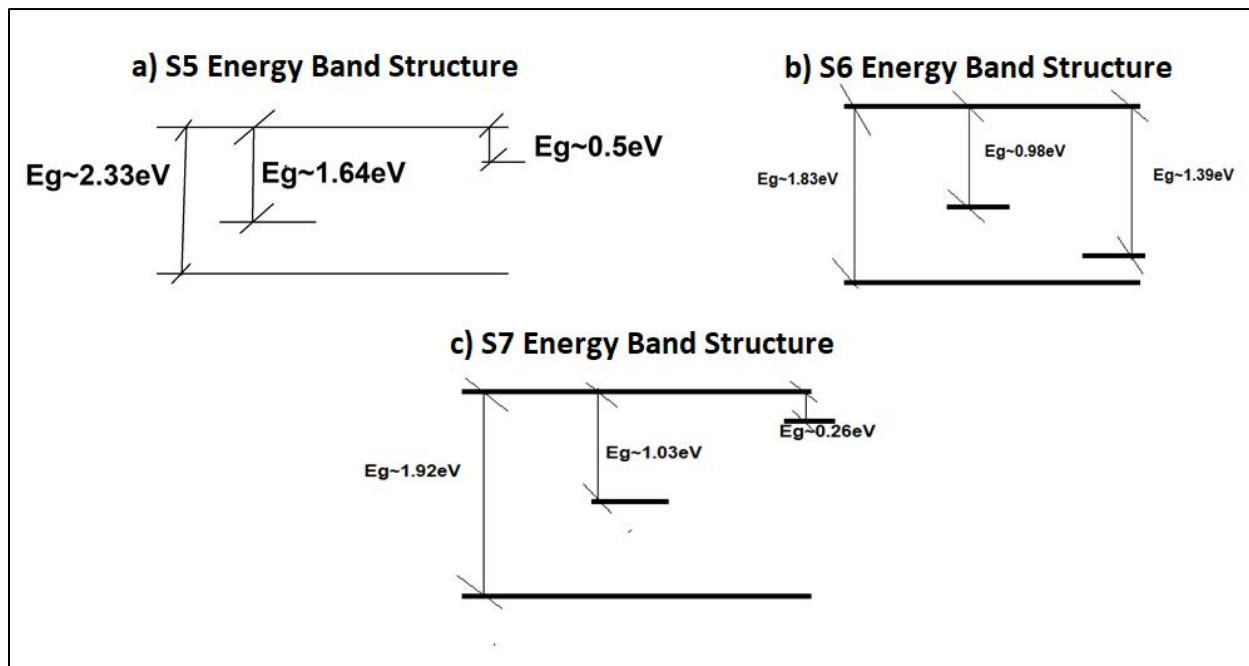


Figure 6. 18 Schematic diagram showing the energy band diagram of the three samples.

6.4. I-V Characteristics and Radiation Experiments

6.4.1. S5 dark measurement

Figure 6.19a shows the S5 I-V characteristic curve recorded in dark condition from +10V to -10V in both forward direction (when the applied voltage started from +Ve value and going down to -Ve value.) and

reverse direction (when the applied voltage started from -Ve value and going up to +Ve value) figure 6.19b shows the schematic diagram for the connection set up.

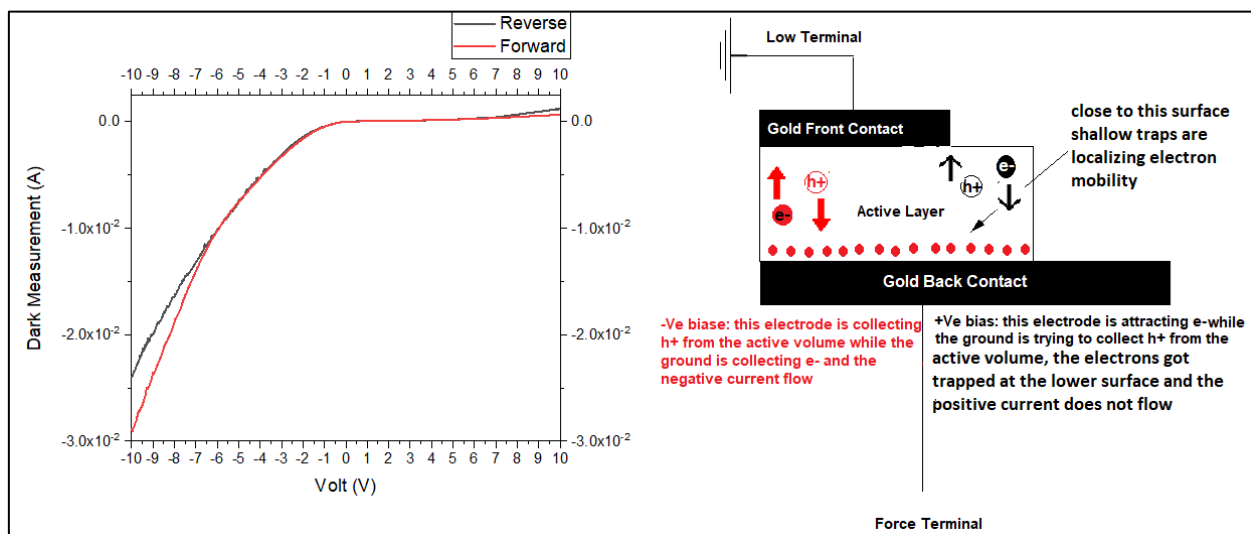


Figure 6. 19 a) S5 I-V characteristic curve recorded in the dark condition from +10V to -10V in both forward direction and reverse direction, b) schematic diagram for the connection set up.

To provide a possible explanation for the behavior seen in the graph let's assume that the majority of shallow (interface) defects that were detected in the UV-Visible measurement are accumulated at the back gold contact interface with the carbon layer while the front contact interface with the carbon layer is free of these traps. It is worth mentioning that the back gold contacted has experienced annealing treatment through being heated during the film deposition while the front contact was deposited on the film and didn't have such treatment. As these defects are located near the conduction band, they would act as electron traps and reduce electron transport through this contact.

On the negative biasing part, the back terminal (where the shallow defects are localized) is attracting holes from the active volume while the ground terminal is attracting electrons from the active volume through the front contact(the free defect interface). Consequently a relatively high negative current flows as can be seen from the figure.

On the positive biasing part, the back (where shallow defects are localized) terminal is attracting electrons that must go through electron interface traps while the ground terminal is attracting holes. Consequently, a very small positive current flow as can be seen from the figure. The small shift between the forward direction and the reverse direction can be explained by the transient behavior in the trapping/de-trapping mechanism when applying negative bias as reported by Yiuri et al. in their study about the effects of shallow traps on the reverse current of diamond Schottky diode ⁶⁶. To investigate more about the validity of

the assumption that the shallow traps are accumulated at one electrode and not the other, the dark measurement was repeated after flipping the connection electrodes connection as presented in figure 6.20.

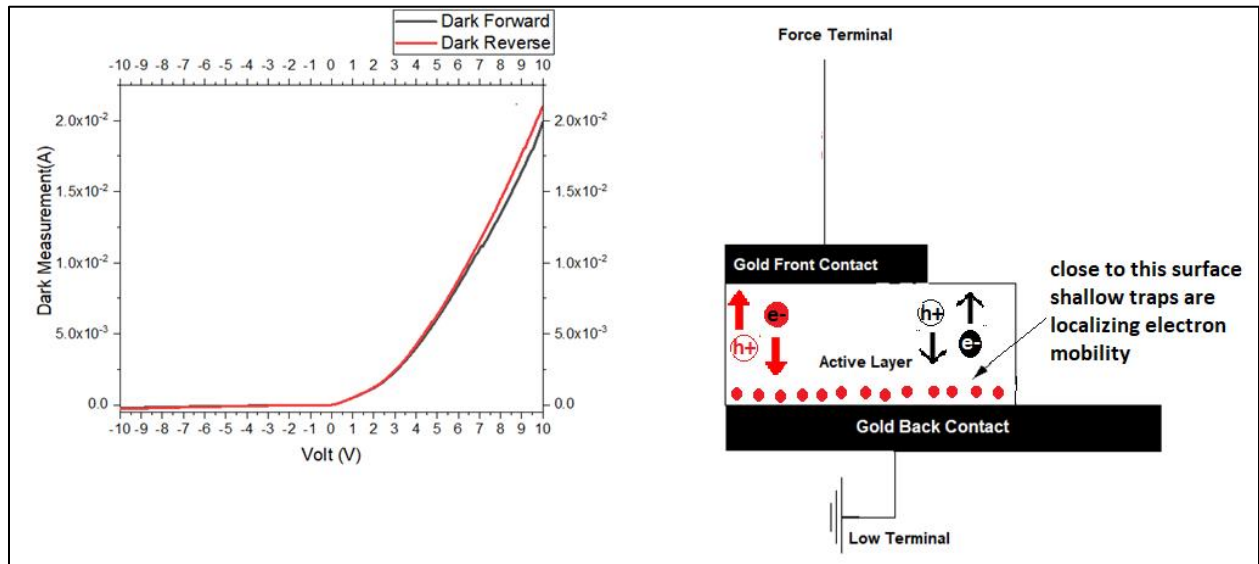


Figure 6. 20 S5 I-V characteristic curve recorded in the dark condition from +10V to -10V in both forward direction and reverse direction, flipped configuration.

In this configuration, during the positive biasing the front terminal is trying to attract electrons from the active volume, while the ground terminal is trying to attract holes through the back contact and consequently a high positive current flow as can be seen from the figure. In the negative biasing, the force terminal is trying to attract holes, while the ground terminal attracts electrons. Consequently a very small current flow as can be seen from the figure.

6.4.2.S5 radiation measurement

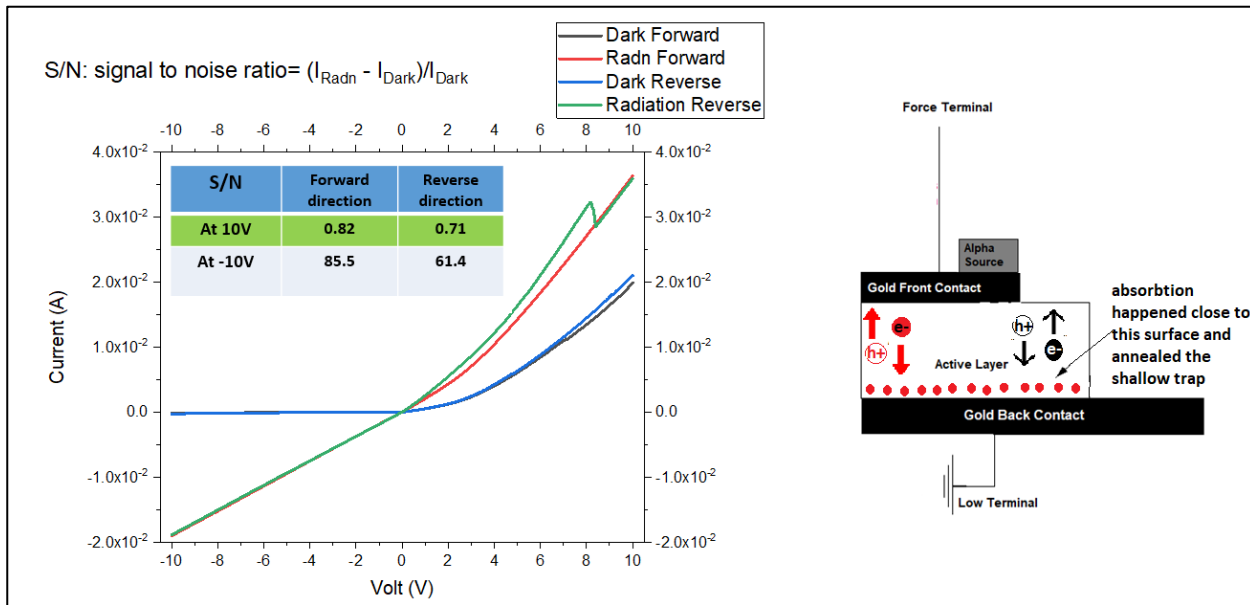


Figure 6. 21 S5 I-V characteristic curve recorded under irradiation condition from +10V to -10V in both forward direction and reverse direction and schematic diagram for the connection set up and the source-sample configuration.

Figure 6.21 shows the S5 I-V characteristic curve recorded under irradiation condition from +10V to -10V in both forward direction and reverse direction and schematic diagram for the connection set up and the source-sample configuration. As the radiation source is introduced, the alpha particles is being absorbed in the carbon layer creating e-h pairs which work on annealing the shallow traps at the interface by filling these defect levels and allowing the current to flow.

To investigate whether the radiation has caused a permanent effect on the sample or not, the dark measurement was recorded again after radiation exposure and compared to that before radiation and shown in figure 6.22.

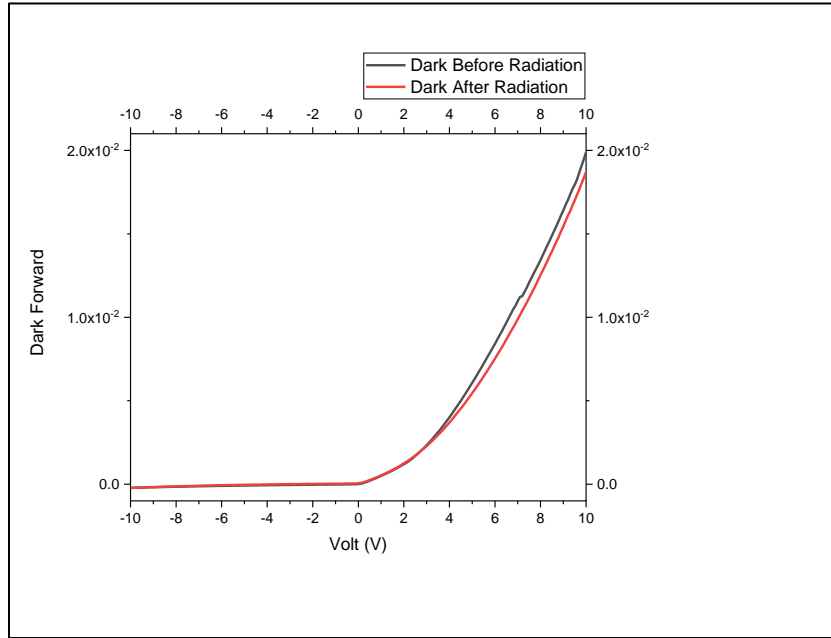


Figure 6. 22 S5 dark measurement comparison before and after radiation.

It can be seen from figure 6.22 that, Identical behavior is observed in the negative side with a very little shift in the positive current which confirms the suggestion of trap filling mechanism in interpreting the radiation response and also indicates that exposure to radiation tends to decrease the dark current through filling the defect levels.

It has been reported that, it is a common practice to give diamond detectors a pre-irradiation dose or what is known as “prime dose” to anneal the effects of the shallow traps and stabilize the sensor response⁶⁷⁻⁶⁹. To investigate more about the pre-irradiation effects, one of the samples was exposed to the source for 24 hours and the dark current was compared before and after the irradiation, as can be seen from figure 6.23. Pre-irradiating the sample has the effect of reducing the dark current which can be explained by filling mechanism of the shallow defects in the material.

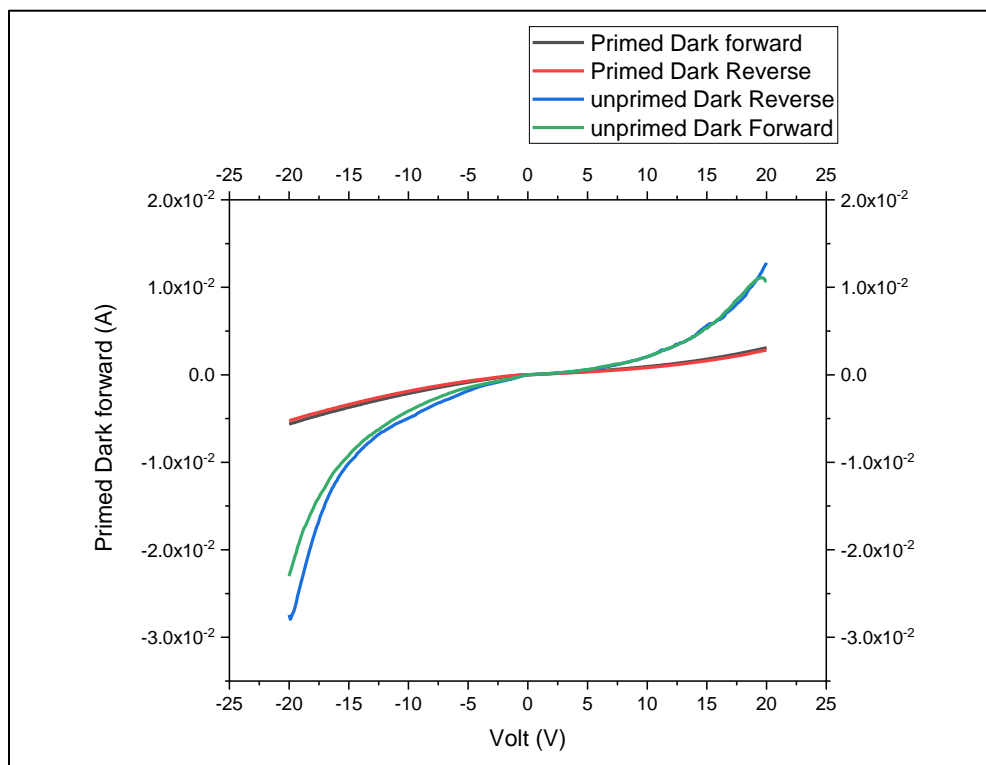


Figure 6. 23 effect of giving the sensor a prime dose on the Dark current.

6.4.3. S6 radiation measurement

It can be seen from figure 6.24 that sample S6 is providing a better signal to noise ratio than sample S5, which can be attributed to the better crystallinity in S6 as seen from the Raman and FTIR measurement. Also similar to S5, S6 is giving a better response at negative biasing than positive biasing and almost identical behaviors before and after radiation.

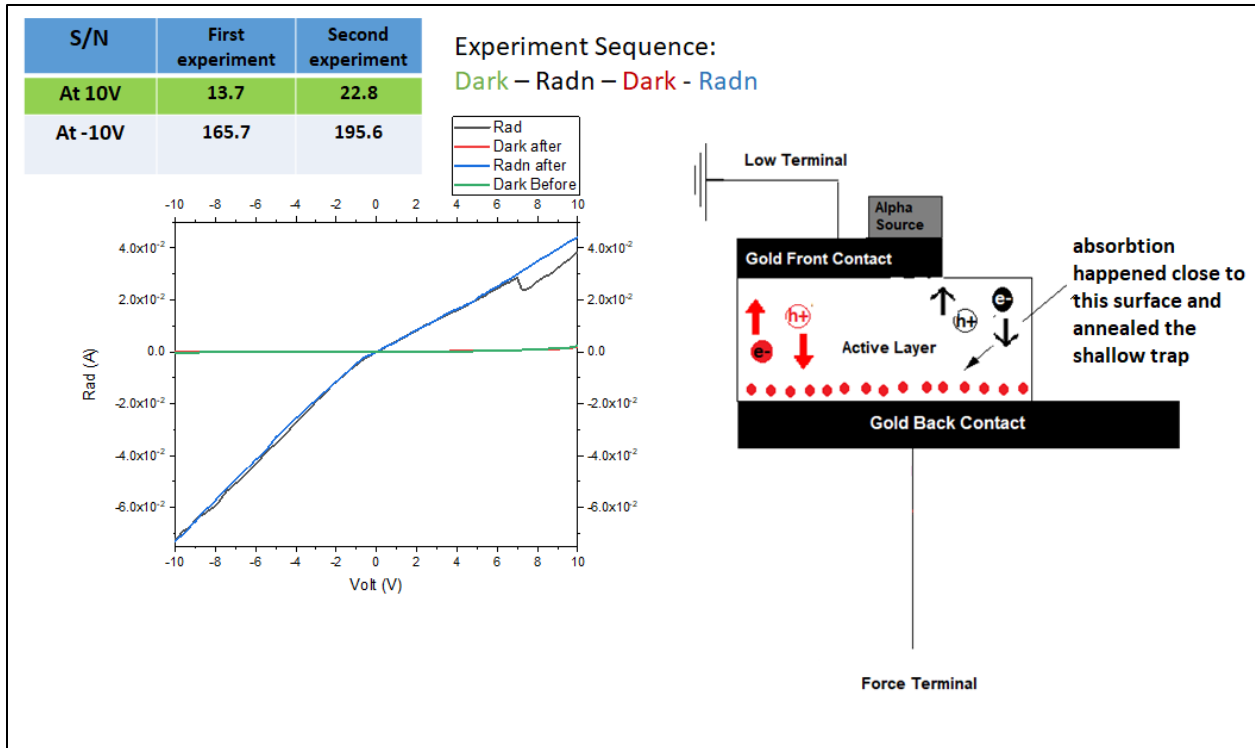
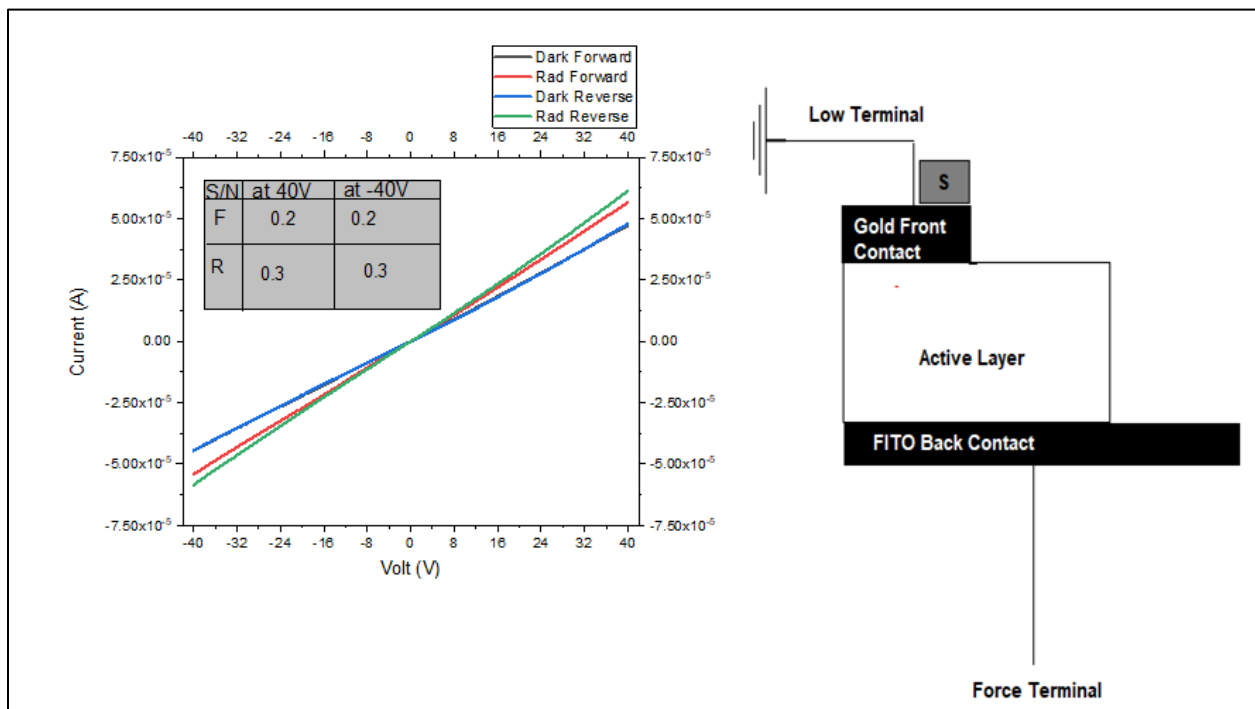


Figure 6. 24 S6 I-V characteristic curve recorded under dark and irradiation condition from +10V to -10V in both forward direction and reverse direction and schematic diagram for the connection set up and the source-sample configuration.

6.4.4. S7 radiation measurement



S7 is the only sample that showed a perfectly ohmic conductivity unlike S5 and S6 which were more schottky-like. A possible explanation for this symmetry is that, the mechanism of e- and h+ injection/collection from the FITO is different than for the Gold electrode. Also the signal to noise ratio is very small when compared to S5 and S6 which can be explained by the poor crystallinity in S7 as seen from the Raman and the FTIR measurements.

7. Conclusions and Recommendations for Future Work

7.1. Conclusions

The two main goals of this projects were to, firstly, establish the feasibility of thin-film nano structured diamond materials as a replacement for Diamond-based radiation monitoring, and, secondly, to evaluate the best materials properties for effective radiation monitoring applications.

In order to control film properties, they were correlated to preparation conditions, leading to the following observations:

Increasing the hydrogen content in the gases ratios decreases the degree of crystallinity and the optical band gap of the resulted film. Increasing the deposition pressure increases the deposition rate and consequently decreases the range of crystallinity. It was also observed that graphene can be deposited at pressures equal to or less than 80 mTorr.

Film characterization was then followed by radiation experiments, and the film responses were correlated with their opto-electronic characteristics. It was established that the electron and hole mobilities are mainly affected by the presence and location of shallow defects. Deep defect levels are present in all samples near the middle of band gap, and act mainly as recombination centers.

A primary radiation response was successfully measured for sample S5, prepared at 100% CH₄ and 500 mTorr deposition pressure, and for sample S6, prepared at 100% CH₄ and 160mTorr. Furthermore, the reproducibility of the radiation response was successfully verified by measuring the dark current, after removing the radiation source, in order to confirm that the measured radiation response is solely due to radiation and there is no permanent damage for the samples. Both samples showed the same dark current characteristics, before and after radiation, with a small shift in S5 to a smaller dark current, which can be attributed to the filling of shallow defects.

These result validate the choice of nano-structured diamond thin-film as possible replacement for Diamond. Additionally, it was observed that the radiation response is not only dependent on the band gap but also on the defect levels inside the band gap, the ease in filling these traps and their contribution to the dark current. Electron traps are the most damaging type of defects, likely due to the fact that electron transport is more impactful than hole transport due to the higher electron mobilities.

Pre-irradiation of the samples was performed to verify the effects of radiation on the electronic properties. Two effects were observed: 1. A reduction in the dark current, and 2. a more symmetric I-V curve for the positive and negative sides.

This can be interpreted in two ways, as follows: the pre-irradiation works on curing the interface defects and possibly anneals their effect, or, alternatively, there is temporary filling of the traps during irradiation. The latter seems more probable since dark I-V characteristics after pre-irradiation go back to the original asymmetric behavior. It should be reminded that the bottom gold layer is annealed prior to deposition, but the top layer is not.

Finally, it was observed that the best radiation response is related to the sample with high crystallinity and absence of electron traps (S6).

7.2. Future Work

It has been established that sample S6 is the most promising candidate for radiation detection application, and should form the basis for further investigation. Thicker samples with the same opto-electronic characteristics should be tested. Further characterization techniques are also needed, such as Photoluminescence spectroscopy, to get better understanding of the density of these defect levels. UV-Raman and XPS can be used to draw a better understanding of the sp^3 content and its range of crystallinity.

Further radiation testing is also needed, such as testing the radiation response against other types of radiation (neutrons, x-rays and/or gamma-rays). Also more sophisticated set ups like measuring the signal with a pre-amplifier and amplifier circuit would give a better understanding of a pulse height spectrum and charge collection efficiency.

A better substrate cooling mechanism so that the samples can be quickly cooled from the deposition temperature to room temperature would increase the chances to prepare more crystalline diamond with less sp^2 content at relatively low preparation temperature.

The low pressure region is very promising for preparation of graphene based materials especially if a metallic substrate is used as it is well known as a catalyst for graphene growth.

Finally, the sandwich metallization process should be improved to eliminate interface defects.

References

- (1) Gracio, J. J.; Fan, Q. H.; Madaleno, J. C. Diamond Growth by Chemical Vapour Deposition. *J. Phys. D: Appl. Phys.* **2010**, *43* (37), 374017. <https://doi.org/10.1088/0022-3727/43/37/374017>.
- (2) Lim, P. K.; Gaspari, F.; Zukotynski, S. Structural Properties of A-C:H Deposited Using Saddle-field Glow-discharge Decomposition of Methane. *Journal of Applied Physics* **1995**, *78* (9), 5307–5312. <https://doi.org/10.1063/1.359707>.
- (3) Mathur, R. B.; Singh, B. P.; Pande, S. *Carbon Nanomaterials: Synthesis, Structure, Properties and Applications*, 0 ed.; Taylor & Francis, 2016. <https://doi.org/10.1201/9781315371849>.
- (4) Shahzad, M. I.; Tagliaferro, A. Introduction to Carbon Materials. In *Carbon for Sensing Devices*; Demarchi, D., Tagliaferro, A., Eds.; Springer International Publishing: Cham, 2015; pp 3–14. https://doi.org/10.1007/978-3-319-08648-4_1.
- (5) Pierson, H. O. The Fullerene Molecules. In *Handbook of Carbon, Graphite, Diamonds and Fullerenes*; Elsevier, 1993; pp 356–373. <https://doi.org/10.1016/B978-0-8155-1339-1.50020-7>.
- (6) Vidu, R.; Rahman, M.; Mahmoudi, M.; Enachescu, M.; Poteca, T.; Opris, I. Nanostructures: A Platform for Brain Repair and Augmentation. *Frontiers in systems neuroscience* **2014**, *8*, 91. <https://doi.org/10.3389/fnsys.2014.00091>.
- (7) Ferrari, A. C.; Meyer, J. C.; Scardaci, V.; Casiraghi, C.; Lazzeri, M.; Mauri, F.; Piscanec, S.; Jiang, D.; Novoselov, K. S.; Roth, S.; Geim, A. K. Raman Spectrum of Graphene and Graphene Layers. *Phys. Rev. Lett.* **2006**, *97* (18), 187401. <https://doi.org/10.1103/PhysRevLett.97.187401>.
- (8) Novoselov, K. S.; Jiang, D.; Schedin, F.; Booth, T. J.; Khotkevich, V. V.; Morozov, S. V.; Geim, A. K. Two-Dimensional Atomic Crystals. *Proc Natl Acad Sci U S A* **2005**, *102* (30), 10451. <https://doi.org/10.1073/pnas.0502848102>.
- (9) Hirsch, A. The Era of Carbon Allotropes. *Nature Materials* **2010**, *9* (11), 868–871. <https://doi.org/10.1038/nmat2885>.
- (10) Pierson, H. O. Properties, Processing and Applications. 417.
- (11) Bernal, J. D.; Bragg, W. L. The Structure of Graphite. *Proceedings of the Royal Society of London. Series A, Containing Papers of a Mathematical and Physical Character* **1924**, *106* (740), 749–773. <https://doi.org/10.1098/rspa.1924.0101>.
- (12) Wort, C. J. H.; Balmer, R. S. Diamond as an Electronic Material. *Materials Today* **2008**, *11* (1), 22–28. [https://doi.org/10.1016/S1369-7021\(07\)70349-8](https://doi.org/10.1016/S1369-7021(07)70349-8).
- (13) Berdermann, E.; Badura, E.; Neyer, C.; Schulze, R.; Stelzer, H. Diamond Detectors for Heavy Ion Measurements. *Nuclear Physics B - Proceedings Supplements* **1998**, *61* (3), 399–403. [https://doi.org/10.1016/S0920-5632\(97\)00593-8](https://doi.org/10.1016/S0920-5632(97)00593-8).
- (14) Jacob, W.; Möller, W. On the Structure of Thin Hydrocarbon Films. *Appl. Phys. Lett.* **1993**, *63* (13), 1771–1773. <https://doi.org/10.1063/1.110683>.
- (15) Ferrari, A. C. Non-Destructive Characterisation of Carbon Films. In *Tribology of Diamond-Like Carbon Films*; Donnet, C., Erdemir, A., Eds.; Springer US: Boston, MA, 2008; pp 25–82. https://doi.org/10.1007/978-0-387-49891-1_2.
- (16) Chu, P. K.; Li, L. Characterization of Amorphous and Nanocrystalline Carbon Films. *Materials Chemistry and Physics* **2006**, *96* (2–3), 253–277. <https://doi.org/10.1016/j.matchemphys.2005.07.048>.
- (17) Lacerda, R. G.; Hammer, P.; Lepienski, C. M.; Alvarez, F.; Marques, F. C. Hard Graphitic-like Amorphous Carbon Films with High Stress and Local Microscopic Density. *Journal of Vacuum Science & Technology A* **2001**, *19* (3), 971–975. <https://doi.org/10.1116/1.1365130>.
- (18) Zhang, L.; Wei, X.; Wang, F. A Ternary Phase Diagram for Amorphous Carbon. *Carbon* **2015**, *94*. <https://doi.org/10.1016/j.carbon.2015.06.055>.

- (19) Das, D. Nanocrystalline Diamond. In *Carbon-Based Nanofillers and Their Rubber Nanocomposites*; Elsevier, 2019; pp 123–181. <https://doi.org/10.1016/B978-0-12-813248-7.00005-5>.
- (20) Williams, O. A. Nanocrystalline Diamond. *Diamond and Related Materials* **2011**, *20* (5–6), 621–640. <https://doi.org/10.1016/j.diamond.2011.02.015>.
- (21) Gruen, D. M. Ultrananocrystalline Diamond in the Laboratory and the Cosmos. *MRS Bulletin* **2001**, *26* (10), 771–776. <https://doi.org/10.1557/mrs2001.204>.
- (22) Carvalho, A. F.; Holz, T.; Santos, N. F.; Ferro, M. C.; Martins, M. A.; Fernandes, A. J. S.; Silva, R. F.; Costa, F. M. Simultaneous CVD Synthesis of Graphene-Diamond Hybrid Films. *Carbon* **2016**, *98*, 99–105. <https://doi.org/10.1016/j.carbon.2015.10.095>.
- (23) Yuan, Q.; Liu, Y.; Ye, C.; Sun, H.; Dai, D.; Wei, Q.; Lai, G.; Wu, T.; Yu, A.; Fu, L.; Chee, K. W. A.; Lin, C.-T. Highly Stable and Regenerative Graphene–Diamond Hybrid Electrochemical Biosensor for Fouling Target Dopamine Detection. *Biosensors and Bioelectronics* **2018**, *111*, 117–123. <https://doi.org/10.1016/j.bios.2018.04.006>.
- (24) Ahmed, S. N. *Physics and Engineering of Radiation Detection*, 2nd edition.; Elsevier: Waltham, MS, 2014.
- (25) Squillante, M. R.; Christian, J. F.; Entine, G. Solid State Radiation Detectors. In *Wiley Encyclopedia of Electrical and Electronics Engineering*; John Wiley & Sons, Inc.: Hoboken, NJ, USA, 2016; pp 1–18. <https://doi.org/10.1002/047134608X.W5214.pub2>.
- (26) Solid-State Radiation Detectors. 412.
- (27) Grdanovska, S. CHARACTERIZATION OF RADIATION DAMAGE TO A NOVEL PHOTONIC CRYSTAL SENSOR, 2015. <https://doi.org/10.13016/M2BZ0D>.
- (28) Khan, F. M. *The Physics of Radiation Therapy*, 3rd ed.; Lippincott Williams & Wilkins: Philadelphia, 2003.
- (29) Thompson, J. M. T.; May, P. W. Diamond Thin Films: A 21st-Century Material. *Philosophical Transactions of the Royal Society of London. Series A: Mathematical, Physical and Engineering Sciences* **2000**, *358* (1766), 473–495. <https://doi.org/10.1098/rsta.2000.0542>.
- (30) Prelas, M. A.; Popovici, G.; Bigelow, L. K. *Handbook of Industrial Diamonds and Diamond Films*; CRC Press, 2018.
- (31) *Handbook of Thin-Film Technology*; Frey, H., Khan, H. R., Eds.; Springer Berlin Heidelberg: Berlin, Heidelberg, 2015. <https://doi.org/10.1007/978-3-642-05430-3>.
- (32) Gaspari, F.; Zukotynski, S.; Perz, J. M. Density of States of Inhomogeneous Hydrogenated Amorphous Silicon. *Journal of Non-Crystalline Solids* **1992**, *143*, 241–245. [https://doi.org/10.1016/S0022-3093\(05\)80572-1](https://doi.org/10.1016/S0022-3093(05)80572-1).
- (33) Țucureanu, V.; Matei, A.; Avram, A. M. FTIR Spectroscopy for Carbon Family Study. *Critical Reviews in Analytical Chemistry* **2016**, *46* (6), 502–520. <https://doi.org/10.1080/10408347.2016.1157013>.
- (34) Dischler, B.; Bubenzer, A.; Koidl, P. Hard Carbon Coatings with Low Optical Absorption. *Appl. Phys. Lett.* **1983**, *42* (8), 636–638. <https://doi.org/10.1063/1.94056>.
- (35) Rodil, S. E. Infrared Spectra of Amorphous Carbon Based Materials. *Diamond and Related Materials* **2005**, *14* (8), 1262–1269. <https://doi.org/10.1016/j.diamond.2005.01.044>.
- (36) Ferrari, A. C.; Robertson, J. Raman Spectroscopy of Amorphous, Nanostructured, Diamond-like Carbon, and Nanodiamond. *Philosophical Transactions of the Royal Society of London. Series A: Mathematical, Physical and Engineering Sciences* **2004**, *362* (1824), 2477–2512. <https://doi.org/10.1098/rsta.2004.1452>.
- (37) Irmer, G.; Dorner-Reisel, A. Micro-Raman Studies on DLC Coatings. *Advanced Engineering Materials* **2005**, *7* (8), 694–705. <https://doi.org/10.1002/adem.200500006>.
- (38) Praver, S.; Nemanich, R. J. Raman Spectroscopy of Diamond and Doped Diamond. **2004**, 31.

- (39) Chen, Z. Y.; Zhao, J. P.; Yano, T.; Ooie, T.; Yoneda, M.; Sakakibara, J. Observation of Sp³ Bonding in Tetrahedral Amorphous Carbon Using Visible Raman Spectroscopy. *Journal of Applied Physics* **2000**, *88* (5), 2305–2308. <https://doi.org/10.1063/1.1288160>.
- (40) Paillard, V. On the Origin of the 1100 Cm⁻¹ Raman Band in Amorphous and Nanocrystalline Sp³ Carbon. *Europhysics Letters (EPL)* **2001**, *54* (2), 194–198. <https://doi.org/10.1209/epl/i2001-00105-4>.
- (41) Tauc, J.; Menth, A. States in the Gap. *Journal of Non-Crystalline Solids* **1972**, *8–10*, 569–585. [https://doi.org/10.1016/0022-3093\(72\)90194-9](https://doi.org/10.1016/0022-3093(72)90194-9).
- (42) Evingür, G. A.; Pekcan, Ö. Optical Energy Band Gap of PAAm-GO Composites. *Composite Structures* **2018**, *183*, 212–215. <https://doi.org/10.1016/j.compstruct.2017.02.058>.
- (43) Jarosiński, Ł.; Pawlak, J.; Al-Ani, S. K. J. Inverse Logarithmic Derivative Method for Determining the Energy Gap and the Type of Electron Transitions as an Alternative to the Tauc Method. *Optical Materials* **2019**, *88*, 667–673. <https://doi.org/10.1016/j.optmat.2018.12.041>.
- (44) Vaghri, E.; Khalaj, Z.; Ghoranneviss, M. Preparation and Characterization of Diamond-like Carbon Films on Various Substrates by PECVD System. *Studia Universitatis Babes-Bolyai Chemia* **2012**, *3*, 143–150.
- (45) Silva, C. T.; Monteiro, J.; Radovanovic, E. Unprecedented High Plasmonic Sensitivity of Substrates Based on Gold Nanoparticles. *Sensors and Actuators B Chemical* **2014**, *191*, 152–157. <https://doi.org/10.1016/j.snb.2013.09.109>.
- (46) Chang, D. W.; Lee, E. K.; Park, E. Y.; Yu, H.; Choi, H.-J.; Jeon, I.-Y.; Sohn, G.-J.; Shin, D.; Park, N.; Oh, J. H.; Dai, L.; Baek, J.-B. Nitrogen-Doped Graphene Nanoplatelets from Simple Solution Edge-Functionalization for n-Type Field-Effect Transistors. *J. Am. Chem. Soc.* **2013**, *135* (24), 8981–8988. <https://doi.org/10.1021/ja402555n>.
- (47) Stankovich, S.; Piner, R. D.; Nguyen, S. T.; Ruoff, R. S. Synthesis and Exfoliation of Isocyanate-Treated Graphene Oxide Nanoplatelets. *Carbon* **2006**, *44* (15), 3342–3347. <https://doi.org/10.1016/j.carbon.2006.06.004>.
- (48) Bonelli, M.; Ferrari, A. C.; Fioravanti, A. P.; Miotello, A.; Ossi, P. M. Structural and Mechanical Properties of Diamond-Like Carbon Films Prepared by Pulsed Laser Deposition With Varying Laser Intensity. *MRS Proc.* **1999**, *593*, 359. <https://doi.org/10.1557/PROC-593-359>.
- (49) Sánchez, N. A.; Rincón, C.; Zambrano, G.; Galindo, H.; Prieto, P. Characterization of Diamond-like Carbon (DLC) Thin Films Prepared by r.f. Magnetron Sputtering. *Thin Solid Films* **2000**, *373* (1–2), 247–250. [https://doi.org/10.1016/S0040-6090\(00\)01090-7](https://doi.org/10.1016/S0040-6090(00)01090-7).
- (50) Chung, P.-H.; Perevedentseva, E.; Tu, J.-S.; Chang, C. C.; Cheng, C.-L. Spectroscopic Study of Bio-Functionalized Nanodiamonds. *Diamond and Related Materials* **2006**, *15* (4), 622–625. <https://doi.org/10.1016/j.diamond.2005.11.019>.
- (51) *Nanomaterials Handbook*, Second edition.; Gogotsi, Y., Ed.; Advanced materials and technologies series; CRC Press, Taylor & Francis Group, CRC Press is an imprint of the Taylor & Francis Group, an informa business: Boca Raton, 2017.
- (52) Shahriary, L.; Athawale, A. Graphene Oxide Synthesized by Using Modified Hummers Approach. *Renew. Energy Environ. Eng.* **2014**, *2*.
- (53) Aldosari, M.; Othman, A.; Alsharaeh, E. Synthesis and Characterization of the in Situ Bulk Polymerization of PMMA Containing Graphene Sheets Using Microwave Irradiation. *Molecules* **2013**, *18* (3), 3152–3167. <https://doi.org/10.3390/molecules18033152>.
- (54) Ban, F. Y.; Majid, S. R.; Huang, N. M.; Lim, H. N. Graphene Oxide and Its Electrochemical Performance. *Int. J. Electrochem. Sci.* **2012**, *7*, 7.
- (55) Chhabra, V. A.; Deep, A.; Kaur, R.; Kumar, R. Functionalization of Graphene Using Carboxylation Process. **2012**, *8*.

- (56) Tu, J.-S.; Perevedentseva, E.; Chung, P.-H.; Cheng, C.-L. Size-Dependent Surface CO Stretching Frequency Investigations on Nanodiamond Particles. *J. Chem. Phys.* **2006**, *125* (17), 174713. <https://doi.org/10.1063/1.2370880>.
- (57) A. C. Obreja; D. Cristea; R. Gavrilă; V. Schiopu; A. Dinescu; M. Danila; F. Comanescu. Functionalized Graphene / Poly 3-Hexyl Thiophene Based Nanocomposites. In *CAS 2011 Proceedings (2011 International Semiconductor Conference)*; 2011; Vol. 1, pp 27–30. <https://doi.org/10.1109/SMICND.2011.6095703>.
- (58) Beeman, D.; Silverman, J.; Lynds, R.; Anderson, M. R. Modeling Studies of Amorphous Carbon. *Phys. Rev. B* **1984**, *30* (2), 870–875. <https://doi.org/10.1103/PhysRevB.30.870>.
- (59) Roy, M.; George, V. C.; Dua, A. K.; Raj, P.; Schulze, S.; Tenne, D. A.; Salvan, G.; Zahn, D. R. T. Detection of Nanophase at the Surface of HFCVD Grown Diamond Films Using Surface Enhanced Raman Spectroscopic Technique. *Diamond and Related Materials* **2002**, *11* (11), 1858–1862. [https://doi.org/10.1016/S0925-9635\(02\)00174-7](https://doi.org/10.1016/S0925-9635(02)00174-7).
- (60) Ferrari, A. C.; Robertson, J. Origin of the $\sim 1150\text{ cm}^{-1}$ Raman Mode in Nanocrystalline Diamond. *Phys. Rev. B* **2001**, *63* (12), 121405. <https://doi.org/10.1103/PhysRevB.63.121405>.
- (61) Saito, R.; Jorio, A.; Souza Filho, A. G.; Dresselhaus, G.; Dresselhaus, M. S.; Pimenta, M. A. Probing Phonon Dispersion Relations of Graphite by Double Resonance Raman Scattering. *Phys. Rev. Lett.* **2001**, *88* (2), 027401. <https://doi.org/10.1103/PhysRevLett.88.027401>.
- (62) Saito, R.; Hofmann, M.; Dresselhaus, G.; Jorio, A.; Dresselhaus, M. S. Raman Spectroscopy of Graphene and Carbon Nanotubes. *Advances in Physics* **2011**, *60* (3), 413–550. <https://doi.org/10.1080/00018732.2011.582251>.
- (63) Childres, I.; Jauregui, L. A.; Park, W.; Cao, H.; Chen, Y. P. RAMAN SPECTROSCOPY OF GRAPHENE AND RELATED MATERIALS. 20.
- (64) Schwan, J.; Ulrich, S.; Batori, V.; Ehrhardt, H.; Silva, S. R. P. Raman Spectroscopy on Amorphous Carbon Films. *Journal of Applied Physics* **1996**, *80* (1), 440–447. <https://doi.org/10.1063/1.362745>.
- (65) Nemanich, R. J.; Solin, S. A. First- and Second-Order Raman Scattering from Finite-Size Crystals of Graphite. *Phys. Rev. B* **1979**, *20* (2), 392–401. <https://doi.org/10.1103/PhysRevB.20.392>.
- (66) Garino, Y.; Teraji, T.; Koizumi, S.; Koide, Y.; Ito, T. Effects of Shallow Traps on the Reverse Current of Diamond Schottky Diode: An Electrical Transient Study. *phys. stat. sol. (a)* **2010**, *207* (6), 1460–1463. <https://doi.org/10.1002/pssa.200925448>.
- (67) Baba, S.; Ito, T.; Toyoda, T.; Wakamatsu, O.; Machida, T. Meaning of Pre-Irradiation to Diamond Detector. *Nippon Hoshasen Gishikai Zasshi* **2002**, *49* (10), 1250–1255.
- (68) De Angelis, C.; Onori, S.; Pacilio, M.; Cirrone, G. A. P.; Cuttone, G.; Raffaele, L.; Bucciolini, M.; Mazzocchi, S. An Investigation of the Operating Characteristics of Two PTW Diamond Detectors in Photon and Electron Beams. *Medical Physics* **2002**, *29* (2), 248–254. <https://doi.org/10.1118/1.1446101>.
- (69) Piliero, M. A.; Hugtenburg, R. P.; Ryde, S. J. S.; Oliver, K. Development of CVD Diamond Detectors for Clinical Dosimetry. *Radiation Physics and Chemistry* **2014**, *104*, 10–14. <https://doi.org/10.1016/j.radphyschem.2014.04.030>.